

**MAGNETIC RESONANCE IMAGING OF  
SPINAL CORD AND BRAIN IN  
ANIMAL MODELS OF MULTIPLE SCLEROSIS**

**By**

**ANGELA E. SCHELLENBERG**

**A Thesis  
Submitted to the Faculty of Graduate Studies  
In Partial Fulfilment of the Requirements  
For the degree of**

**DOCTOR OF PHILOSOPHY**

**Department of Pharmacology and Therapeutics  
Faculty of Medicine  
University of Manitoba  
Winnipeg, Manitoba**

**© Angela E. Schellenberg, June 2008**

**THE UNIVERSITY OF MANITOBA  
FACULTY OF GRADUATE STUDIES  
\*\*\*\*\*  
COPYRIGHT PERMISSION**

**Magnetic Resonance Imaging of Spinal Cord and Brain  
in Animal Models of Multiple Sclerosis**

**BY**

**Angela E. Schellenberg**

**A Thesis/Practicum submitted to the Faculty of Graduate Studies of The University of  
Manitoba in partial fulfillment of the requirement of the degree**

**Of**

**Doctor of Philosophy**

**Angela E. Schellenberg © 2008**

**Permission has been granted to the University of Manitoba Libraries to lend a copy of this thesis/practicum, to Library and Archives Canada (LAC) to lend a copy of this thesis/practicum, and to LAC's agent (UMI/ProQuest) to microfilm, sell copies and to publish an abstract of this thesis/practicum.**

**This reproduction or copy of this thesis has been made available by authority of the copyright owner solely for the purpose of private study and research, and may only be reproduced and copied as permitted by copyright laws or with express written authorization from the copyright owner.**

***“Be the change you wish to see in the world.”*** - Mahatma Gandhi

## ACKNOWLEDGEMENTS

I would like to express my thanks to my supervisor Dr. Jim Peeling for accepting me as a graduate student in his lab. I enjoyed my experience and appreciate the opportunity to work in the MR lab. Dr. Peeling provided guidance and direction throughout my research project and at the same time taught me independence and critical thinking.

Thank you to Dr. Richard Buist for training me on the use of the MR system and software. Dr. Buist was in the lab daily and always took the time to answer my questions and provide assistance when a problem arose. Thank you for all your help and for the many discussions.

I would like to thank Dr. Marc Del Bigio for sharing his expertise in the histology component of my project and thanks to Osaama Khan and Terry Enno from the Del Bigio lab for their assistance.

My advisory committee members Dr. Chris Anderson, Dr. Fiona Parkinson, and Dr. Marc Del Bigio attended and provided input at all my committee meetings held twice a year. I thank them for all the direction and support since I began my degree.

I would like to thank all the collaborators I had the opportunity to work with during the last four years. Thank you to Dr. V. Wee Yong and members of his lab who taught me the methods for EAE induction. Dr. Trevor Owens and Dr. Henrik Toft-Hansen sent the transgenic mice for the study dealing with CCL2 upregulation. Their assistance and valuable advice made this project possible. Dr. Christopher Power and Dr. Shigeki Tsutsui were collaborators in the study with A1AR knockout mice. Thanks

to them for providing the mice for this experiment and their assistance with EAE induction techniques and EAE scoring. Thank you to Dr. Don Miller for the useful discussions during the collaboration on the S1P project and also thank you to Dr. Melanie Martin for the helpful discussions on MRI.

Thank you to the Department of Pharmacology, especially Dr. Ratna Bose, for the invaluable discussions and advice. The department supported me through awards and financial support to present my research at scientific conferences.

Thanks to the many fellow Pharmacology students along the way for your friendship and shared conversations. A special thanks to Carmen Edmundson, Annie Kim, and Heather Ostermann for all your help and support in the lab and making the lab environment enjoyable through your company and conversations.

I would like to acknowledge the Natural Sciences and Engineering Research Council of Canada (NSERC) for providing me with financial support over the last three years. I would also like to acknowledge grant funding for my research project from the Interdisciplinary Health Research Teams (IHRT) program of the Canadian Institutes of Health Research (CIHR).

Lastly and importantly I would like to thank my father Harry, mother Irene, brother Harold, sister-in-law Shannon and my close friends for all your encouragement during the completion of my PhD. Your support gave me the motivation to persevere and follow my dreams. Thanks for always believing in me and supporting my decisions. My parents taught me the importance of a higher education that led me to pursue a graduate degree. Without this drive and passion for learning, I would not have completed such an achievement.

## TABLE OF CONTENTS

<b>Acknowledgements</b>	II
<b>Table of Contents</b>	IV
<b>List of Abbreviations</b>	VIII
<b>List of Figures</b>	XII
<b>List of Tables</b>	XVI
<b>Abstract</b>	XVII
<b>Chapter I: Introduction</b>	1
1.1 Multiple Sclerosis	2
1.1.1 Clinical Presentation of MS	2
1.1.2 Etiology and Prevalence of MS	3
1.1.3 Immune Response in MS	4
1.1.3.1 Inflammation	4
1.1.3.2 Demyelination	8
1.1.3.3 Neurodegenerative Phase	9
1.1.4 Role of Cytokines in MS	9
1.1.5 Approved Treatments for MS	11
1.2 Experimental Autoimmune Encephalomyelitis	12
1.2.1 EAE as a Model of MS	12
1.2.2 Contrasts between EAE and MS	13
1.3 Blood-Brain and Blood-Spinal Cord Barriers	14
1.4 Magnetic Resonance Imaging	17
1.4.1 Protons and Magnetism	17
1.4.2 Radiofrequency Pulses and Spin Relaxation	17
1.4.3 Magnetic Field Gradients	20
1.4.4 Pulse Sequences	20
1.4.5 T <sub>1</sub> - and T <sub>2</sub> -weighted Imaging	21
1.4.6 Magnetization transfer-weighted Imaging	22
1.4.7 Gadolinium Contrast Agent	23
1.4.8 MRI in MS and EAE	24

<b>Chapter II: Hypothesis and Objectives</b>	<b>26</b>
2.1 Hypothesis	27
2.2 Specific Objectives	27
<b>Chapter III: General Methodology</b>	<b>29</b>
3.1 Induction of EAE	30
3.2 Scoring System	31
3.3 Magnetic Resonance Imaging	33
3.3.1 T <sub>2</sub> -weighted MR Imaging	35
3.3.2 T <sub>1</sub> -weighted contrast-enhanced MR Imaging	35
3.3.3 MT-weighted MR imaging	36
3.3.4 Slice Positioning	36
3.3.4.1 Imaging of the spinal cord: two sets of interleaved slices	36
3.3.4.2 Imaging of the spinal cord: single set of slices	36
3.3.4.3 Imaging of the brain	37
3.4 MR Image Processing	40
3.4.1 T <sub>2</sub> -weighted MR Images of the Spinal Cord	40
3.4.2 T <sub>2</sub> -weighted MR Images of the Brain	40
3.4.3 T <sub>1</sub> -weighted contrast-enhanced MR Images of the Spinal Cord	42
3.4.4 T <sub>1</sub> -weighted contrast-enhanced MR Images of the Brain	42
3.4.5 MT-weighted MR Images of the Spinal Cord	42
<b>Chapter IV: Preliminary Magnetic Resonance Imaging Studies</b>	<b>44</b>
4.1 MRI of the Central Nervous System in MOG-Induced EAE	45
4.2 Kinetics of Contrast Enhancement in the Spinal Cord	48
4.3 Dextran Tracer Pilot Study	51
<b>Chapter V: Magnetic Resonance Imaging of Blood-Spinal Cord Barrier Disruption in Mice with Experimental Autoimmune Encephalomyelitis</b>	<b>55</b>
5.1 Introduction	56

5.2	Materials and Methods	58
5.2.1	Induction of EAE and Scoring System	58
5.2.2	MR Imaging	58
5.2.3	MR Image Analysis	59
5.2.4	Tissue Processing and Scoring of Inflammation	59
5.2.5	Statistical Analysis	61
5.3	Results	63
5.4	Discussion	72
<b>Chapter VI:</b>	<b>Blood-Brain Barrier Disruption in CCL2 Transgenic Mice during Pertussis Toxin-Induced Brain Inflammation</b>	<b>77</b>
6.1	Introduction	78
6.2	Methods	80
6.2.1	Animal Model	80
6.2.2	MR Imaging	81
6.2.3	MR Image Analysis	81
6.2.4	Tissue Processing	84
6.2.5	Statistical Analysis	84
6.3	Results	86
6.3.1	MR Imaging	86
6.3.2	Clinical Signs	92
6.3.3	Histology	94
6.4	Discussion	100
<b>Chapter VII:</b>	<b>Magnetic Resonance Imaging of the Spinal Cord of A1 Adenosine Receptor Knockout Mice with Experimental Autoimmune Encephalomyelitis</b>	<b>104</b>
7.1	Introduction	105
7.2	Methods	107
7.2.1	Induction of EAE and Scoring System	107
7.2.2	MR Imaging	107
7.2.3	MR Image Analysis	108
7.2.4	Statistical Analysis	108

7.3	Results	109
7.3.1	Behaviour Scores and Changes in Weight	109
7.3.2	Contrast Enhancement	111
7.3.3	Spinal Cord Volume	115
7.4	Discussion	118
<b>Chapter VIII: Effects of Sphingosine 1-Phosphate in Mice with Experimental Autoimmune Encephalomyelitis</b>		<b>120</b>
8.1	Introduction	121
8.2	Methods	123
8.2.1	Induction of EAE and Scoring System	123
8.2.2	S1P Administration	123
8.2.3	MR Imaging	123
8.2.4	MR Image Analysis	125
8.2.5	Statistical Analysis	125
8.3	Results	126
8.3.1	Behaviour Scores	126
8.3.2	Changes in Weight	127
8.3.3	Contrast Enhancement	132
8.3.4	MTR	138
8.3.5	Spinal Cord Volume	139
8.4	Discussion	144
8.4.1	Behavioural Scores	144
8.4.2	Changes in Weight	145
8.4.3	Contrast Enhancement	145
8.4.4	MTR	146
<b>Chapter IX: Conclusions</b>		<b>148</b>
<b>Appendix A</b>		<b>151</b>
	Pulse sequence for T <sub>2</sub> -weighted imaging	152
	Pulse sequence for T <sub>1</sub> -weighted imaging	153
	Pulse sequence for MT-weighted imaging with saturation pulse	154
	Monitoring Record	155
<b>References</b>		<b>156</b>

## LIST OF ABBREVIATIONS

A1AR	A1 adenosine receptor
ANOVA	analysis of variance
APC	antigen-presenting cell
B <sub>0</sub>	external magnetic field
B <sub>1</sub>	applied magnetic field
BBB	blood-brain barrier
BSA	bovine serum albumin
BSB	blood-spinal cord barrier
CFA	complete Freund's adjuvant
CNPase	cyclic nucleotide phosphohydrolase
CNS	central nervous system
CSF	cerebral spinal fluid
CTLA	cytotoxic T lymphocyte antigen
D	Dalton
DAB	diaminobenzidine
DAPI	4',6-diamidino-2-phenyl indole
EAE	experimental autoimmune encephalomyelitis
Edg	endothelial differentiation gene
<i>f</i>	frequency
FID	free induction decay
FITC	fluorescein

FOV	field of view
FTY720	2-amino-2-(2-[4-octylphenyl]ethyl)-1,3-propanediol hydrochloride
$\gamma$	gyromagnetic ratio
GA	glatiramer acetate
Gd-DTPA	gadolinium diethylene-triamine-pentaacetate
GFAP	glial fibrillary acidic protein
GS	Griffonia simplicifolia
H&E	hematoxylin & eosin
HBSS	Hanks' balanced salt solution
HLA	human leukocyte antigen
Hz	Hertz
ICAM	intercellular adhesion molecule
IFN	interferon
IgG	immunoglobulin G
IL	interleukin
LPS	lipopolysaccharide
LT	lymphotoxin
$M_0$	net magnetization
$M_{xy}$	magnetization in the xy plane
$M_z$	magnetization in the z plane
MAG	myelin-associated glycoprotein
MBP	myelin basic protein
MCP	monocyte chemoattractant protein

MHC	major histocompatibility complex
MMP	matrix metalloproteinase
MOG	myelin oligodendrocyte glycoprotein
MRI	magnetic resonance imaging
mRNA	messenger ribonucleic acid
MS	multiple sclerosis
MT	magnetization transfer
MTR	magnetization transfer ratio
NK	natural killer
NO	nitric oxide
PBS	phosphate buffered saline
PD	proton density
PLP	proteolipid protein
PTx	pertussis toxin
RF	radiofrequency
ROI	region of interest
$S_0$	signal intensity without saturation
$S_1$	signal intensity with saturation
SIP	sphingosine 1-phosphate
SE	spin echo
SEM	standard error of the mean
T	Tesla
$T_1$	longitudinal spin-lattice relaxation constant

T <sub>2</sub>	transverse spin-spin relaxation constant
TCR	T cell receptor
TGF	transforming growth factor
Th1	T helper 1
Th2	T helper 2
TE	echo time
TNF	tumor necrosis factor
TR	recovery time

## LIST OF FIGURES

- Figure 1.1** A schematic diagram of the immune response in the pathogenesis of MS.
- Figure 1.2** A coronal section of a human brain from a deceased individual that had MS.
- Figure 1.3** A schematic drawing of the anatomical structure of the BBB/BSB of a postcapillary venule.
- Figure 1.4** The net magnetization vector  $M_0$  flips into the xy plane following a  $90^\circ$  RF pulse.
- Figure 1.5** The relative recovery of longitudinal magnetization with time constant  $T_1$  and decay of transverse magnetization with time constant  $T_2$  following a  $90^\circ$  RF pulse.
- Figure 1.6** The molecular structure of Gd-DTPA.
- Figure 3.1** Photographs demonstrating the scoring system for mice with EAE.
- Figure 3.2** Bruker Biospec 7T/21cm magnet and surface and volume coils used for all imaging experiments.
- Figure 3.3** MR scout images indicating various MR slice positioning.
- Figure 3.4**  $T_2$ -weighted images and defining the area of the spinal cord.
- Figure 3.5**  $T_2$ -weighted images and defining the area of the brain.
- Figure 3.6** MT-weighted images and defining the areas of grey and white matter within the spinal cord.
- Figure 4.1** Representative  $T_1$ -weighted contrast-enhanced difference images of the brain and spinal cord from a mouse with EAE before and at the onset of disease signs.
- Figure 4.2** Pre- and post-contrast-enhanced  $T_1$ -weighted images of the lumbar spinal cord from a mouse with EAE at the beginning of disease signs.
- Figure 4.3** A representative calculated difference image of contrast enhancement of the lumbar spinal cord from a mouse with EAE acquired at six time points at the onset of disease with corresponding quantified intensity.

- Figure 4.4** Dissection of the imaged region of the lumbar spinal cord.
- Figure 4.5** Histology of the spinal cord from a mouse with EAE following intravenous administration of dextran tracer with corresponding calculated difference image of contrast enhancement.
- Figure 5.1** Tissue dissection of the lumbar spinal cord *in situ*.
- Figure 5.2** Average scores of disease severity and body weight in mice during the progression of EAE.
- Figure 5.3** Representative sets of calculated contrast-enhanced images of mice with EAE at different stages of disease.
- Figure 5.4** The average percent intensity change in T<sub>1</sub>-weighted MR images of the lumbar spinal cord in mice with EAE at different stages of disease.
- Figure 5.5** Representative histograms of the pixel intensities within the spinal cord of mice with EAE at different stages of disease.
- Figure 5.6** Histological sections of lumbar spinal cord stained with H&E, lectin, IgG, and solochrome cyanin from mice with EAE at various stages of disease progression.
- Figure 5.7** Histological scores for H&E, lectin, and solochrome cyanin for mice with EAE at different stages of disease.
- Figure 6.1** Calculated image of percent enhancement of the brain from a CCL2 transgenic mouse with corresponding histogram of percent intensity.
- Figure 6.2** Calculated image of percent enhancement of the brain from a CCL2 transgenic mouse following PTx administration with corresponding histogram of percent intensity.
- Figure 6.3** Dissection of the imaged region of the brain.
- Figure 6.4** Representative contrast-enhanced difference images taken from wild type and CCL2 transgenic mice that were administered HBSS, 10 $\mu$ g/kg PTx, or 20 $\mu$ g/kg PTx obtained pre-injection, days 1, 3, and 5 post-injection.
- Figure 6.5** The percentage of pixels enhancing with an intensity of 20% or greater within each contrast-enhanced difference image of the brain of all groups of mice following PTx/HBSS at day 3 post injection.

- Figure 6.6** The percentage of pixels in the posterior six slices of the brain showing a 20% or greater increase in intensity on calculated percent enhancement images for wild type and transgenic mice pre-injection and days 1, 3 and 5 post-HBSS/PTx.
- Figure 6.7** Average histogram of the third anterior slice for wild type and transgenic mice before the administration of PTx or HBSS.
- Figure 6.8** The change in weight following the injection of HBSS or PTx in CCL2 transgenic and wild type mice over 5 days.
- Figure 6.9** Histological sections stained with H&E and corresponding sections of fluorescent dextrans taken from wild type and CCL2 transgenic mice following HBSS or PTx administration.
- Figure 6.10** A histological H&E section of the brain from a CCL2 transgenic mouse following PTx and corresponding contrast-enhanced percent difference MR image.
- Figure 6.11** Histological sections of vessels within the brain of CCL2 transgenic mice identifying fluorescent dextrans, GFAP, DAPI and laminin.
- Figure 7.1** Average scores of A1AR<sup>+/+</sup>, A1AR<sup>+/-</sup> and A1AR<sup>-/-</sup> mice during the progression of EAE and calculations of maximum score, disease burden and day of disease onset for each animal.
- Figure 7.2** Average weight changes of A1AR<sup>+/+</sup>, A1AR<sup>+/-</sup> and A1AR<sup>-/-</sup> mice during the progression of EAE and the total drop in weight for each animal.
- Figure 7.3** Representative sets of calculated contrast-enhanced images for a control mouse, A1AR<sup>+/+</sup>, A1AR<sup>+/-</sup> and A1AR<sup>-/-</sup> mouse at the initial stage of disease and at remission.
- Figure 7.4** The average percent intensity for the entire set of slices in A1AR<sup>+/+</sup>, A1AR<sup>+/-</sup> and A1AR<sup>-/-</sup>, and control mice at onset and remission stages of disease.
- Figure 7.5** Complete sets of T<sub>2</sub>-weighted images from the same A1AR<sup>+/+</sup> mouse that was imaged at pre-disease, early stage of disease, and day 30 with corresponding spinal cord volumes.
- Figure 7.6** The average change in spinal cord volume from initial onset of signs to remission for A1AR<sup>+/+</sup>, A1AR<sup>+/-</sup> and A1AR<sup>-/-</sup>, and control mice as well as grouped according to complete versus incomplete recovery at remission.

- Figure 8.1** The molecular structure of S1P.
- Figure 8.2** Average scores of mice during disease progression that received daily doses of S1P or BSA beginning at the onset of disease signs and day 7.
- Figure 8.3** The maximum score, disease burden, and day of disease onset for each animal according to the S1P or BSA dosing regimen.
- Figure 8.4** Average weight changes of mice during disease progression that received daily doses of S1P or BSA beginning at the onset of disease signs and at day 7.
- Figure 8.5** The drop in weight for each animal according to the S1P or BSA dosing regimen.
- Figure 8.6** Representative sets of calculated contrast-enhanced images of the lumbar spinal cord with ROIs outlining the areas of grey and white matter at various stages of disease.
- Figure 8.7** A representative calculated difference image of percent enhancement of the spinal cord from a control mouse at the onset of disease signs indicating the regions of grey and white matter and the corresponding histogram.
- Figure 8.8** The average percent intensity change in T<sub>1</sub>-weighted MR images of the lumbar spinal cord following Gd-DTPA administration.
- Figure 8.9** The average percent change in intensity within the spinal cord on calculated contrast-enhanced difference images at the initial stage of disease relative to 6 hours post S1P/BSA administration.
- Figure 8.10** Representative MTR maps at various time points of disease progression of mice that were administered different doses of S1P.
- Figure 8.11** The average MTR within the grey and white matter of the spinal cord of mice that were administered S1P or BSA beginning at the onset of disease signs.
- Figure 8.12** The average MTR within the grey and white matter of the spinal cord of mice that were administered S1P or BSA beginning at day 7.
- Figure 8.13** The average percent change in cord volume relative to pre-disease values with first administration of S1P/BSA at day 7 and at initial signs of disease.

## **LIST OF TABLES**

**Table 1.1** Tracers commonly used to detect vascular permeability.

**Table 8.1** S1P/BSA treatment groups and imaging protocol.

## ABSTRACT

Magnetic resonance imaging (MRI) can be used to follow the progression of tissue injury within the central nervous system (CNS) caused by autoimmune inflammatory responses found in diseases such as multiple sclerosis (MS). Contrast-enhanced T<sub>1</sub>-weighted MRI can detect changes in the extent of blood-brain barrier (BBB) and blood-spinal cord barrier (BSB) disruption and magnetization transfer (MT)-weighted MRI can detect changes in myelin content.

Experimental autoimmune encephalomyelitis (EAE), an animal model of demyelinating disease, is associated with the breakdown of the BBB and BSB and the infiltration of macrophages and T cells into the CNS.

The first study used a myelin oligodendrocyte glycoprotein (MOG)-induced mouse model of EAE to study the relative changes in vascular permeability using T<sub>1</sub>-weighted contrast-enhanced MRI of the lumbar spinal cord at various stages of disease severity. Maximum breakdown of the BSB was observed at the earliest indication of disease, occurring before maximum inflammation seen histologically. The use of contrast-enhanced MRI to quantify relative vascular permeability of mouse spinal cord can be further applied to study genetically altered mouse models.

BBB disruption was determined to be a prerequisite to CNS inflammation in the second study. Transgenic mice that overexpressed the chemokine CCL2 showed weight loss and infiltration of leukocytes into the brain parenchyma following pertussis toxin (PTx) administration. This combination of genetic predisposition with an

environmental trigger resulted in focal areas of increased permeability within the brain of CCL2 transgenic mice that was visualized using contrast-enhanced MRI.

In the third study, contrast-enhanced MRI of the lumbar spinal cord was performed in MOG-induced EAE, comparing mice with a knocked out A1 adenosine receptor (A1AR) to wild type mice. No significant difference in the relative change of vascular permeability was found between the groups. Therefore, the role of the A1AR alone was not found to have significant effects on BSB regulation.

Contrast-enhanced T<sub>1</sub>-weighted and MT-weighted MRI was used to study the effects of sphingosine 1-phosphate (S1P) on BSB permeability and demyelination in the mouse model of MOG-induced EAE in the final study. S1P was not found to have any long term protective effects in stabilizing the BSB; however, a high dose of S1P was observed to reduce the extent of demyelination.

## **CHAPTER I**

### **INTRODUCTION**

## 1.1 Multiple Sclerosis

### 1.1.1 *Clinical Presentation of MS*

Multiple sclerosis (MS) is the most common neurological disease currently affecting young adults with twice as many females affected as males.<sup>1</sup> MS can follow a relapsing-remitting, primary progressive, or secondary progressive disease course. The relapsing-remitting clinical course is seen most commonly, presenting in 80% of patients, where clinical signs and symptoms develop and spontaneously resolve after a few weeks.<sup>2,3</sup> When clinical signs and symptoms begin to persist or progress between relapses and the disease course eventually changes into a progressive pattern, this is known as secondary progressive MS.<sup>2,3</sup> Patients with primary progressive MS show gradual worsening of signs and symptoms from the time of the initial symptoms.<sup>2,3</sup> Common presenting symptoms and signs of MS are vision problems, limb weakness, loss of coordination and balance, vertigo, fatigue, sensory loss, pain, cognitive impairment, bowel, bladder, and sexual dysfunction.<sup>2,4</sup>

MS is diagnosed using clinical observations often aided by various laboratory tests and procedures such as magnetic resonance imaging (MRI). Multifocal lesions within the central nervous system (CNS) on MR images, especially in the periventricular white matter, brain stem, cerebellum, and spinal cord white matter, support a diagnosis of MS.<sup>2</sup> Focal areas of hyperintensity can be visualized within the brain or spinal cord on T<sub>2</sub>-weighted MR images in more than 95% of patients.<sup>5,6</sup> More than 90% of individuals with MS also show an elevated amount of immunoglobulins within their cerebral spinal fluid (CSF), particularly oligoclonal bands of

immunoglobulin G (IgG).<sup>2,6-8</sup> A diagnosis of MS requires patients to have lesions that affect at least two distinct sites in the CNS with two episodes of neurological symptoms separated in time that are not otherwise explained.<sup>3,4,9,10</sup>

### *1.1.2 Etiology and Prevalence of MS*

MS is a disease of the CNS that involves inflammation, edema, demyelination, limited remyelination, and axon damage.<sup>6</sup> The cause of MS is still unknown today, but is believed to involve genetic factors, environmental triggers, and autoimmune mechanisms. The interaction of genetic predisposition and environmental factors is believed to trigger the onset of MS. There is a known higher geographic prevalence of MS with increasing latitude in both hemispheres, particularly in northern Europe, southern Australia, and the middle region of North America, supporting environmental factors as predisposing causes of MS.<sup>2,3</sup> According to the World Health Organization, there are approximately 1.1 to 2.5 million cases of MS world-wide.<sup>11</sup> In regions where MS is more prevalent 50 – 100 for every 100,000 are affected, whereas regions with a low prevalence only have 5 in 100,000 affected with the disease.<sup>11</sup> There is a significantly increased risk of disease in a first-degree relative of a patient with MS as compared to the general population<sup>2</sup> and there is evidence to support that human leukocyte antigen (HLA) classes I and II, T cell receptor  $\beta$ , cytotoxic T lymphocyte antigen (CTLA)-4, intercellular adhesion molecule (ICAM)-1, and SH2D2A genes are associated with MS.<sup>12</sup>

### *1.1.3 Immune Response in MS*

#### *1.1.3.1 Inflammation*

Patients with MS and healthy individuals both have autoreactive T cells to CNS antigens that are present in circulation. However, in MS patients these T cells enter the CNS and recognize myelin self-antigens, whereas in healthy individuals they fail to recognize self-antigens.<sup>4,13</sup> Regulatory T cells are believed to control the actions of autoreactive T cells.<sup>6</sup> It has been hypothesized that autoreactive CD4<sup>+</sup> T cells in individuals with MS may become activated through fragments of the CNS itself, molecular mimicry, or bystander activation. Molecular mimicry occurs when an epitope from a foreign antigen, such as a viral protein, is indistinguishable from an epitope in the CNS and causes the autoreactive T cells to activate.<sup>4,6,13-15</sup> In bystander activation, autoreactive T cells become activated through non-specific inflammatory events during infections.<sup>15</sup> In one theory, a foreign antigen, such as an antigen from a viral envelope, can act as a superantigen causing the activation of entire T cell populations and possibly leading to autoimmunity.<sup>4</sup>

Antigens are presented by antigen-presenting cells (APCs; dendritic cells, macrophages) on their major histocompatibility complex (MHC)-II to autoreactive CD4<sup>+</sup> T cells in the peripheral lymphoid tissue.<sup>15</sup> CD4<sup>+</sup> T cells interact with the MHC-II on APCs leading to hypersensitivity and antibody responses, whereas CD8<sup>+</sup> T cells interact with the MHC-I on APCs associated with cytotoxicity.<sup>4</sup> The T cell receptor (TCR) binds to the antigen and MHC resulting in T cell activation and proliferation.<sup>14,16,17</sup> CD4<sup>+</sup> T cells are divided into T helper 1 (Th1) and T helper 2 (Th2) cell subtypes. Th1 cells play an important role in cell-mediated immunity and

generally produce proinflammatory cytokines, whereas Th2 cells are important in humoral immunity and predominantly release anti-inflammatory cytokines.<sup>18</sup> CD4<sup>+</sup> Th1 cells are believed to be responsible for the initial events leading to the eventual destruction of myelin sheaths.<sup>15,17</sup> Activated CD4<sup>+</sup> T cells adhere and cross the blood-brain barrier (BBB) through the actions of adhesion molecules, proteases, chemokines, and enzymes such as matrix metalloproteinases (MMPs) that degrade the extracellular matrix of the BBB.<sup>13,15</sup> In the CNS the CD4<sup>+</sup> T cells must be reactivated by the presentation of a CNS antigen on the MHC-II of APCs (microglia, astrocytes, perivascular macrophages, endothelial cells).<sup>3,17</sup> Once reactivated, these T cells release proinflammatory Th1 cytokines which initiate inflammation and the activation of other cells of the immune system such as macrophages, B cells, and other T cells in the CNS.<sup>13,14</sup> The cytokines released from T cells also activate cells within the CNS such as microglia and astrocytes, which also secrete proinflammatory cytokines and attract more inflammatory cells (summarized in Figure 1.1).<sup>17</sup>

MS lesions contain parenchymal and perivascular infiltrates of lymphocytes and macrophages commonly at the site of postcapillary venules.<sup>3,19</sup> Cells that predominate within lesions are CD8<sup>+</sup> T cells with few B cells, CD4<sup>+</sup> T cells and plasma cells.<sup>4</sup> It has been hypothesized that CD8<sup>+</sup> T cells contribute more to the pathological process leading to axonal damage, whereas CD4<sup>+</sup> T cells are important in the triggering of the autoimmune inflammatory response.<sup>13</sup> MS plaques are focal areas of demyelination that are well-demarcated (Figure 1.2) and thought to arise from many small MS lesions consisting of perivascular cuffs of inflammatory cells.<sup>20</sup>

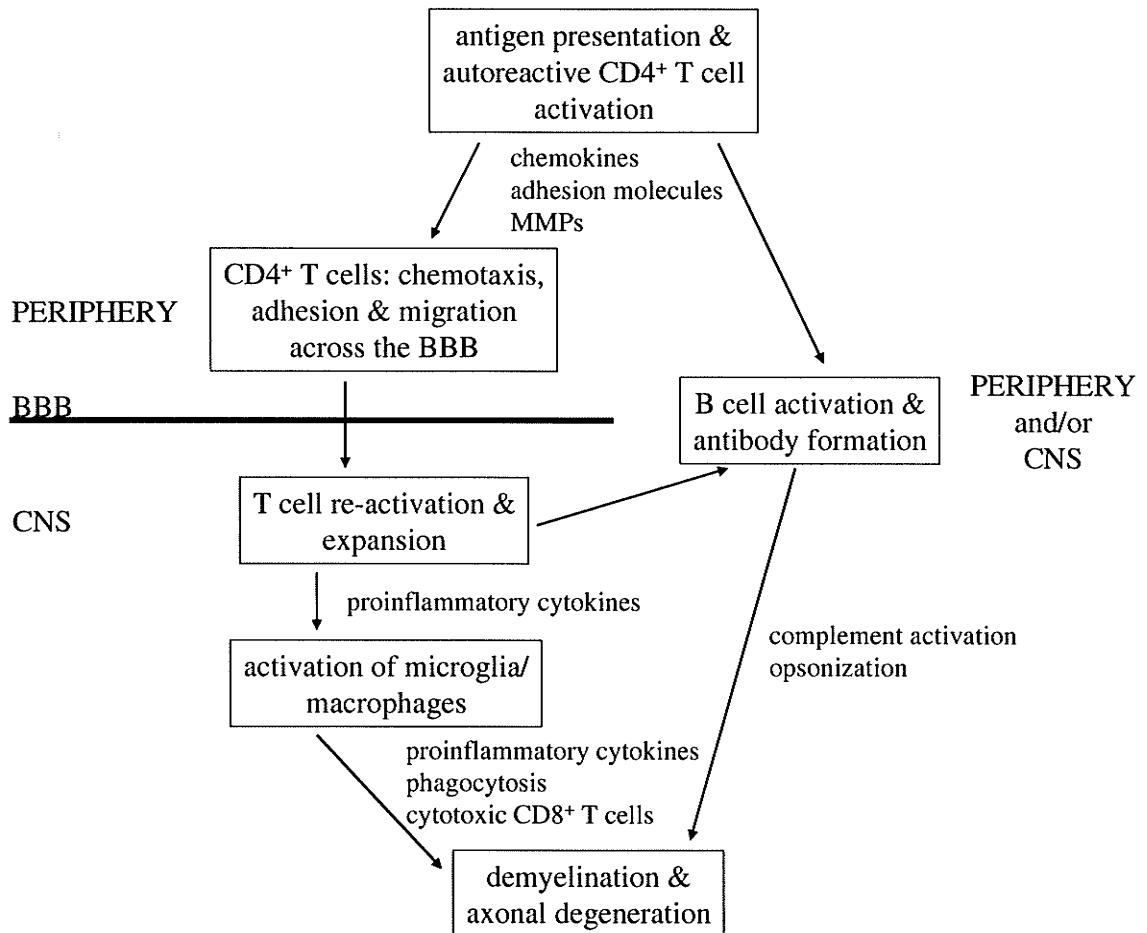


**Figure 1.1.** A schematic diagram of the immune response in the pathogenesis of MS.

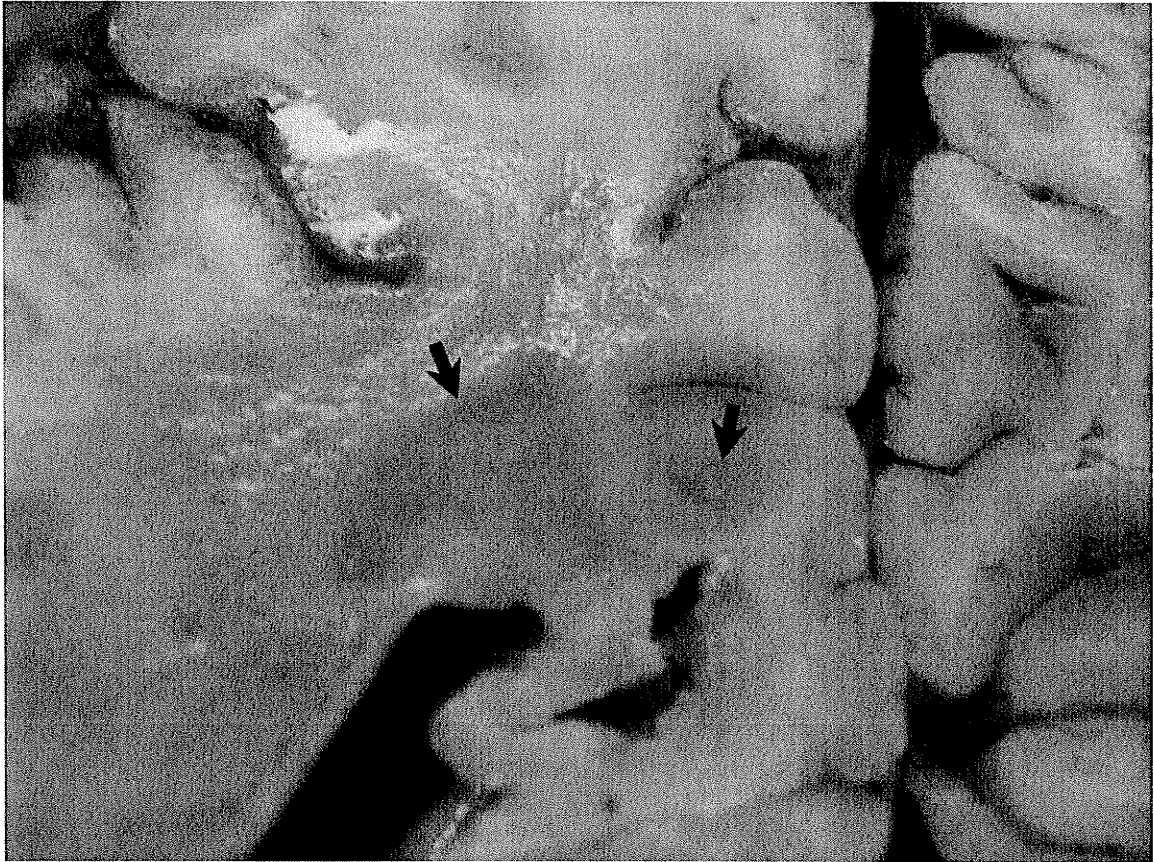


**Figure 1.2.** A coronal section of a human brain from a deceased individual that had MS. Arrows indicate areas of MS plaque formation. Specimen provided courtesy of Dr. Marc Del Bigio, Neuropathologist, Health Sciences Centre.

### 1.1.3.2 Demyelination

Numerous layers of the plasma membrane of oligodendrocytes wrap around axons within white matter tracts in the CNS to form the myelin sheath. A single oligodendrocyte has up to 40 to 50 processes that myelinate numerous segments of axons and provide fast saltatory conduction of action potentials along axons at the nodes of Ranvier where  $\text{Na}^+$  channels are clustered.<sup>3,4,6</sup> Myelin is composed of approximately 75 – 80% lipids and 20 – 25% proteins with myelin basic protein (MBP) and proteolipid protein (PLP) as the major protein components whereas some minor proteins are myelin oligodendrocyte glycoprotein (MOG), myelin-associated glycoprotein (MAG), and cyclic nucleotide phosphohydrolase (CNPase).<sup>3</sup>

Activated macrophages, microglia and  $\text{CD8}^+$  T cells are believed to cause damage to myelin sheaths because they release cytotoxic factors such as proinflammatory cytokines, oxygen radicals, nitric oxide (NO), excitatory amino acids, or proteolytic and lipolytic enzymes.<sup>2,7,14</sup> B cells differentiate into plasma cells following activation and secrete antibodies against CNS antigens. Antibodies cause tissue damage by binding to myelin antigens and activating the complement cascade.<sup>2,13,16</sup> Complement proteins interact with one another and other molecules to generate an immune response that involves the insertion of a membrane attack complex into the cell membrane resulting in lysis.<sup>21</sup> Macrophages also recognize and bind to the antibodies, which triggers phagocytosis of the myelin antigen.<sup>21</sup> Following these destructive events, macrophages engulf the myelin components that have been disrupted (summarized in Figure 1.1).

Astrocytes are stellate cells in the CNS that are known to provide structural support to surrounding neurons, but they are also involved in scar formation in areas of demyelination leading to the formation of MS plaques (Figure 1.2).<sup>4,8</sup> Glial fibrillary acidic protein (GFAP) is found within the intermediate filaments of astrocytes and is routinely used as an astrocytic marker.<sup>4</sup>

#### *1.1.3.3 Neurodegenerative Phase*

Demyelination leads to the reduction or loss of conduction of action potentials down axons resulting in the initial symptoms of MS.<sup>2</sup> Depending on the pathway affected, for example a motor or sensory tract, a disruption can lead to the loss of motor function or sensation, respectively. An upregulation of Na<sup>+</sup> and Ca<sup>2+</sup> channels and mitochondrial dysfunction contribute to axonal degeneration.<sup>13</sup> Axonal loss has been related to neurological disability seen in patients with MS.<sup>15</sup>

#### *1.1.4 Role of Cytokines in MS*

Cytokines play an important role in regulating immune and inflammatory responses by binding to target cells and altering their function.<sup>22</sup> The actions of cytokines often overlap and therefore they are sometimes found to be redundant or they may act antagonistically.<sup>23</sup> Th1 proinflammatory cytokines contribute to a cell-mediated immunity, whereas Th2 anti-inflammatory cytokines control humoral immunity.<sup>23</sup>

Chemotactic cytokines are commonly known as chemokines, which are small peptides (7 – 10kD) that act as signals to direct leukocyte/mononuclear cell migration

during an immune response by forming concentration gradients.<sup>24</sup> Chemokines generally have four cysteine residues that form two disulfide bonds. They are classified according to the arrangement of cysteine residues close to the N-terminus, being CC, CXC, CX<sub>3</sub>C and C where X represents an amino acid.<sup>25-27</sup> A wide range of cells produce chemokines, such as monocytes/macrophages, lymphocytes, neutrophils, fibroblasts, endothelial cells, keratinocytes, and astrocytes.<sup>24</sup>

The proinflammatory cytokines interferon (IFN)- $\gamma$ , tumor necrosis factor (TNF)- $\alpha$ , interleukin (IL)-12, and lymphotoxin (LT)- $\alpha$  are upregulated in MS and therefore likely have a role in disease initiation or progression.<sup>23</sup> LT- $\alpha$  and TNF- $\alpha$  were present in acute and chronic active MS lesions<sup>19,28</sup> and higher levels of cytokine mRNA in peripheral blood monocytes were found in patients during a relapse than in remission.<sup>29</sup> An increased expression of TNF- $\alpha$  mRNA in peripheral blood monocytes has also been observed prior to a relapse.<sup>30</sup>

IFN- $\gamma$  is released by activated T cells and natural killer (NK) cells and has been found in active MS lesions, mainly expressed by astrocytes and T cells in the perivascular region.<sup>4,19</sup> IFN- $\gamma$  has been found to activate macrophages, stimulate the expression of MHC class I and II proteins on endothelial cells and astrocytes,<sup>31</sup> and induce the synthesis of adhesion molecules and NO.<sup>4</sup>

The anti-inflammatory cytokines transforming growth factor (TGF)- $\beta$  and IL-10 are found to be downregulated in MS prior to a relapse in patients with relapsing-remitting MS.<sup>23,30</sup>

### *1.1.5 Approved Treatments for MS*

Immunosuppressants have been used to treat MS and have been classified as intracellular ligands, cell surface ligands, and anticytokines.<sup>32</sup> Intracellular ligands include calcineurin inhibitors (cyclosporine A), antimetabolites (methotrexate), and antiproliferative agents (cyclophosphamide, mitoxantrone).<sup>17,32</sup> Cell surface ligands mostly function to block adhesion molecules and include monoclonal antibodies (natalizumab).<sup>33</sup> Anticytokines act against TNF- $\alpha$  and many proinflammatory interleukins.<sup>32</sup>

Current treatments for MS, such as IFN- $\beta$  and glatiramer acetate (GA), are immunomodulatory agents that cause a shift in cytokine release from proinflammatory Th1 cytokines to anti-inflammatory Th2 cytokines.<sup>13,14,34</sup> IFN- $\beta$  decreases the production of the proinflammatory cytokine IFN- $\gamma$  (thereby blocking the upregulation of MHC-II) and inhibits T cell activation.<sup>13,18</sup> GA is a co-polymer containing a mix of four different amino acids and is believed to compete with antigens by binding to the MHC. GA stimulates a broad T cell response; however, GA-reactive T cells are shifted towards the Th2 subtype.<sup>13,18,35</sup>

## 1.2 Experimental Autoimmune Encephalomyelitis

### 1.2.1 EAE as a Model of MS

Experimental autoimmune encephalomyelitis (EAE) is an animal model of demyelinating disease of the CNS that is widely used to study features of MS. Various species such as mouse,<sup>36-39</sup> rat,<sup>40-43</sup> guinea pig,<sup>44-47</sup> Rhesus monkey,<sup>48</sup> and dog<sup>49</sup> have been used to produce the model. EAE is not a spontaneous disease like MS and is commonly induced by immunizing with CNS myelin peptides such as MBP, PLP, MOG, CNPase, or  $\alpha$ -B-crystalline emulsified in complete Freund's adjuvant (CFA)<sup>7,50</sup> or with myelin-specific CD4<sup>+</sup> T cells.<sup>51,52</sup> CFA contains oil (paraffin oil and mannide monooleate) mixed with attenuated mycobacterium that envelopes the protein making it more accessible for presentation.<sup>20,53</sup> The mycobacterium serves as a general stimulus to activate the immune response<sup>53</sup> and is found to increase disease severity and reduce the amount of time between injection and first signs of disease.<sup>20</sup> Some models use exposure to a virus as the method of inducing demyelination as the result of an immune response against viral proteins.<sup>53</sup>

EAE is an ascending paralytic disease where the tail and hind limbs are first affected followed by the forelimbs.<sup>52</sup> The autoimmune inflammatory responses generated in EAE are similar to events observed in MS, and include the infiltration of macrophages and T cells into the CNS and the breakdown of the BBB or blood-spinal cord barrier (BSB). Focal areas of inflammatory infiltrates<sup>54,55</sup> and demyelination<sup>47,56</sup> have been observed throughout the CNS in various models of EAE. Similarly to MS, the autoimmune inflammatory events in EAE are thought to be CD4<sup>+</sup> T cell

mediated,<sup>50,55</sup> but macrophages are believed to be responsible for the destruction of the myelin sheath that leads to the debilitating features.<sup>56,57</sup> Proinflammatory cytokines regulate immune interactions leading to an increased inflammatory response and the breakdown of the BBB and the activation of macrophages, CD8<sup>+</sup> T cells and NK cells.<sup>53</sup>

### *1.2.2 Contrasts between EAE and MS*

In EAE the antigen that triggers the autoimmune response in the CNS is known, whereas in MS the triggering factor is unknown. The B and T cell repertoire is also much more diverse in MS, whereas animal models of EAE commonly involve inbred animals and therefore do not reflect what might be observed in the outbred human population.<sup>1,58</sup> In both EAE and MS, CD4<sup>+</sup> and CD8<sup>+</sup> T cells are found within lesions of the CNS; however, in most EAE models CD4<sup>+</sup> T cells predominate.<sup>1</sup>

The disease progressions observed in models of EAE are in the form of a single acute episode or follow a relapsing-remitting pattern. Signs of disease often resolve in a few weeks in EAE, whereas MS is a chronic disease over a time frame of years. The shorter time frame of EAE studies does not allow the potential chronic side effects of treatments to be observed. The first relapse has also been reported to be more severe than subsequent relapses in some models of EAE, as opposed to a worsening of symptoms commonly observed in MS.<sup>56,59</sup>

### 1.3 Blood-Brain and Blood-Spinal Cord Barriers

The BBB protects the CNS against immune cells and macromolecules such as antibodies under normal conditions. Capillary endothelial cells, surrounded by a network of astrocytic foot processes (glia limitans) and a collagen matrix, make up the BBB.<sup>4,60</sup> Endothelial cells within the CNS have different properties than those found elsewhere; they have a greater number of mitochondria, lack fenestrations with reduced numbers of pinocytotic vesicles, and have tight junctions (zona occludens) located between adjacent endothelial cells.<sup>4,61</sup> Tight junctions between endothelial cells function to limit the paracellular movement of molecules across the BBB, while the reduced number of vesicles restricts the transcellular movement of molecules. A basal lamina surrounds the endothelium on the abluminal side of the endothelial cells (Figure 1.3).<sup>62</sup> Other cells types associated with the BBB, located in the perivascular (Virchow-Robin) space surrounding endothelial cells, are pericytes, neuron terminals, and microglia.<sup>63</sup>

Leukocytes are thought to migrate across the BBB and enter the CNS primarily at postcapillary venules, whereas solute diffusion occurs at the capillaries.<sup>61,64,65</sup> Postcapillary venules have different BBB properties than capillaries. A separate basement membrane is associated with the glia limitans in postcapillary venules (Figure 1.3), whereas the endothelial and glial basal laminas are fused at the level of the capillaries.<sup>66</sup> The glia limitans serves as the boundary of the parenchyma of the brain or spinal cord. The basal lamina of the endothelium and the glia limitans are separated by the perivascular space and associated cells. In order to enter the parenchyma of the

CNS, leukocytes must migrate across the endothelial cell barrier and the glia limitans. The BBB regulates the migration of leukocytes through the expression of adhesion molecules, chemokines, cytokines, and MMPs.<sup>61</sup> MMPs are known to disrupt the extracellular matrix of the BBB by digesting collagen fibres.<sup>67</sup> MMPs are secreted by macrophages and T cells and expressed by microglia, endothelial cells, and astrocytes.<sup>4</sup> Increased expression of MMPs has been observed in patients with MS and they are believed to play a role in the migration of inflammatory cells into the CNS by causing a disruption of the BBB.<sup>68-71</sup>

Tracers are commonly used to detect the permeability of the BBB (Table 1.1) through intravenous or cardiac injection followed by histological detection in the CNS. Dextran tracers have molecular weights typically ranging from 3 – 150kD and are often conjugated to a fluorescent marker such as fluorescein (FITC) to allow detection within the parenchyma.<sup>72</sup> Dextrans with different molecular weights have the advantage of determining the relative degree of vascular permeability while retaining the same chemical properties.

**Table 1.1. Tracers commonly used to detect vascular permeability**

Tracer	Molecular Weight (D)	Diameter (nm)
Evans Blue (binds to albumin) <sup>73-76</sup>	68,000	8
Dextrans <sup>72,73</sup>	3,000 – 150,000	2.4 – 17.4
Horseradish peroxidase <sup>38,46,47,73,77,78</sup>	40,000	5
Microperoxidase <sup>79</sup>	1,900	2
Gd-DTPA (MR contrast agent)	550	0.7
Sodium fluorescein <sup>73</sup>	376	0.5
Lanthanum <sup>79,80</sup>	139	0.2

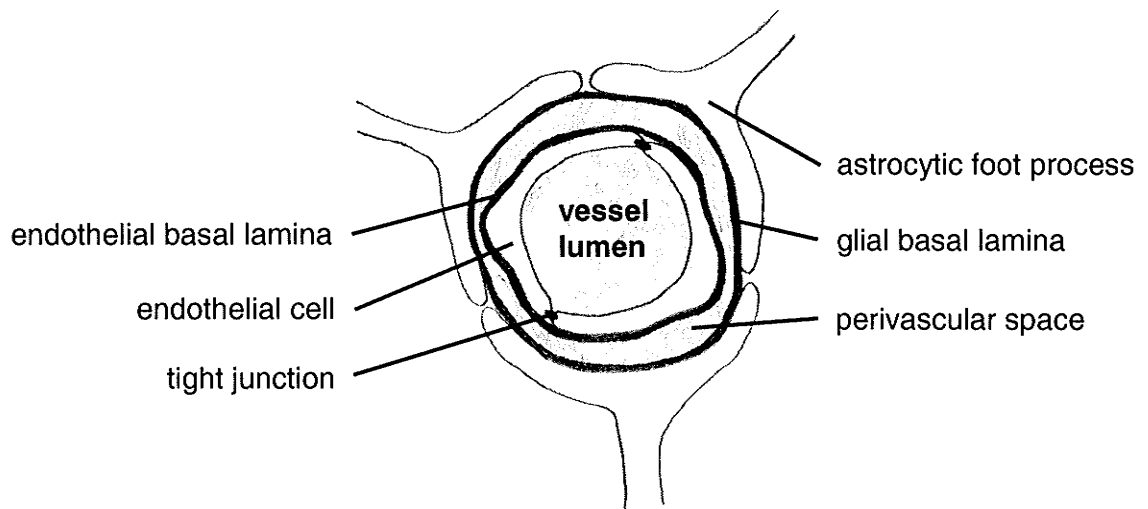


**Figure 1.3.** A schematic drawing of the anatomical structure of the BBB/BSB of a postcapillary venule.

## 1.4 Magnetic Resonance Imaging

### 1.4.1 Protons and Magnetism

A proton has angular momentum and a magnetic moment characterized by the spin quantum number  $m_s = \pm 1/2$ .<sup>81-83</sup> In an environment where an external magnetic field is not present, these magnetic moments are randomly oriented and the result is no net magnetic moment. However, when protons are placed in an external magnetic field ( $B_0$ ), the magnetic moments precess around  $B_0$  with an alignment either along or against the direction of  $B_0$  (labelled as the z axis) and with an extremely small excess oriented along the direction of  $B_0$ .<sup>81-83</sup> The orientation along  $B_0$  is favoured because it has a lower energy state and the excess in proton magnetic moments creates a net magnetization ( $M_0$ ) along the z axis. The precession frequency ( $f$ ), known as the Larmor frequency, is proportional to the strength of  $B_0$ :

$$f = \gamma B_0$$

where  $\gamma$  is the gyromagnetic ratio (42.6 MHz/T in the case of hydrogen).<sup>81-83</sup> When protons are placed in  $B_0$  they precess randomly out of phase and therefore there is no net magnetization in the transverse xy plane ( $M_{xy}$ ).<sup>83</sup>

### 1.4.2 Radiofrequency Pulses and Spin Relaxation

Net magnetization along the z axis cannot be detected because it is not an oscillating signal and therefore a radiofrequency pulse (RF) transmitted by a coil is used to flip the magnetization into the xy plane.<sup>83</sup> When the RF pulse is applied in the xy plane at the Larmor frequency, the proton magnetic moments precess in sync or in

phase with one another,<sup>81-83</sup> and effectively precess about the magnetic field component ( $B_1$ ) of the RF pulse. To simplify the description of net magnetization a rotating frame of reference can be considered, which is a coordinate system that rotates about  $B_0$  at the Larmor frequency.

For a  $90^\circ$  RF pulse,  $B_1$  is applied long enough to cause the magnetization  $M_0$  to flip into the  $xy$  plane (Figure 1.4) and  $M_{xy}=M_0$ .<sup>83</sup> Magnetic moments of protons in the  $xy$  plane are precessing in phase in the magnetic field  $B_1$  in the rotating frame. After the RF pulse is turned off the magnetization relaxes back to equilibrium. During relaxation two independent processes occur at different rates. The  $xy$  component of the net magnetization  $M_{xy}$  decreases with time until  $M_{xy}=0$  and the  $z$  component  $M_z$  increases until  $M_z=M_0$ . The rate at which  $M_z$  increases with time as magnetic moments relax back to equilibrium is characterized by the time constant  $T_1$ , the longitudinal or spin-lattice relaxation time (Figure 1.5A), and is caused by the interaction and transfer of energy from the hydrogen proton to the surrounding molecules.<sup>81-83</sup>

$$M_z(t) = M_0 (1 - e^{-t/T_1})$$

The rate at which  $M_{xy}$  decreases with time as protons relax back to equilibrium is characterized as the time constant  $T_2$ , the transverse or spin-spin relaxation time (Figure 1.5B), which is caused by the interaction and energy exchange between individual hydrogen protons resulting in the loss of phase coherence of precessing protons.<sup>81-83</sup> After the RF pulse is turned off this phase coherence between precessing protons will be lost due to small differences in the magnetic field surrounding each proton called field inhomogeneities that cause the protons to precess at slightly different frequencies.<sup>82</sup>

$$M_{xy}(t) = M_0 e^{-t/T_2}$$

$T_2$  relaxation times are shorter than  $T_1$  relaxation times.<sup>81</sup> When  $M_z = M_0$  there cannot be any magnetization remaining in the xy plane.

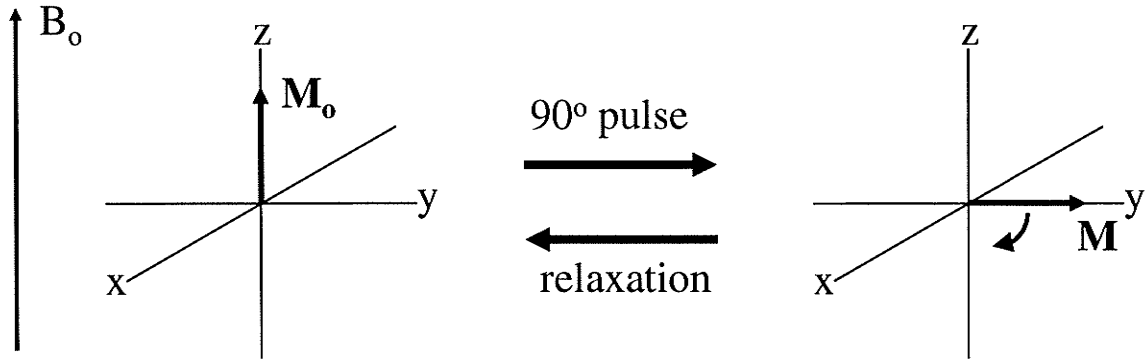


**Figure 1.4.** The net magnetization vector  $M_0$  flips into the xy plane following a  $90^\circ$  RF pulse.

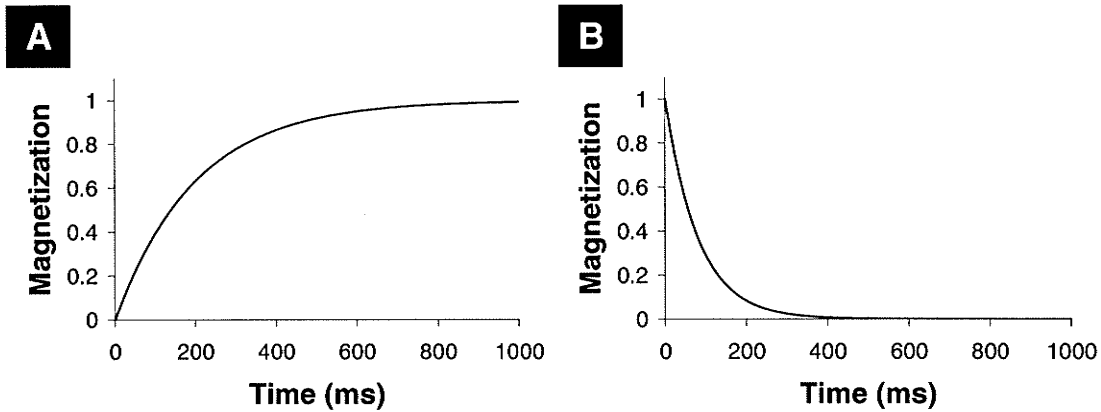


**Figure 1.5.** (A) The relative recovery of longitudinal magnetization with time constant  $T_1$  and (B) decay of transverse magnetization with time constant  $T_2$  following a  $90^\circ$  RF pulse. Diagram is provided courtesy of Dr. Richard Buist.

A  $180^\circ$  pulse applied at equilibrium causes the net magnetization to flip into the negative z direction.<sup>83</sup>

The oscillating signal in the xy plane following an RF pulse induces a small current in the receiver coil. The signal that is created is called free induction decay (FID) and decreases with time as the magnetic moments relax back to the positive z direction.<sup>81</sup> The FID is a signal acquired in the time domain and is converted into the frequency domain by Fourier transformation.<sup>82</sup> This frequency domain is called k-space, which a computer converts into spatial information used to produce an MR image.

### *1.4.3 Magnetic Field Gradients*

Gradients are magnetic fields that change linearly along a certain axis and they can be applied in each of the x, y, and z directions. Pulsed gradient magnetic fields are used to obtain spatial information such as slice selection and pixel location within the slice.<sup>81,83</sup> The precession frequency of  $M_0$  is directly proportional to the magnetic field strength, which gives the magnetic moments at each pixel location a unique frequency depending on the location along the gradient.<sup>83</sup>

### *1.4.4 Pulse Sequences*

Some common pulse sequences are partial saturation, inversion recovery, spin echo, gradient echo, and echo planar.<sup>81</sup> The focus here will be on the spin echo (SE) pulse sequence which was used in all MR imaging studies to follow.

Due to limitations of electronics, the MR signal cannot be measured immediately following the 90° pulse.<sup>83</sup> Therefore, the SE sequence begins with a 90° RF pulse, but needs to be followed by a 180° refocusing RF pulse.<sup>81,83</sup> After the 90°

pulse, which causes  $M_0$  to flip into the xy plane, some magnetic moments will precess at a higher frequency, while other magnetic moments will precess at a lower frequency because of inhomogeneities in  $B_0$ .<sup>83</sup> These small differences in precession cause the magnetic moments to dephase as the protons that precess at a slower rate fall behind and those that precess at a faster rate move ahead. A  $180^\circ$  pulse causes the net magnetization to flip  $180^\circ$  as individual precessing magnetic moments rotate  $180^\circ$  in the xy plane, which causes precession to continue in the opposite direction. As a result, the magnetic moments precessing at a faster rate are placed behind those that are precessing at a slower rate and over time they come back into phase forming an echo.<sup>83</sup> The  $180^\circ$  RF pulse can be repeated which generates another SE that is smaller in amplitude than the previous one because of  $T_2$  decay.<sup>81</sup> The echo time (TE) is the time between the first  $90^\circ$  pulse and the SE. The repetition time is the time between  $90^\circ$  RF pulses, whereas recovery time (TR) is the time between the last pulse of a given scan and the first pulse of the next scan.

#### *1.4.5 $T_1$ - and $T_2$ -weighted Imaging*

Tissue characteristics that are important in creating an MR image are proton density (PD), the spin-lattice relaxation time  $T_1$ , and the spin-spin relaxation time  $T_2$ . The properties of different tissues result in different values of PD,  $T_1$  and  $T_2$ .

In the case of water there is minimal spin-spin interaction between magnetic moments because of the large distance between molecules resulting in slow dephasing of spins and a long  $T_2$ .<sup>83</sup> Solids contain molecules that are more compact, which results in more spin-spin interactions and more dephasing of spins with a short  $T_2$ .<sup>83</sup> In fat and

proteinaceous tissue there is more dephasing than in water, but not to the extent found in solids and therefore the  $T_2$  value is intermediate.<sup>83</sup>

$T_1$  relaxation values are dependent on the ability of the tissue to transfer energy from the protons to the surrounding molecules. This energy transfer occurs most readily when motional frequencies of the protons are at the Larmor frequency.<sup>83</sup> In water the motional frequencies are faster than the Larmor frequency, in solids the motional frequencies are slower, and in fat the motional frequencies are about equivalent to the Larmor frequency and therefore  $T_1$  values are long, intermediate, and short respectively.<sup>83</sup>

MR images can be weighted by PD,  $T_1$ , or  $T_2$  by changing the values of TR and TE. A  $T_2$ -weighted image has a long TR and a long TE, whereas a  $T_1$ -weighted image has a short TR and a short TE and a PD-weighted image has a long TR and a short TE.<sup>81</sup> In  $T_1$ -weighted images, tissue with a short  $T_1$  will appear bright and tissue with a long  $T_1$  will appear dark, whereas in  $T_2$ -weighted images, tissue with a long  $T_2$  will appear bright and tissue with a short  $T_2$  will appear dark. The longer the TE, the more  $T_2$ -weighted the image becomes.<sup>81</sup>

#### *1.4.6 Magnetization transfer-weighted Imaging*

Magnetization-transfer (MT)-weighted imaging detects tissue degradation (demyelination) and edema. Protons within macromolecules (such as myelin) and protons within water molecules that are bound to macromolecules have a broad range of resonance frequencies with short  $T_2$  (less than 1ms), so that they are not detected in most MR imaging experiments.<sup>81,84</sup> Therefore, bound water protons do not directly

contribute to the MR signal. MT saturation pulses are off-resonance pulses (1000 to 2000 Hz away from the Larmor frequency of free water protons) that saturate the MR signals of protons in water bound to macromolecules.<sup>83,84</sup> Chemical exchange with protons on free water causes a transfer in the saturation and a reduction in the signal.<sup>83</sup> Therefore, tissue with a greater concentration of macromolecule-bound water will have a greater signal loss. The magnetization transfer ratio (MTR) is dependent on the structural integrity of white matter within the CNS and a reduction in the MTR has been correlated with demyelination in models of EAE<sup>85</sup> and in post mortem human brain studies.<sup>86</sup> A low MTR indicates there is less exchange of magnetization between bound and free water protons.

#### *1.4.7 Gadolinium Contrast Agent*

Gadolinium diethylene-triamine-pentaacetate (Gd-DTPA) is a paramagnetic contrast agent made up of  $Gd^{3+}$  that is chelated with DTPA in order to reduce its toxicity (Figure 1.6). Gadolinium is a member of the lanthanide group of the periodic table and it has 7 unpaired electrons, which create a strong local magnetic field that causes a significant shortening in  $T_1$  relaxation time with some shortening effects in  $T_2$  relaxation time.<sup>81-83</sup> Gd-DTPA follows an extracellular non-specific biodistribution and it does not pass through an intact BBB or BSB. Gadolinium-enhanced MRI can detect changes in the extent of BBB or BSB disruption in diseased tissue.

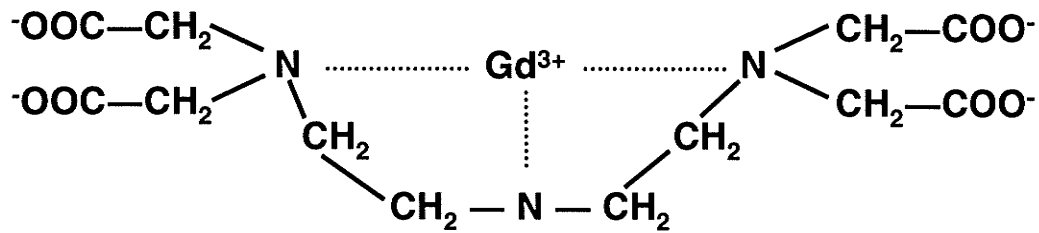


**Figure 1.6.** The molecular structure of Gd-DTPA.

#### 1.4.8 MRI in MS and EAE

MRI has become a valuable tool in monitoring disease progression<sup>87,88</sup> and effectiveness of treatments in clinical trials for patients with MS. T<sub>2</sub>-weighted MR images have conventionally been used to determine the lesion load within the CNS of patients with MS; whereas T<sub>1</sub>-weighted contrast-enhanced MR images identify active lesions. MS lesions typically appear hyperintense on T<sub>2</sub>-weighted MR images, representing a range of underlying pathology such as inflammation, edema, demyelination, and axonal loss.<sup>89,90</sup> Some lesions also appear hypointense on T<sub>1</sub>-weighted MR images, often referred to as black holes, and studies have found histological correlation to axonal loss, edema and demyelination.<sup>89</sup>

Various studies of EAE have shown a correlation between the number of Gd-enhancing lesions and the severity of disease.<sup>91</sup> Histological assessment of the CNS of animals with EAE showed that contrast enhancement on T<sub>1</sub>-weighted images correlates with active inflammation.<sup>43,49,54,92,93</sup> Early active lesions on T<sub>1</sub>-weighted contrast-enhanced MR images from patients with MS have extensive enhancement, indicating that BBB disruption is an important early finding in newly developed lesions<sup>89,94-96</sup> and has been found to precede changes on T<sub>2</sub>-weighted MR images.<sup>95,97</sup> The number of

enhancing lesions on contrast-enhanced T<sub>1</sub>-weighted MR images can also be used to predict the occurrence of future relapses and clinical worsening.<sup>98-100</sup> For example, IFN-β has been found to reduce clinical disease symptoms and decrease the number of enhancing lesions using MRI.<sup>101</sup>

MT-weighted MRI of normal-appearing white matter within the brain of patients with MS<sup>102-105</sup> and animals with EAE<sup>106</sup> has shown a significantly lower MTR than is found within the white matter of healthy subjects or control animals. MTR values within the area of contrast-enhanced lesions identified on T<sub>1</sub>-weighted images were found to decrease at the time of enhancement.<sup>107,108</sup> Subsequent decreases and increases in MTR were consistent with demyelination and remyelination respectively.<sup>107</sup> Other human studies have also found that lesions identified with conventional MR imaging have a significantly decreased MTR.<sup>104,105</sup> In a Lewis rat model of EAE, a decrease in MTR was correlated histologically with monocyte infiltrates in brain parenchyma, suggesting their contribution in demyelination<sup>56,59</sup> and similar observations were noted in a marmoset model of EAE.<sup>109</sup> Areas of inflammation and demyelination seen histologically within the spinal cord of a guinea pig model of EAE correlated with a decrease in MTR.<sup>85</sup> Myelin content correlated with MTR within MS lesions in a study of MT-weighted imaging of post-mortem human brains where an increased MTR was found in remyelinated lesions relative to lesions that remained demyelinated.<sup>110</sup>

## **CHAPTER II**

### **HYPOTHESIS AND OBJECTIVES**

## 2.1 HYPOTHESIS

MRI can be used to monitor changes *in vivo* in BBB/BSB permeability and demyelination in the CNS of mouse models exhibiting features of MS, and to assess the effect of genetic alterations and pharmacological intervention on the disease state.

## 2.2 SPECIFIC OBJECTIVES

A series of MR imaging experiments was conducted in order to study mouse models of CNS inflammation similar to MS. The studies involved MRI of the spinal cord in a mouse model of EAE, except in the second study which used MRI of the brain to study inflammation induced in mice with an upregulated chemokine.

The specific objectives or goals of each study were:

### *Study #1*

- To develop a reproducible procedure for imaging of mouse spinal cord that applies T<sub>1</sub>-weighted contrast-enhanced MRI while the mouse remains undisturbed in the magnet.
- To evaluate relative changes in BSB disruption during EAE and to investigate the correspondence of such changes with clinical signs and histological features of disease.

### *Study #2*

- To determine the relative extent and time course of BBB permeability in the brain of transgenic mice with an upregulated chemokine before and after pertussis toxin (PTx)-induced CNS inflammation, and in wild type control mice.

*Study #3*

- To compare the BSB permeability in A1 adenosine receptor (A1AR) knockout mice and in wild type mice with EAE using T<sub>1</sub>-weighted contrast-enhanced MRI of the spinal cord.

*Study #4*

- To determine whether MT-weighted MRI can detect changes within the white matter of the spinal cord in diseased versus pre-diseased mice following the induction of EAE.
- To apply T<sub>1</sub>-weighted contrast-enhanced and MT-weighted MRI to determine the effect of a drug treatment on changes in BSB disruption and demyelination in the spinal cord of mice with EAE.

## **CHAPTER III**

### **GENERAL METHODOLOGY**

All animal procedures were approved by the Institutional Animal Care Committee at the University of Manitoba.

### **3.1 Induction of EAE**

All the mice that were used in studies of EAE were female. Daily handling of mice began one week before experiments began in order for the mice to become familiar with being handled as well as with the individual performing the daily scoring. A solution of a 21 amino acid peptide fragment of MOG<sub>35-55</sub> (synthesized by the Peptide Facility of the University of Calgary; 0.5 mg/mL in phosphate buffered saline (PBS)) was mixed 1:1 with CFA (Sigma-Aldrich, Saint Louis, MO) in an air tight system of two 5mL glass syringes connected by a stopcock. To induce EAE, on day 0 each mouse received two 50 µL subcutaneous injections of the MOG mixture near the base of the tail.<sup>111,112</sup> Additionally, each animal received a 200 µL intraperitoneal injection of 0.3 µg PTx (List Biological Laboratories, Campbell, CA) in PBS, which was repeated on day 2. The exact mechanism of PTx in the induction of EAE is unknown; however, PTx is believed to increase BBB/BSB permeability, perhaps by increasing the sensitivity to vasoactive amines such as histamine or serotonin,<sup>113</sup> and to cause greater disease severity. Previous studies comparing the effects of EAE induction with and without PTx showed that animals receiving PTx had an earlier onset of disease signs with increased BBB permeability compared to mice that were induced without PTx.<sup>37,113</sup> Animals were allowed free access to food and water for the duration of the experiment and were housed in individual cages.

### 3.2 Scoring System

All mice were weighed and the neurological condition was evaluated daily each morning. A scoring system with a scale of 0 to 14 was used<sup>114</sup> where individual scores from the tail and each limb were summed to give a total score. For the tail, a mouse retaining the ability to wrap the tail tightly around the examiner's finger and showing no sign of impairment was given a score of 0 (Figure 3.1A,B), 1 indicated signs of weakness in the tail, and 2 indicated complete paralysis of the tail (Figure 3.1C,D). Each limb was scored separately, with 0 indicating no loss of function, 1 representing weakness of grip when suspended from the examiner's hand and an abnormal posturing during ambulation, 2 indicating dragging and partial paralysis of the limb (Figure 3.1E), and 3 indicating complete paralysis (Figure 3.1F,G). When mice first exhibited a score of 1 in the tail, wetted chow was placed at the bottom of the cage along with bacon softies so that mice could easily access the food. Mice received a 1 mL subcutaneous injection of saline daily starting when mice first showed signs of hind limb weakness (score=1). A mouse that exhibited a limp tail, complete paralysis of hindlimbs, and forelimbs that were unable to support its weight when it was first observed in the morning, was observed more frequently throughout the day. If signs persisted with no improvements, the mouse was said to have reached endpoint and was sacrificed at the end of the day.

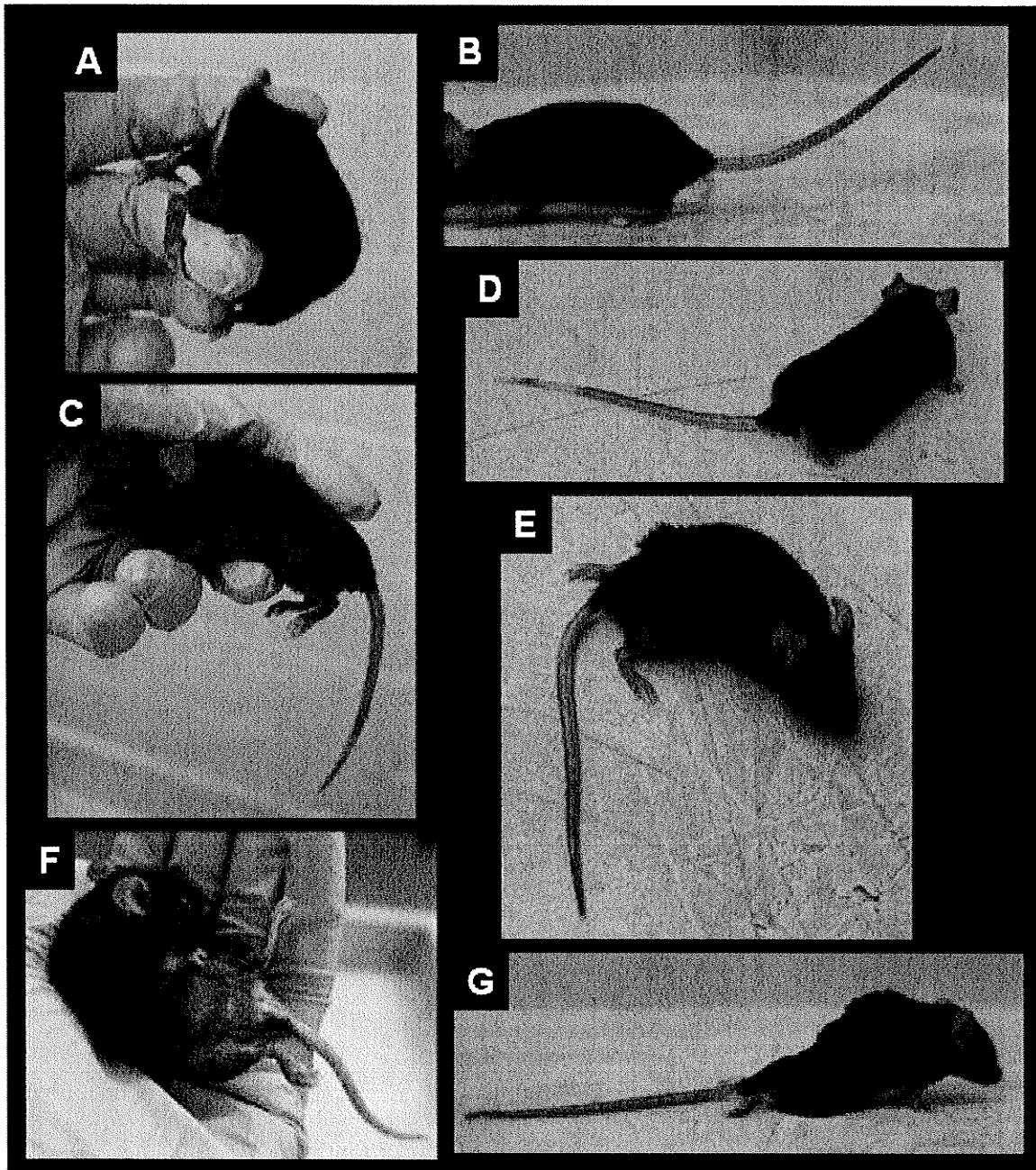


**Figure 3.1.** (A) A healthy mouse indicating the ability to grasp with its hind limbs and wrap its tail around the examiner's finger and (B) tail showing no signs of impairment. (C) A mouse at initial stages of disease with a floppy tail and (D) still retaining hind limb function. (E) A mouse with dragging hind limbs (score=2 in each) and floppy tail. (F) A mouse at peak disease showing the loss of a righting reflex and (G) complete paralysis of hind limbs (score=3 in each).

### 3.3 Magnetic Resonance Imaging

All MRI experiments were performed using a Bruker Biospec spectrometer with a 7T/21cm magnet (Figure 3.2A). Anesthesia was induced by ventilating the mouse within an induction chamber with 5% halothane or isoflurane in O<sub>2</sub>/N<sub>2</sub>O (30/70) and was maintained during imaging using 1.5-2% halothane or isoflurane delivered via a nose cone. The respiratory rate of each mouse was monitored using an HP 78212D Neonatal Respiratory monitor with a respiratory pillow (SA Instruments) positioned under the animal and the anesthetic was adjusted in order to maintain a rate between 70 and 120 respirations per minute. The body temperature of the mice was also monitored during examination using a thermometer (Cole-Parmer Model No. 7002HT) with a rectal thermal probe (Geneq) and was air controlled by blowing hot or cold air around the animal in order to maintain a temperature of  $37 \pm 1$  °C. MR images of the lumbar spinal cord were obtained using either a 2cm × 3cm quadrature surface coil (Figure 3.2B) or a 2cm diameter quadrature volume coil (Figure 3.2C) depending on the imaging protocol, while MR images of the brain were obtained using the quadrature volume coil. In the volume coil mice were in the prone position with the head centered in the coil, while on the surface coil mice were in the supine position with the kidney region centered on the coil.

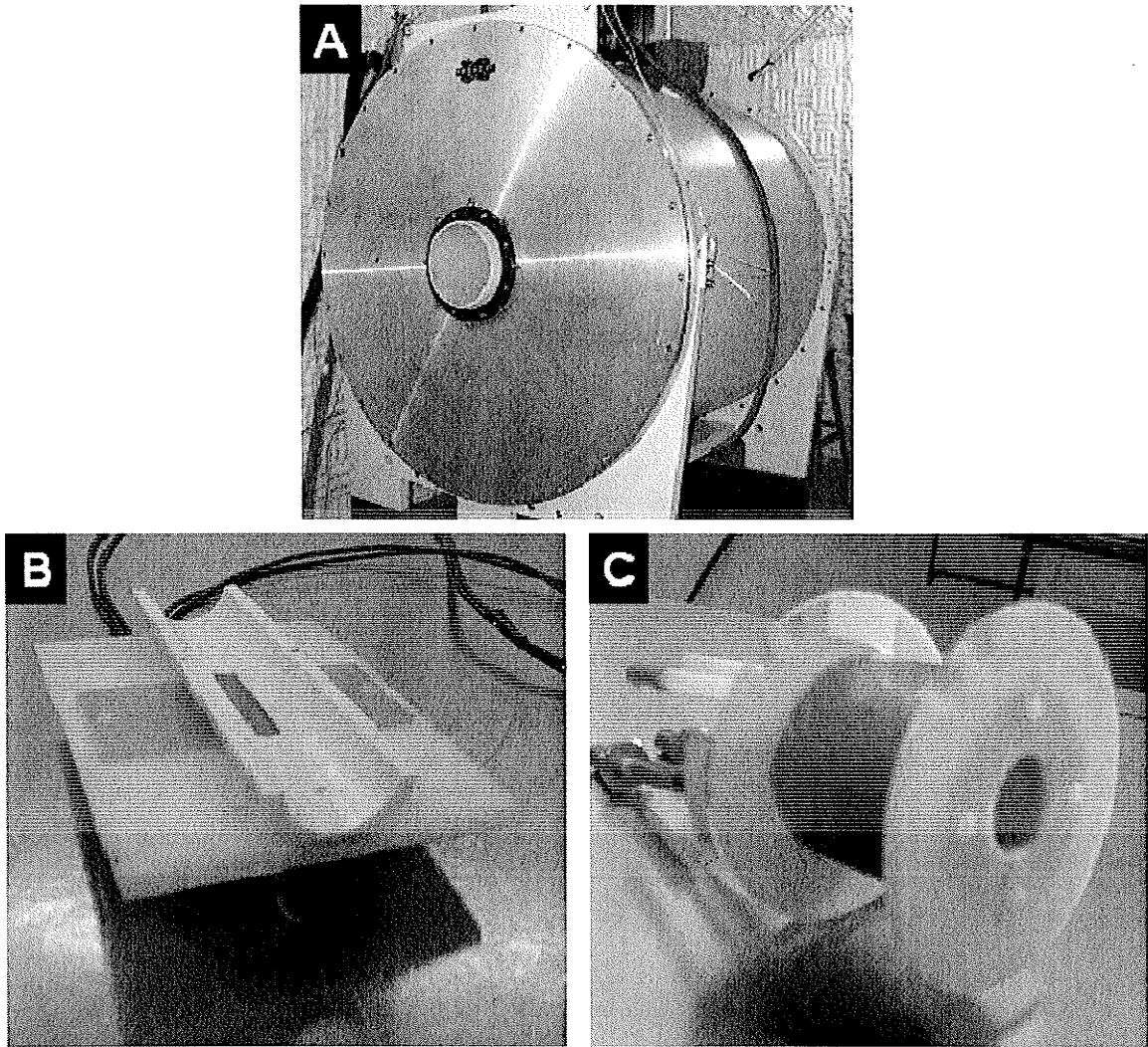


**Figure 3.2.** (A) Bruker Biospec 7T/21cm magnet used for all imaging experiments. (B) Surface coil (2cm  $\times$  3cm) used to obtain MR images of the lumbar spinal cord. (C) Quadrature volume coil used to acquire MR images of the lumbar spinal cord and brain.

### 3.3.1 $T_2$ -weighted MR Imaging

$T_2$ -weighted MR images were obtained using a multi-slice multi-echo sequence (8 echoes evenly spaced by 26.8 ms, TR=2300 ms, matrix size=256×256, field of view (FOV)=2.5×2.5 cm<sup>2</sup>, slice thickness=0.75 mm, 8 echoes, 2 averages). TR was selected by adjusting for optimal signal-to-noise ratio with minimal  $T_1$  weighting. The value of  $T_2$  at 7T has previously been determined to be 44ms and 35ms within the grey and white matter of mouse spinal cord respectively.<sup>115</sup>

### 3.3.2 $T_1$ -weighted contrast-enhanced MR Imaging

Initially a 30 gauge cannula attached to a syringe filled with saline was inserted into the tail vein of each mouse. A small bolus of saline was injected to ensure the correct placement of the cannula within the vein. Then the syringe containing saline was replaced with one contained the gadolinium contrast agent. The cannulation and syringe was secured tightly to the tail using adhesive tape.  $T_1$ -weighted images were acquired using a multi-slice SE sequence (TE=13.0 ms, TR=600 ms, matrix size=256×256, FOV=2.5×2.5 cm<sup>2</sup>, slice thickness=0.75 mm, 4 averages) before the injection of a contrast agent. A bolus of 0.4mmol/kg Gd-DTPA (dimeglumine salt, Berlex Canada, 0.5 mmol/mL) was injected through the tail vein cannula while the mouse remained undisturbed in the magnet. Contrast-enhanced  $T_1$ -weighted images were obtained immediately following the Gd-DTPA administration, using the same acquisition parameters as for the pre-contrast-enhanced MR images (acquisition time 10 minutes). The TR was selected by compromising between the signal-to-noise ratio and  $T_1$  contrast. Linear phase encoding was used, resulting in maximum signal being

detected 5 minutes after starting the acquisition. The value of  $T_1$  at 7T has previously been determined to be 1650ms and 1450ms within the grey and white matter of mouse spinal cord respectively.<sup>115</sup>

### *3.3.3 MT-weighted MR Imaging*

MT-weighted images were obtained using a multi-slice SE sequence preceded with off-resonance saturation (TE=10 ms, TR=1500 ms,  $B_1=20 \mu\text{T}$ , saturation pulse offset=+6000 Hz, slice thickness=0.75 mm, 4 averages) followed by a second set without saturation. Saturation pulses were applied during the inter-slice gaps with duration of 221 ms and a duty cycle of 88%.

### *3.3.4 Slice positioning*

#### *3.3.4.1 Imaging of the spinal cord using two sets of interleaved slices*

Eleven contiguous MR images spanning 8.25 mm of the lumbar spinal cord were obtained in two interleaved sets (interslice gap=0.75 mm) to minimize inter-slice excitation. In order to obtain reproducible image positions, disc 21 of the spinal column, located at the level of the kidneys (Figure 3.3A), was centered between slices 2 and 3 (slice 1 being the most anterior slice; Figure 3.3B) of the first set of 6 slices.

#### *3.3.4.2 Imaging of the spinal cord using a single set of slices*

A single set of six MR images spanning 5.5 mm of the lumbar spinal cord (interslice gap=0.2 mm) was acquired. For reproducible image positioning, the slices

were positioned at the rostral end of the kidneys (Figure 3.3C) and disc 21 of the spinal column was centered on slice 6 (Figure 3.3D).

#### *3.3.4.3 Imaging of the brain*

A set of eight MR images spanning the brain was obtained with an interslice gap of 0.25 mm. Slices were reproducibly positioned with exactly 1 mm between the notch posterior to the olfactory bulbs and the edge of the first slice (Figure 3.3E,F).

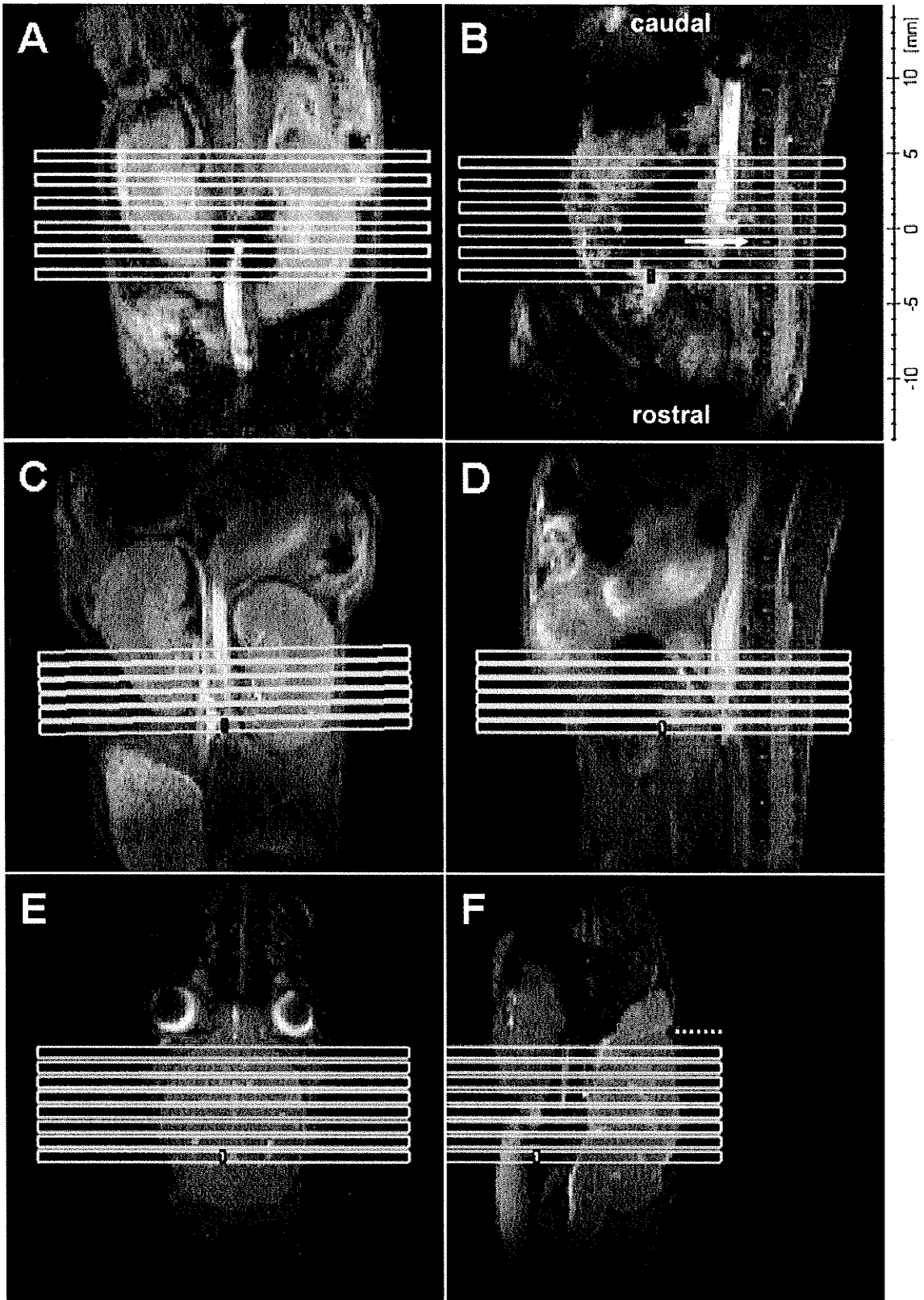


**Figure 3.3.** (A) A horizontal MR image of a mouse showing the slice positions of the first set of interleaved MR images used to examine the lumbar spinal cord at the level of the kidney and (B) the corresponding sagittal MR image where the arrow indicates the position of intervertebral disc 21 located between slices 2 and 3, used to obtain reproducible slice positioning. (C) A horizontal MR image of a mouse showing the slice positions of a single set of images with an interslice gap distance of 0.2mm located at the rostral end of the kidneys and (D) the corresponding sagittal MR image showing the position of intervertebral disc 21 located on slice 6. (E) A horizontal MR image of a mouse showing the slice positions of the MR images used to examine the brain and (F) the corresponding sagittal MR image. The furthest anterior slice was positioned 1mm posterior to the notch at the olfactory bulbs indicated by the dotted line.

### 3.4 MR Image Processing

#### 3.4.1 $T_2$ -weighted MR Images of the Spinal Cord

Regions of interest (ROIs) outlining the spinal cord were determined from the 5<sup>th</sup> echo (TE=134ms) of  $T_2$ -weighted images, in which the spinal cord was clearly distinguished from the surrounding CSF and nerve roots (Figure 3.4), using Marevisi (National Research Council, Canada) software.

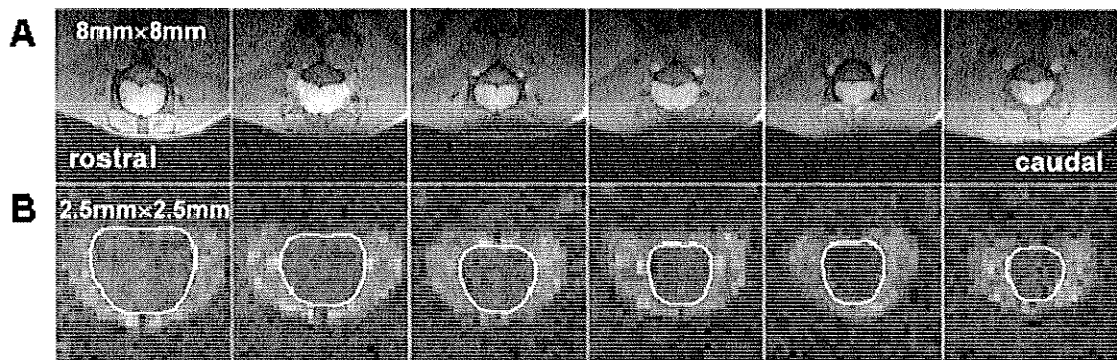


**Figure 3.4.**  $T_2$ -weighted MR images (A, TE = 26.8 ms; B, TE = 134 ms) of the mouse spinal cord. The ROI consisting of the spinal cord, clearly differentiated from surrounding CSF and nerve roots in the more strongly  $T_2$ -weighted images in B, is outlined.

#### 3.4.2 $T_2$ -weighted MR Images of the Brain

$T_2$ -weighted images (TE=80.4ms; Figure 3.5A) were used to define the ROI outlining the brain and omitting the ventricles (Figure 3.5B) using Marevisi software. The ventricles were omitted from the ROI since they were found to enhance on contrast-enhanced  $T_1$ -weighted images.

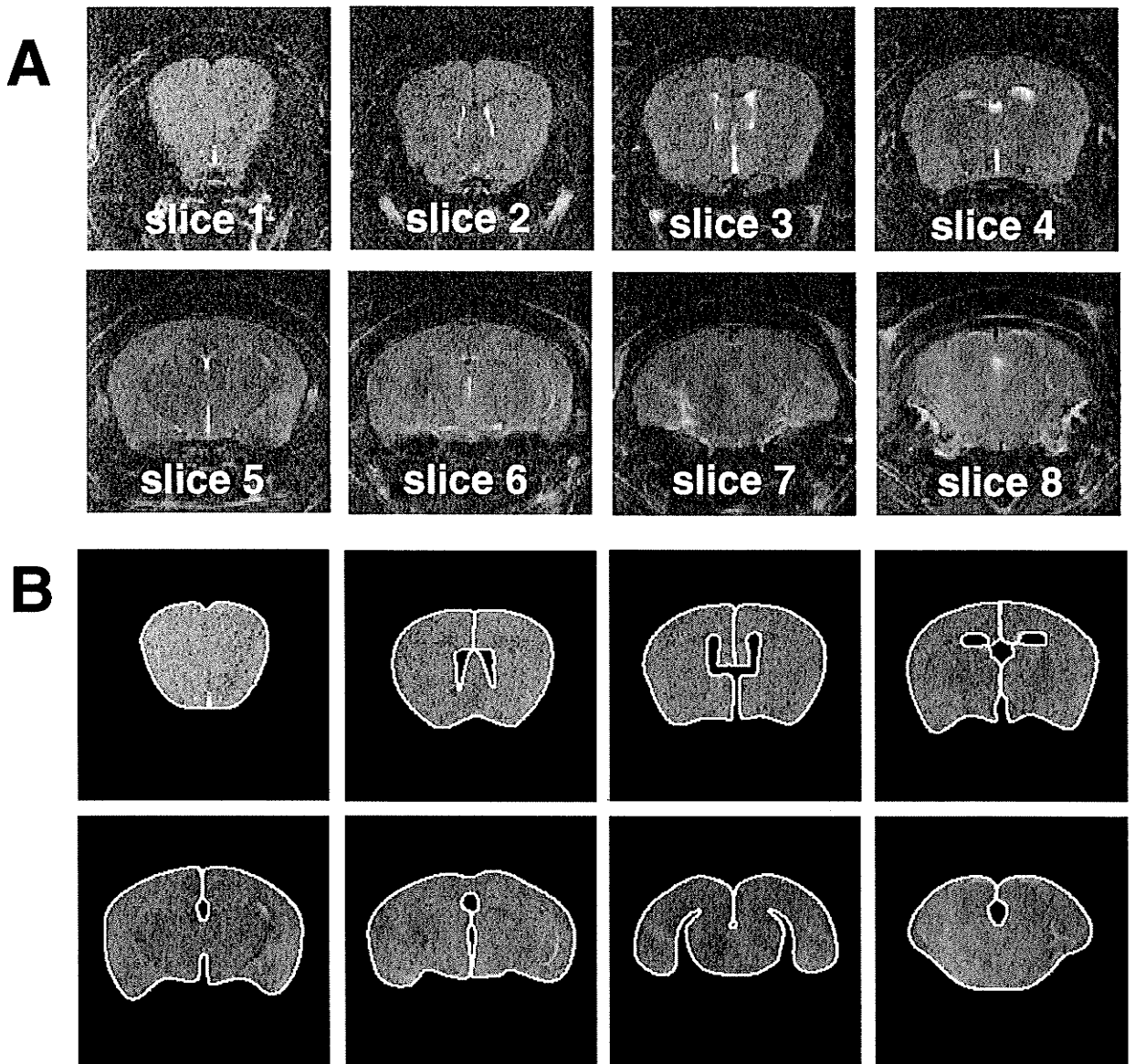


**Figure 3.5.** (A) Coronal T<sub>2</sub>-weighted MR images (TE=80.4ms) were used to define the area of the brain and omitting the ventricles as shown in (B).

### *3.4.3 T<sub>1</sub>-weighted contrast-enhanced MR Images of the Spinal Cord*

The percent intensity increase due to contrast enhancement was calculated voxel-by-voxel using the T<sub>1</sub>-weighted MR images obtained pre- and post-Gd-DTPA injection as

$$\frac{\text{post-contrast image} - \text{pre-contrast image}}{\text{pre-contrast image}} \times 100\%.$$

The ROIs determined from T<sub>2</sub>-weighted images were then superimposed onto the calculated percent enhancement images to quantify the average percent intensity increase within the spinal cord. The kidneys and other surrounding tissue consistently showed elevated intensity on T<sub>1</sub>-weighted images following successful Gd-DTPA injection.

### *3.4.4 T<sub>1</sub>-weighted contrast-enhanced MR Images of the Brain*

The contrast enhancement on T<sub>1</sub>-weighted images was quantified by calculating percent difference images using the same formula used for images of the spinal cord (Section 3.4.3). ROIs determined from corresponding T<sub>2</sub>-weighted images were superimposed onto the calculated images of percent enhancement to obtain the number of pixels above any given selected intensity threshold.

### *3.4.5 MT-weighted MR Images of the Spinal Cord*

ROIs outlining the spinal cord as determined from T<sub>2</sub>-weighted images were superimposed onto corresponding MT-weighted images that were obtained with saturation (Figure 3.6A). The regions of the grey and white matter within the ROI

defining the spinal cord were then outlined on MT-weighted images (Figure 3.6B). The ROIs outlining the grey and white matter were then superimposed onto MTR maps, which were calculated as

$$\text{MTR} = \frac{S_0 - S_s}{S_0} \times 100\%$$

where  $S_0$  = the signal intensities without saturation and  $S_s$  = the signal intensities with saturation.

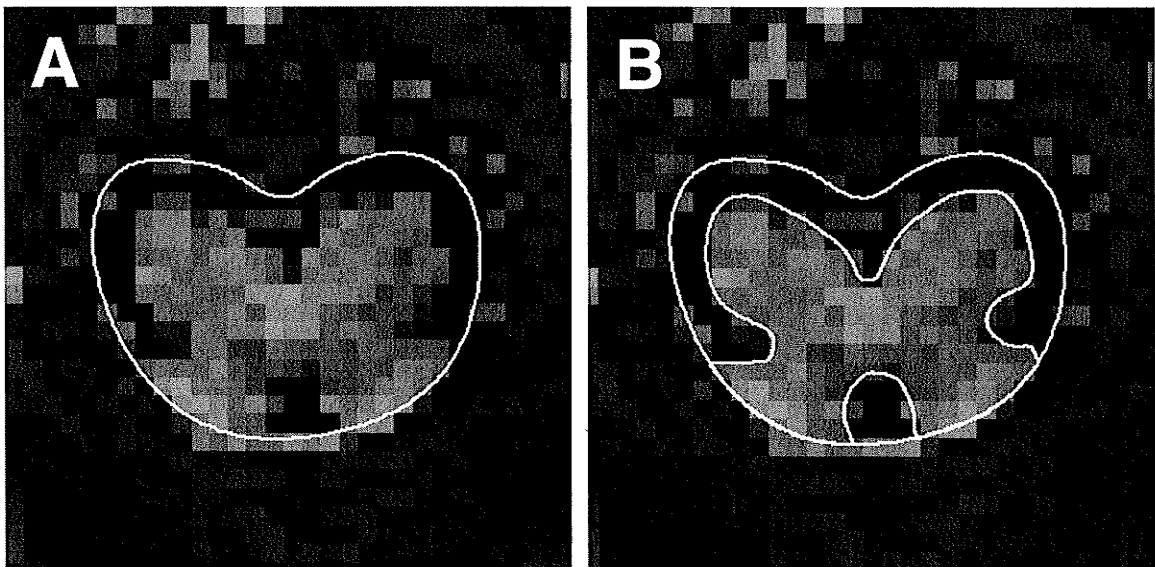


**Figure 3.6.** (A) A ROI determined from a  $T_2$ -weighted image superimposed onto the corresponding MT-weighted image obtained with saturation. (B) ROIs outlining the boundary between the grey and white matter were determined from the MT-weighted image.

## **CHAPTER IV**

### **PRELIMINARY MAGNETIC RESONANCE IMAGING STUDIES**

## **4.1 MRI OF THE CENTRAL NERVOUS SYSTEM IN MOG-INDUCED EAE**

During preliminary T<sub>1</sub>-weighted contrast-enhanced imaging of mice induced with EAE, images of the brain were obtained in order to determine the extent of BBB disruption. In this pilot study, EAE was induced in 9 female mice 11 weeks old as described in chapter 3. Pre- and post- contrast-enhanced T<sub>1</sub>-weighted MR images of the brain and spinal cord were acquired before signs of disease appeared (n=3), at the initial onset of signs (n=6), and again at peak disease for one mouse that had a previous imaging session at the initial stages of EAE. Each mouse underwent an imaging session examining the spinal cord and an imaging session examining the brain on the same day with a delay of a few hours in between imaging sessions to allow the Gd-DTPA to clear from the tissue. A single set of T<sub>1</sub>-weighted contrast-enhanced MR images of the spinal cord was first obtained using a quadrature surface coil as described in chapter 3. After a few hours to allow Gd-DTPA contrast agent to clear from the tissue, MR images of the brain were obtained using a quadrature volume coil as described in chapter 3. This allowed a comparison between the relative contrast enhancement found on MR images of the brain and MR images of the spinal cord in this model of EAE.

In general, comparison of MR images of the brain obtained before the onset of disease signs (Figure 4.1A) with images at the onset of disease signs in mice with EAE (Figure 4.1B) showed no areas of contrast enhancement. The only areas of contrast enhancement observed on all MR images of the brain are within the ventricles. Only in

one mouse were focal areas of contrast enhancement observed within the brain at the early stage of disease (Figure 4.1C). This mouse was re-examined at peak disease and the areas of enhancement were no longer present within the brain (Figure 4.1D). This suggests a rare and transient presence of enhancing brain lesions in this mouse model of EAE. Corresponding images of the spinal cord showed significant contrast enhancement at early stages of disease. Therefore, the spinal cord was felt to be a better target for studies using T<sub>1</sub>-weighted contrast-enhanced MRI in this mouse model, and further MR studies only examined the spinal cord.

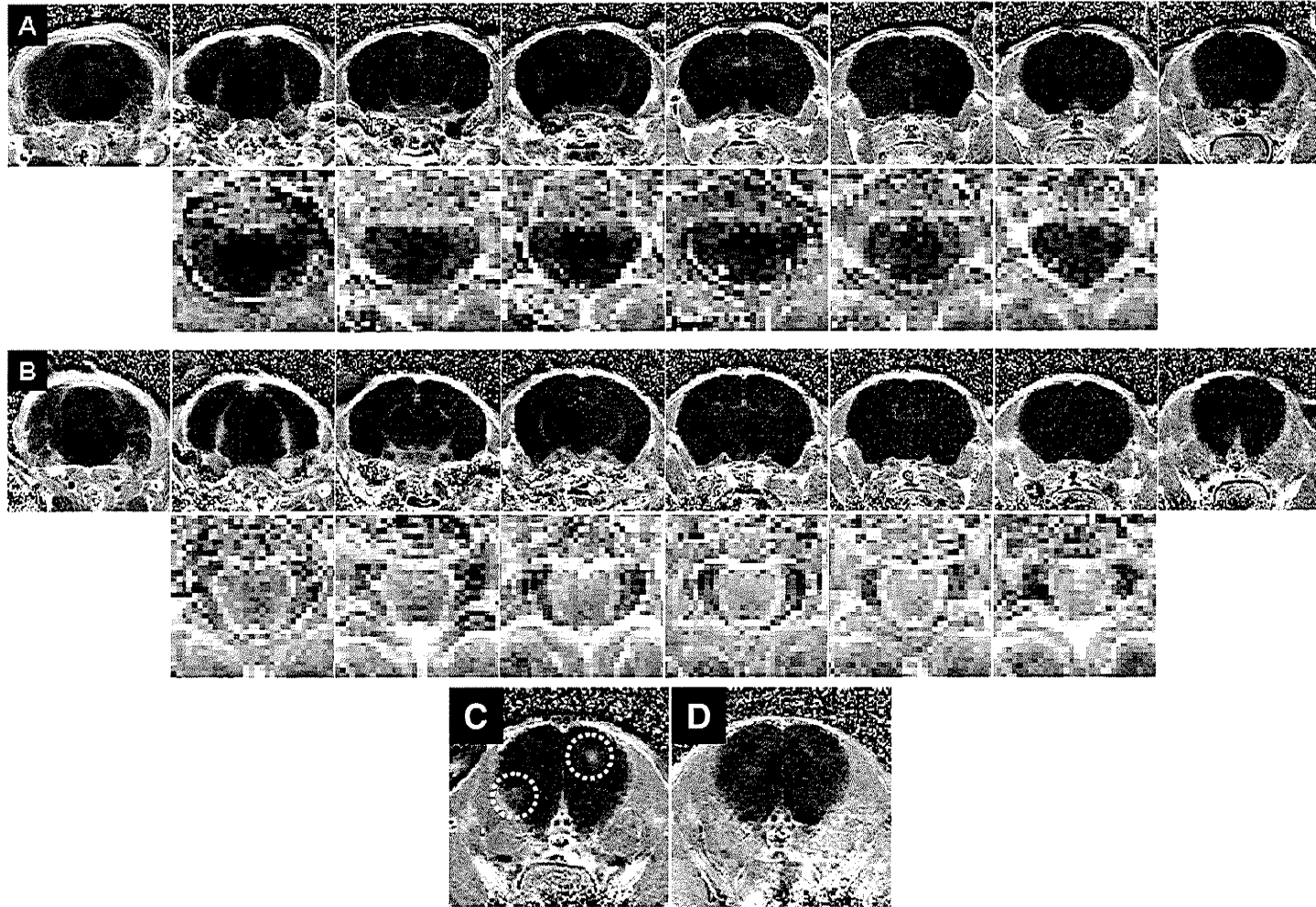


**Figure 4.1.** Representative T<sub>1</sub>-weighted contrast-enhanced difference images of the brain (12mm×12mm) and corresponding images of the spinal cord (3mm×3mm) from a mouse (A) before disease signs and (B) at the first indication of disease signs. One mouse showed focal areas of enhancement (C) at onset of signs, which resolved (D) at peak disease.

## 4.2 KINETICS OF CONTRAST ENHANCEMENT IN THE SPINAL CORD

During preliminary imaging of the lumbar spinal cord in mice with EAE, one mouse was examined at the first indication of disease signs with T<sub>2</sub>-weighted MR imaging and pre- and post-contrast-enhanced T<sub>1</sub>-weighted MR imaging using a quadrature surface coil as described in chapter 3. Initial signs of disease is defined as the day on which a loss of weight >1g or a score >0 was first observed. The most typical presentation of disease signs at the onset is a significant drop in weight accompanied by tail weakness/paralysis. A single set of T<sub>1</sub>-weighted images (Figure 3.3C,D) was obtained repeatedly for 60 minutes after Gd-DTPA injection with an acquisition time of 10 minutes for each set of images (Figure 4.2). Percent difference images were calculated and analyzed using the T<sub>2</sub>- and T<sub>1</sub>-weighted images acquired as described in chapter 3.

The greatest enhancement within the spinal cord was found to be on MR images acquired 10 – 20 minutes after Gd-DTPA injection (Figure 4.3A,B). However, the contrast enhancement within the spinal cord had become more diffuse at this time and therefore the location of greatest BSB permeability can be better visualized at 0 – 10 minutes post-Gd-DTPA administration. A ring of pixels of highest intensity was visible at the periphery of the spinal cord in contrast-enhanced images acquired at 0 – 10 minutes with less contrast enhancement in the central region of the spinal cord. During the 10 – 20 minute acquisition interval, the pixels at the outer edge of the spinal

cord had already begun to decrease in intensity with increased contrast enhancement in the centre of the spinal cord as indicated in Figure 4.3A.

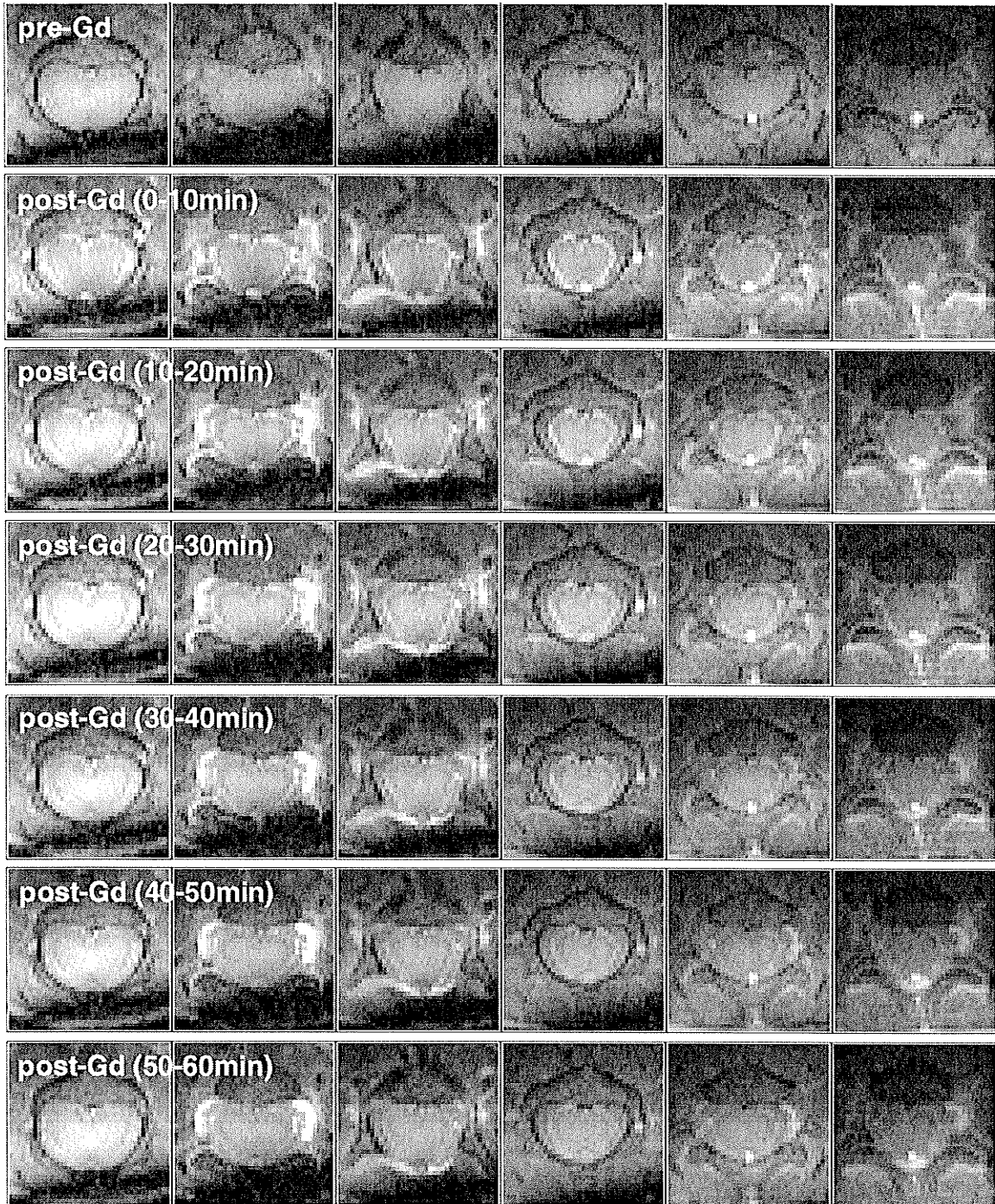


**Figure 4.2.** A complete set of pre- and post-contrast-enhanced  $T_1$ -weighted images (3mm $\times$ 3mm) obtained repeatedly over 60 minutes of the lumbar spinal cord of a mouse with EAE at the beginning of disease signs.

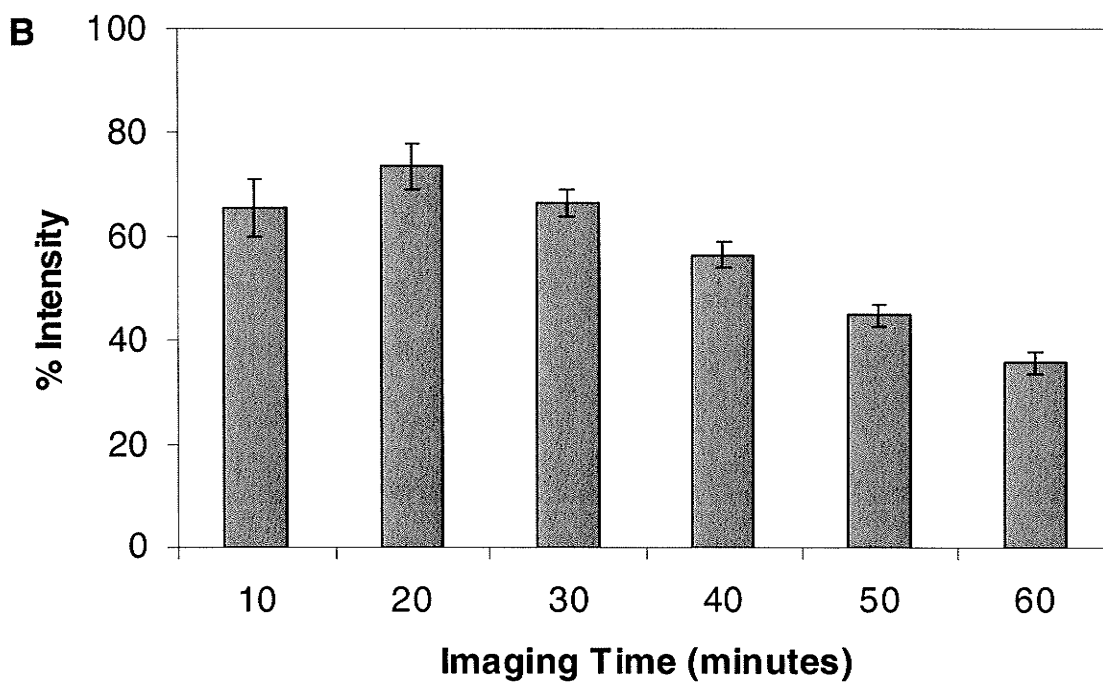
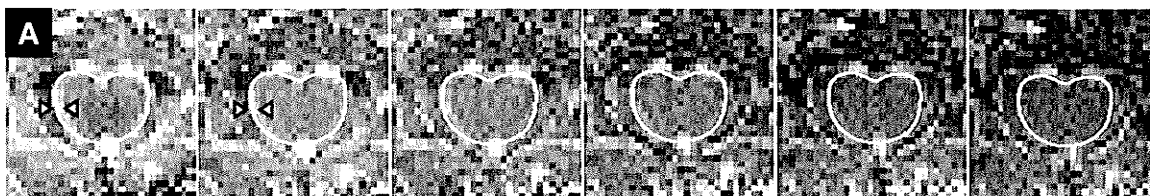


**Figure 4.3.** (A) A representative calculated difference image of contrast enhancement (3mm×3mm) of the lumbar spinal cord of a mouse with EAE acquired at six time points at the onset of disease signs. Images were obtained repeatedly starting immediately after Gd-DTPA administration and every ten minutes later. (B) Average percent intensity ( $\pm$  SEM) across all six slices at each imaging time point of the same mouse as in (A).

### 4.3 DEXTRAN TRACER PILOT STUDY

Tracers such as lanthanum (139D),<sup>80</sup> sodium fluorescein (376D),<sup>73</sup> microperoxidase (1900D),<sup>79</sup> horseradish peroxidase (40kD),<sup>73</sup> Evans Blue (binds to 68kD albumin),<sup>73-75</sup> and fluorescent dextrans (ranging from 3kD to 150kD)<sup>72,73,116-118</sup> have been administered intravenously to visualize vascular permeability in the CNS. Evans Blue and horseradish peroxidase have previously been used as tracers in models of EAE in order to determine the degree of vascular permeability of the BBB and BSB histologically.<sup>38,39,46</sup>

In this pilot study, EAE was induced in a female mouse 11 weeks old and the mouse was weighed and scored daily as described in chapter 3. When the mouse first showed a significant weight loss with tail paralysis, MR images of the lumbar spinal cord were acquired pre- (T<sub>2</sub> and T<sub>1</sub>) and post- (T<sub>1</sub>) contrast enhancement as a single set of slices (Figure 3.3C,D) using a quadrature surface coil as described in chapter 3 (the molecular weight of Gd-DTPA is 550D). Immediately after imaging, Texas Red 3kD dextrans (0.15g/kg, 10mg/mL in PBS, lysine fixable, 1 mole dye/mol dextran; Molecular Probes, Eugene, OR) were injected into the left ventricle of the heart of the mouse followed one minute later by cardiac-fixation using phosphate buffered formalin. The region of the lumbar spinal cord that corresponded to the location of MR slice positions was removed (Figure 4.4) and embedded into paraffin. Sections 6µm thick were dewaxed in xylene to examine for regions of fluorescent dextrans. MR image analysis of contrast-enhanced images was performed as in chapter 3 and showed

there was an average enhancement of 70.2% across all slices at the initial stage of disease.

Patches of red fluorescence were seen surrounding vessels at the periphery of the spinal cord of the mouse at the initial onset of signs of disease (Figure 4.5). This provides some histological evidence of BSB disruption at the beginning of disease signs in EAE. The dextrans were in circulation for only one minute to allow minimal time for diffusion in spinal cord tissue and to provide an indication of the regions of BSB permeability. In the mouse examined, the regions of fluorescence were found in the peripheral white matter of the spinal cord.

The gadolinium contrast agent had a longer circulation time of 10 minutes post injection (the acquisition time of the contrast-enhanced T<sub>1</sub>-weighted images) compared to the circulation time of one minute for the dextran tracers. The smaller molecular size of Gd-DTPA (550D) relative to the dextrans (3kD) along with differing chemical properties and the difference in circulation time are variables that may affect the diffusion of these tracers across the BSB. These differences do not allow a direct spatial comparison to be made between contrast enhancement and histological fluorescence of dextrans; however, the MR contrast agent and the dextran tracers both confirm the presence of increased BSB permeability at the periphery of the spinal cord.

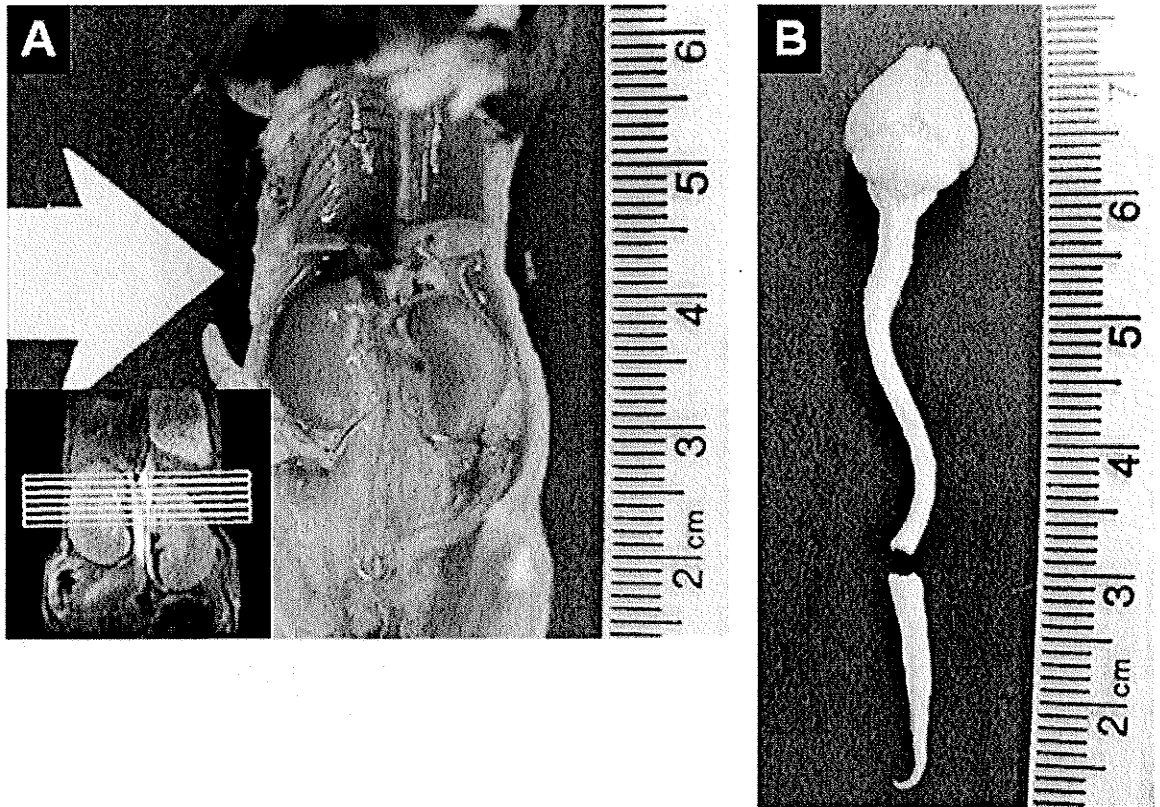


**Figure 4.4.** (A) The anatomical location that corresponds to the imaged region is within the region of the kidneys. The arrow indicates where the imaged region began at the rostral end the kidneys. (B) The spinal cord was removed and cut at the point where imaging began and this lumbar segment of the cord was embedded into paraffin.

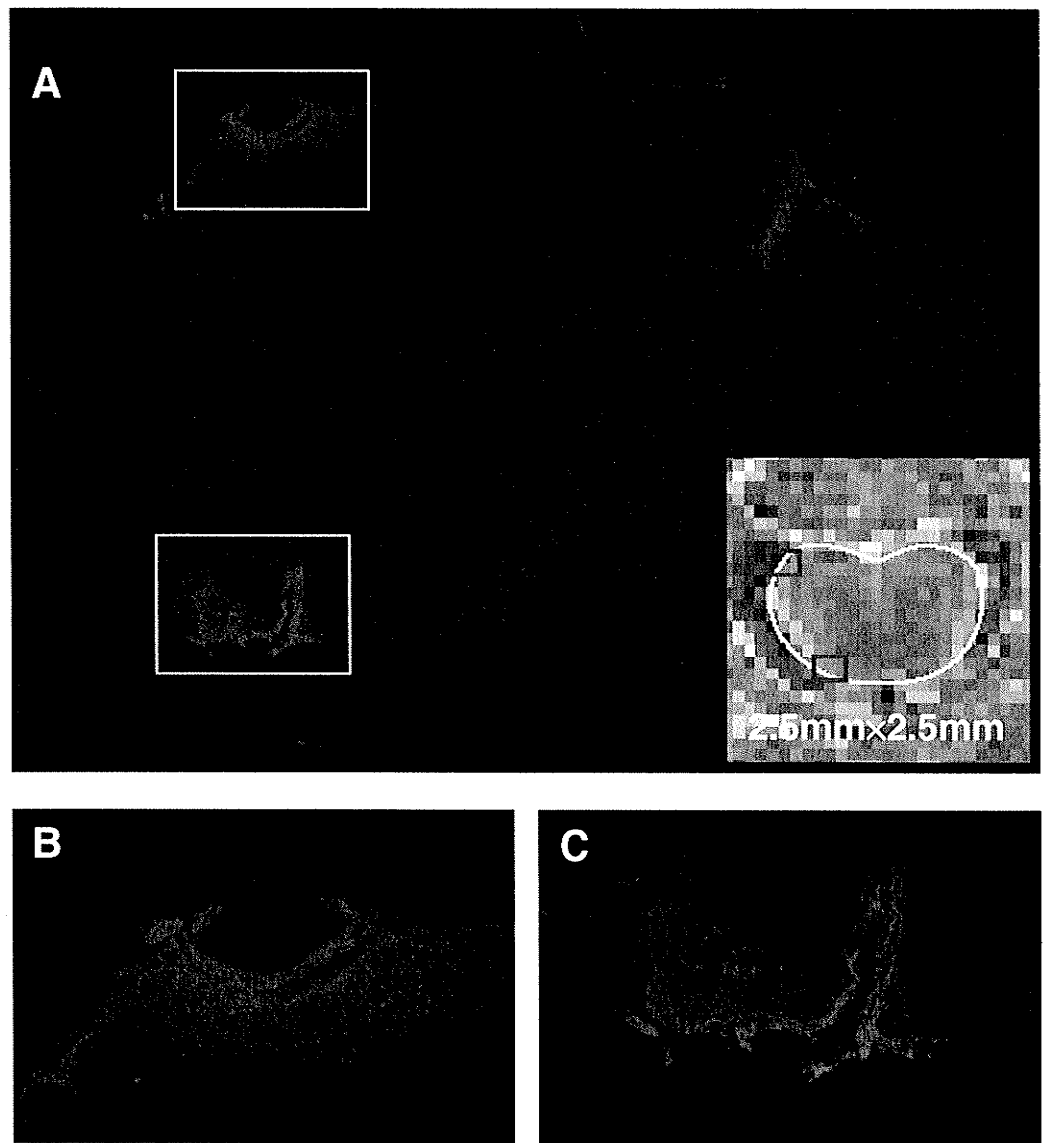


**Figure 4.5.** (A) A histological cross section of the spinal cord of a mouse with EAE at the onset of disease signs following intravenous dextran administration with corresponding calculated difference image of contrast enhancement obtained immediately prior to sacrifice. (B) and (C) show the regions where dextrans have leaked from vessels into spinal cord tissue as outlined on the histological section and calculated image in (A).

## **CHAPTER V**

# **MAGNETIC RESONANCE IMAGING OF BLOOD-SPINAL CORD BARRIER DISRUPTION IN MICE WITH EXPERIMENTAL AUTOIMMUNE ENCEPHALOMYELITIS**

## 5.1 INTRODUCTION

The breakdown of the BBB or BSB may be an important event during the initial stages of EAE. Increased leakage across the BBB may be due to an increase in vesicular transport<sup>46,77,92,119</sup> or the loosening of tight junctions between endothelial cells.<sup>120</sup> There are conflicting reports regarding BBB disruption as a consistent component in the development of EAE and in the sequence of events leading to the development of signs of disease. Some studies have indicated that vascular permeability is a distinct event that precedes cellular infiltration,<sup>41,45,121</sup> while other studies found BBB permeability to be present only during inflammation.<sup>44,48,54,91,92</sup> Though these observations may be dependent on the specific model of EAE, the role of BBB permeability in the initial development and during the progression of the disease is unclear. This question of whether vascular permeability precedes inflammation is important to the understanding of lesion development, and may provide insights into the course of the disease in humans with MS.

The MR contrast agent Gd-DTPA is commonly used to visualize regions of BBB or BSB disruption using MR imaging. An intact BBB and BSB prevents the movement of contrast agent from the blood into the tissue of the CNS. A disrupted or “leaky” BBB on the other hand permits the movement of contrast agent from the blood into the CNS. The resulting increase in proton relaxation rate and in the intensity of T<sub>1</sub>-weighted MR images then shows regions where the BBB is disrupted, and the degree of contrast enhancement gives a measure of the relative BBB disruption at the time of the MR examination. Clinically, lesions in the CNS of MS patients showing such contrast

enhancement on MR images are often identified as active lesions, and in many cases these lesions are found to correlate with clinical symptoms.<sup>87,94,96</sup> Enhancing lesions on T<sub>1</sub>-weighted MR images are often visualized before they can be detected on conventional T<sub>2</sub>-weighted MR images in both MS<sup>95,97</sup> and EAE.<sup>92</sup> A serial imaging study of MS patients showed that all new lesions exhibited Gd-DTPA enhancement, although not all of these were associated with clinical signs or symptoms.<sup>94</sup>

Studies using genetically altered mice are providing new and important information about many disorders of the CNS, including EAE and MS<sup>122,123</sup> and it is important to have methods to follow disease progression *in vivo* in such mice. In mouse, EAE often affects the spinal cord, and in particular the lumbar cord, rather than the brain. MR methods have been used to document BBB disruption in EAE in rat brain<sup>51,54,56,59,121,124</sup> and BSB disruption in the guinea pig spinal cord.<sup>91-93,119</sup> In mouse, BSB disruption has been investigated using histological methods<sup>36,55</sup> but not *in vivo*. The purpose of this study was to evaluate the utility of MRI in detecting lesions and BSB disruption *in vivo* during EAE in the mouse lumbar spinal cord, to determine how MR features of BSB disruption change during the course of disease, and to investigate the correspondence of such changes with clinical signs and histological features of disease.

## 5.2 MATERIALS AND METHODS

### 5.2.1 Induction of EAE and Scoring System

EAE was induced in 21 female C57BL/6 mice (Charles River Canada, Saint Constant, Québec) between 8 and 11 weeks old. Control animals received either saline alone (n=2) or the same preparations used for EAE induction but without MOG<sub>35-55</sub> (n=3). Each mouse was weighed and scored daily as described in chapter 3.

### 5.2.2 MR Imaging

Two sets of interleaved T<sub>2</sub>-weighted images of the lumbar spinal cord were obtained during each imaging session followed by identically positioned T<sub>1</sub>-weighted images using a quadrature surface coil as described in chapter 3 with slice positioning shown in Figure 3.3A,B.

There were 28 imaging sessions for the 21 inoculated mice, with each mouse examined at least once. Mice were examined with MR imaging before signs of disease appeared (n=3), at the onset of disease signs (taken to be the day on which a disease score > 0 or a loss of weight >1g was first observed; n=7), at peak disease (taken to be the day on which weight loss ceased, shown in pilot experiments to occur within  $\pm 1$  day of peak disease score; n=5), or at remission (when the disease score did not decrease for 3 consecutive days; n=10). Three of the mice examined at the onset of signs and one mouse examined at peak disease were also examined during remission; the remaining 4 mice examined at onset of disease and 4 mice examined at peak disease were killed for histology immediately following MRI. The three mice examined before the appearance

of signs of disease were also examined with MRI during remission. All 10 mice examined at remission were killed for histology after MRI. Three mice did not develop disease signs (classified as subclinical EAE), and each was examined with MR imaging once, one on day 19 and two on day 25 post-inoculation, and then killed for histology. Five control (non-inoculated) mice were also examined with the same MR imaging protocol. The inoculated mice were not assigned to experimental groups before the first signs of disease became apparent, but were randomly selected as disease developed in order to satisfy the objective of establishing the utility of MR and demonstrating the correspondence between histology and image features.

### *5.2.3 MR Image Analysis*

The contrast enhancement within the spinal cord following Gd-DTPA was quantified as described in chapter 3. Histograms of pixel intensity within the ROIs were generated in order to determine the distribution of pixel intensities and as an aid in selecting the region of the spinal cord where the pixels of greatest intensity were located within each experimental group.

### *5.2.4 Tissue Processing and Scoring of Inflammation*

Mice were killed by perfusion-fixation through the heart using phosphate buffered formalin for histological examination after MR imaging at the onset of disease (n=4), at peak disease (n=4), at remission (n=10), or at subclinical EAE (n=3). Because one of the goals of the study was to obtain accurate correlations between imaging and histological features, identifiable anatomic landmarks external to the spinal cord were

required. The body was thus dissected to leave the kidneys and retroperitoneal tissue attached to the spinal column with the spinal cord *in situ* (Figure 5.1A). This tissue block was decalcified in 10% formic acid for 48 hours, with the solution replaced after 24 hours. When the bony tissues were soft, the tissue block was cut in cross sections into three smaller blocks corresponding to the kidney anatomy that was visible on the MR images (Figure 5.1B).

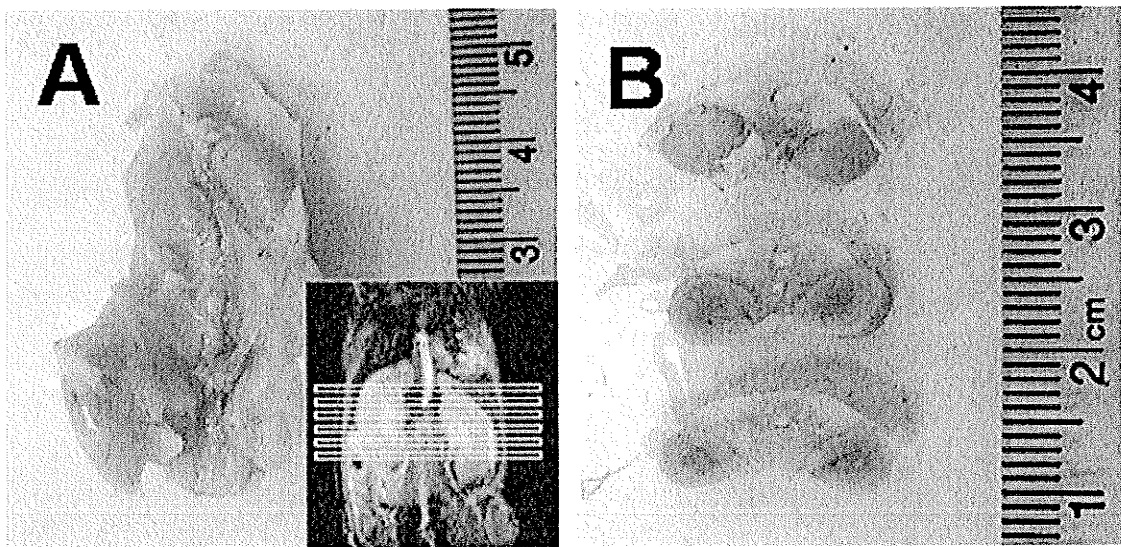


**Figure 5.1.** (A) The spinal cord was kept *in situ* to allow anatomical correlations to MR images (inset) with respect to the kidneys. (B) Tissue was cut into blocks prior to paraffin embedding.

The blocks of tissue were then dehydrated and embedded in paraffin wax. Tissue sections 6  $\mu\text{m}$  thick were cut, stained with hematoxylin & eosin (H&E), and examined for general features of inflammation. Only one tissue section was obtained from each animal for each staining method; however, each tissue section that was cut contained a cross section from three levels of the spinal cord. Sections stained with biotin-

conjugated anti-mouse IgG (1:50; Jackson ImmunoResearch Laboratories, West Grove, PA) followed by incubation in diaminobenzidine (DAB) were used to identify regions of plasma leakage through disrupted BSB. IgG labeling within the kidney served as a positive control. Activated microglia/macrophages were detected using biotin-conjugated Griffonia simplicifolia 1 (GS) lectin (1:100; Sigma-Aldrich, Saint Louis, MO) and visualized using DAB. Lectin labeling in bone marrow cells and endothelial cells of blood vessels served as a positive control. Sections were stained for myelin using solochrome cyanine, differentiating in 10% iron alum and counterstaining with eosin Y.

Tissue sections stained with H&E and with lectin were scored for inflammation.<sup>114</sup> A score of 0 represented no inflammatory cells, 1 indicated small foci of subarachnoid infiltration, 2 represented widespread subarachnoid infiltration, 3 represented foci of inflammatory cells within the periphery of the spinal cord, and 4 represented a more diffuse pattern of inflammatory cells within the spinal cord. In sections stained for myelin, a score of 0 indicated normal staining of myelin within nerve roots and a complete ring of staining within the periphery of the spinal cord, 1 corresponded to rare foci of reduced staining, 2 indicated prominent multifocal or peripheral ring loss of myelin staining, and 3 represented complete loss of myelin staining.

### *5.2.5 Statistical Analysis*

Data from each group of animals are reported as mean  $\pm$  standard error of the mean (SEM). Parametric data (percent enhancement) were compared statistically using

analysis of variance (ANOVA) followed by Bonferroni/Dunn post hoc test, whereas the Kruskal-Wallis test followed by post hoc unpaired t tests were used for non-parametric data (histological scores). Statistical significance was considered to be at  $p < 0.05$ .

### 5.3 RESULTS

Three of the 21 inoculated mice did not develop any signs of disease, while the other mice began to show signs of disease on day 8-14 post-inoculation (Figure 5.2). Typically a drop in weight of 1g or more was accompanied by tail weakness as the first sign of disease. Animals exhibited peak disease score 2-8 days after disease onset or 10-18 days post inoculation, usually with complete hindlimb paralysis and occasional forelimb weakness. At remission the mice had regained substantial use of all limbs. Only one animal showed a modest subsequent increase in disease score before being killed for histology. This disease progression is similar to that seen in other studies using this animal model.<sup>111,112,114</sup>

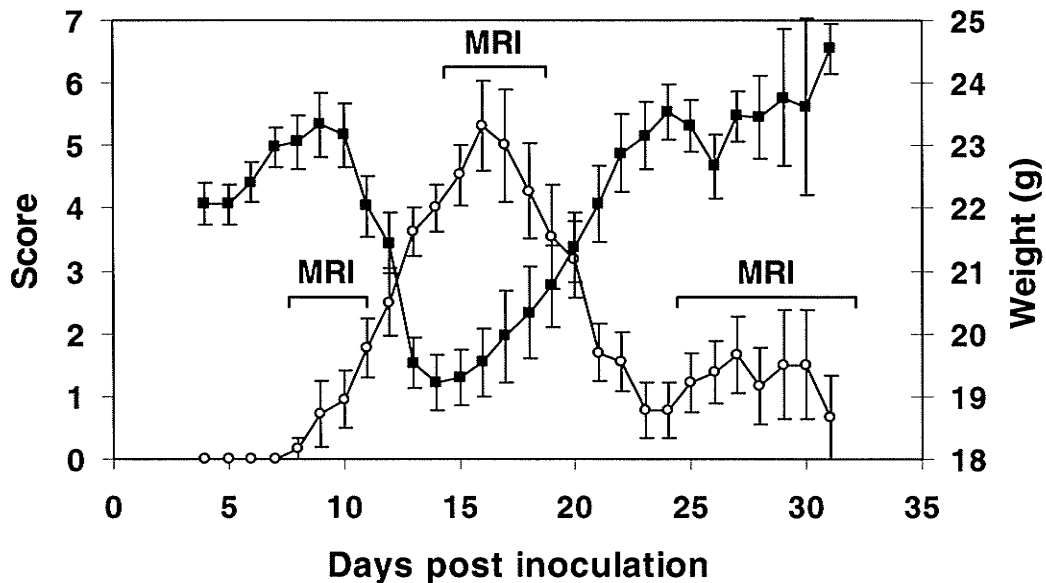


**Figure 5.2.** Average scores of disease severity (o) and body weight (■) in mice during the progression of EAE. Times of MR imaging sessions at the first appearance of disease, at peak disease, and during disease remission are indicated. Error bars represent SEM.

The animals that exhibited signs of disease were imaged within 24 hours of onset, at peak disease, or when in remission, as indicated on Figure 5.2. No focal lesions were evident on T<sub>2</sub>-weighted MR images obtained at any stage of disease, although the lumbar spinal cord was clearly distinguished from nearby nerve roots and surrounding CSF on T<sub>2</sub>-weighted images (previously shown in Figure 3.4). No contrast enhancement was seen in MR images of the spinal cord obtained before the onset of signs of disease in affected mice, in control mice, or in inoculated mice that did not develop signs of disease. Contrast enhancement was clearly seen in the lumbar spinal cord in mice exhibiting signs of disease (Figures 5.3, 5.4). This enhancement took the form of a pronounced ring at the periphery of the cord, with lower enhancement extending throughout the cord. The contrast enhancement within the cord tended to be greater in peripheral regions, suggesting greater BSB disruption in white matter than in the grey matter of the cord. In this study, even in highly T<sub>2</sub>-weighted MR images grey matter was not distinguished from white matter at the level of the lumbar spinal cord, although they were clearly distinguished at more anterior levels. It was therefore not possible to evaluate contrast enhancement quantitatively in lumbar cord white and grey matter separately. Across the entire lumbar spinal cord, however, at the onset of disease signs, the average contrast-induced intensity increase for the 6 slices examined was 60% (Figure 5.4). The contrast enhancement was significantly lower at peak disease, about half that seen at the onset of disease signs (Figure 5.4), and the increased enhancement at the periphery of the cord and in the white matter was less evident (Figure 5.3). Animals in remission showed little enhancement within the spinal cord.

There was no difference between mice examined by MRI only at disease remission, and those examined both at an earlier stage of disease and again at remission.

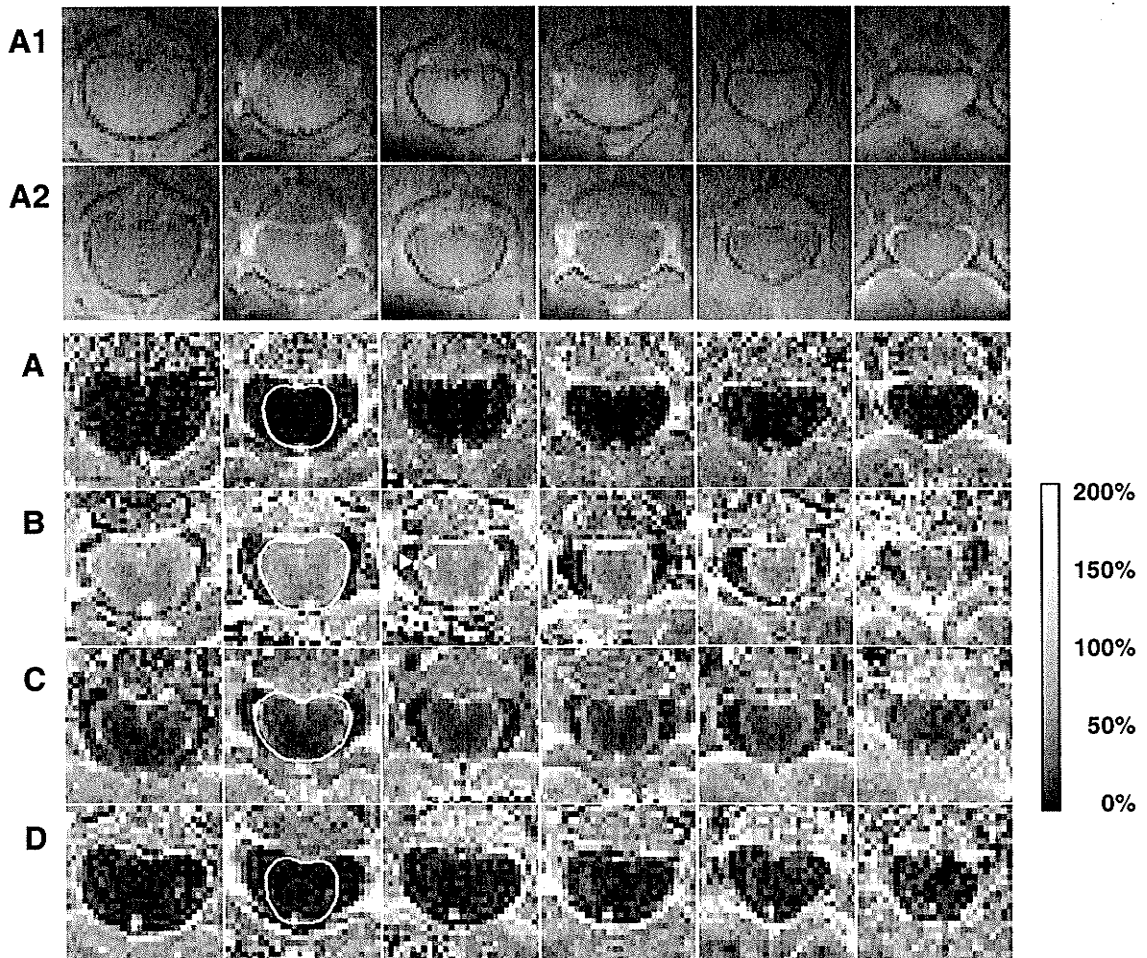


**Figure 5.3.** Representative sets of calculated contrast-enhanced images (A to D), obtained from the MR data acquired over the interval 0-10 minutes after contrast administration, shown as maps of % intensity increase for (A) a healthy mouse, (B) a mouse at the initial stages of disease, (C) a mouse at the peak of disease, and (D) a mouse in remission. The ROI defining the spinal cord is shown for one image of each set. In (B), arrows point out the ring of high contrast enhancement at the cord surface in one of the images. The sets of pre- and post-contrast-enhanced T<sub>1</sub>-weighted images (A1 and A2 respectively) that were used to calculate the images from the healthy mouse in (A) are also shown.

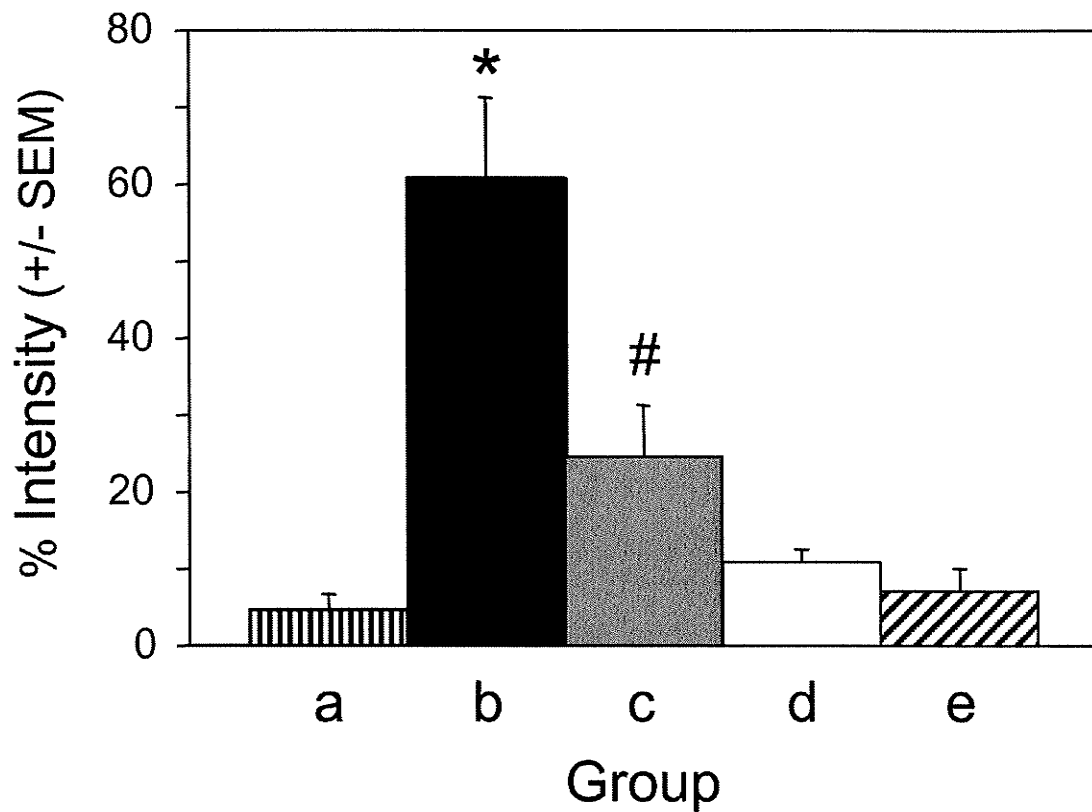


**Figure 5.4.** The average  $\pm$  SEM across the 6 slices examined in this study for the % intensity change in T<sub>1</sub>-weighted MR images of the lumbar spinal cord following Gd-DTPA administration in a) control mice (n = 5), b) mice showing initial signs of EAE (n = 7), c) mice at peak disease (n = 5), d) mice in remission (n = 10), and e) mice with subclinical EAE (n = 3). \* differs from all other groups (p < 0.001) # differs from control (p < 0.05).

Histograms of pixel intensity in the contrast-enhanced MR images of the spinal cord (Figure 5.5) showed a symmetrical distribution about zero for control animals and animals in which disease was in remission. In the case of animals showing signs of disease, the intensity distribution was distinctly asymmetrical with values tailing off to higher intensities, and the peak intensity was significantly shifted away from zero. By selecting only the upper 50% of total pixels, the location of the pixels of greatest intensity was clearly shown to be in the peripheral white matter of the spinal cord (Figures 5.5). No focal lesions showing contrast enhancement were identified in any mice at any stage of disease. No enhancement was seen in the nerve roots at any stage of the disease.

Features of inflammation were characterized on histological sections stained with H&E and with lectin staining. Inflammatory cells were not present in the spinal cords or nerve roots of control mice (Figure 5.6). The nerve roots and periphery of the cord stained blue with solochrome cyanine, indicating the presence of myelin. Mice sacrificed at the initial stage of disease exhibited foci of dense inflammatory cell infiltrates at the periphery of the cord in regions surrounding vessels on both H&E and lectin stained slides (Figure 5.6). The aggregated cells were small and round, morphologically consistent with lymphocytes. At peak disease inflammatory cells were also evident as dispersed infiltrates in the spinal cord (Figure 5.6). Prominent areas of decreased myelin staining were observed at disease onset and at peak disease, whereas a mild diffuse decrease in staining was observed at remission. The amount of inflammation present at remission was significantly reduced and quite variable. A few lectin-positive cells were found scattered in some nerve roots in seven of the ten mice

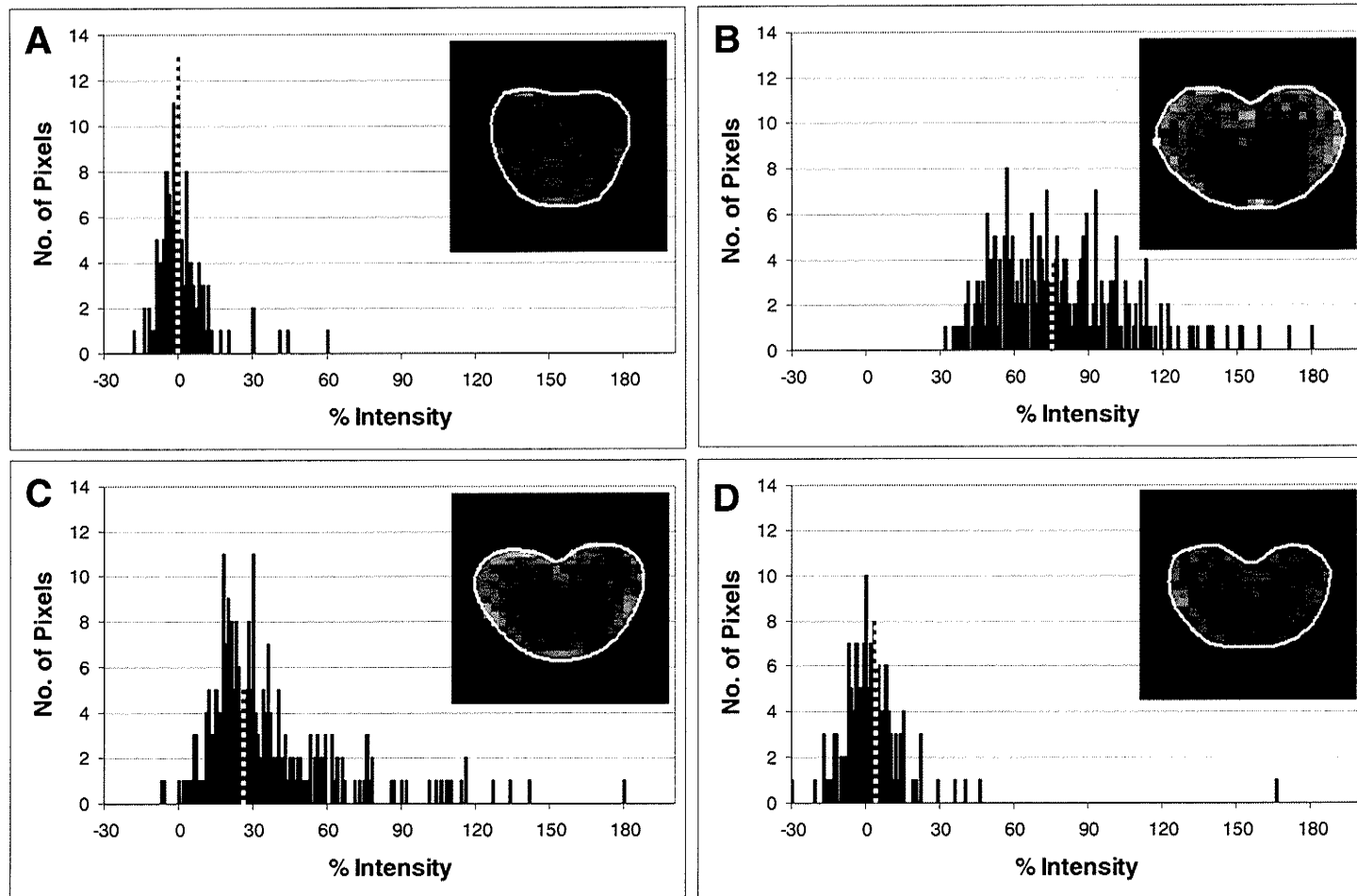


**Figure 5.5.** Representative histograms from a mouse at (A) control, (B) initial onset, (C) peak disease and (D) remission of the pixel intensities within the lumbar spinal cord. Corresponding difference images show the location of the 50% greatest enhancing pixels from each histogram respectively.

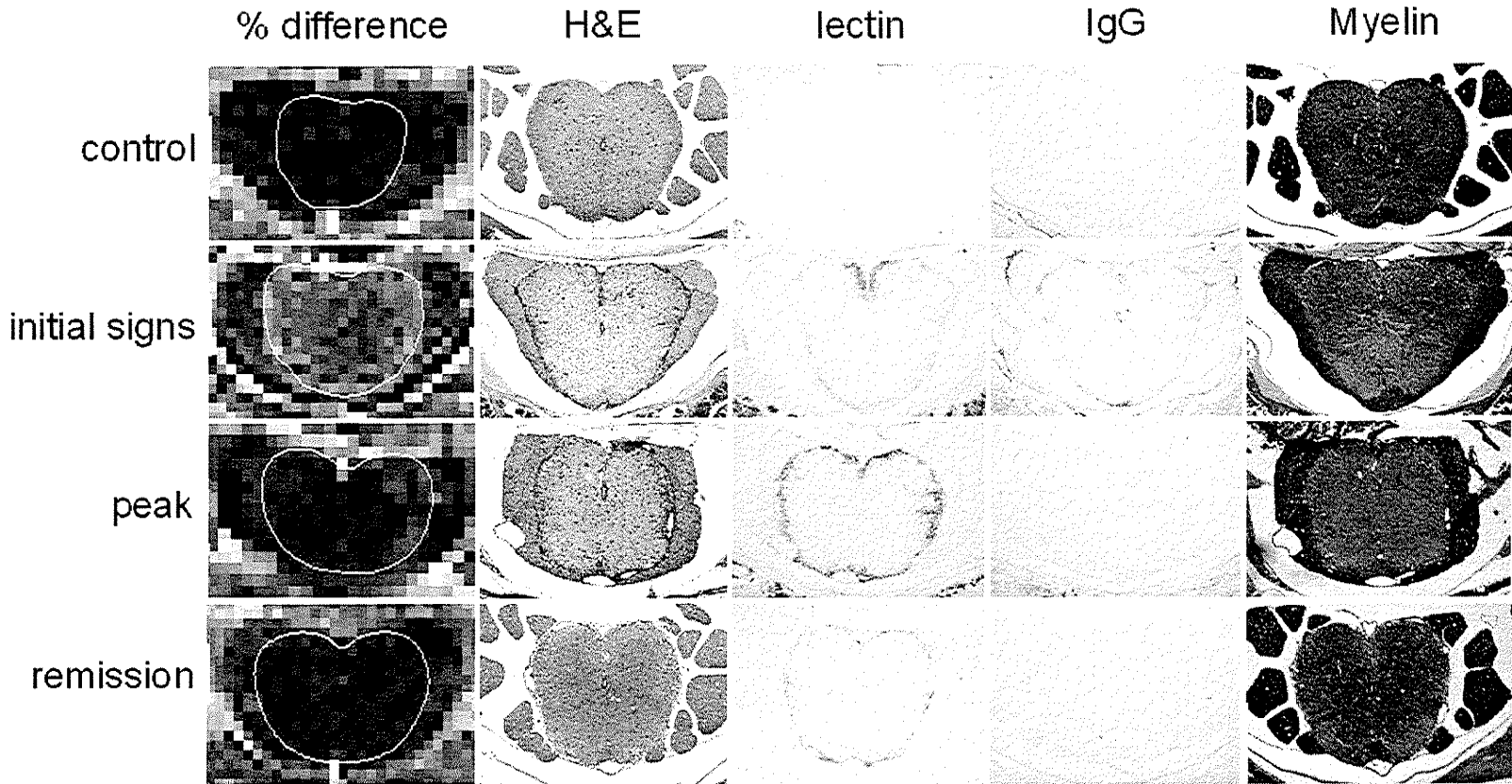


**Figure 5.6.** Histological sections stained with H&E (for general features of inflammation), lectin (activated microglia and macrophages), IgG (BSB leakage), and solochrome cyanine (myelin) for representative control mouse, a mouse showing first signs of disease, a mouse at peak disease, and a mouse in remission. The corresponding contrast enhancement maps of the spinal cords are shown for each case.

killed at remission. Histological scores representing the degree of cellular infiltration apparent on sections stained with H&E and lectin are summarized in Figure 5.7. The scores at the onset of disease signs and at peak disease each differ significantly from the scores both at remission and for subclinical EAE.

Weak labeling of IgG was found in a wedge-like peripheral distribution in three of the four mice examined at the initial stages of EAE. These areas corresponded to regions of dense inflammatory cell infiltrates (Figure 5.6). No positive staining for IgG was observed in spinal cord tissue of mice killed at peak disease or in remission, although spinal cords of animals killed at peak disease appeared to have more vacuolated white matter, suggesting an edematous state.

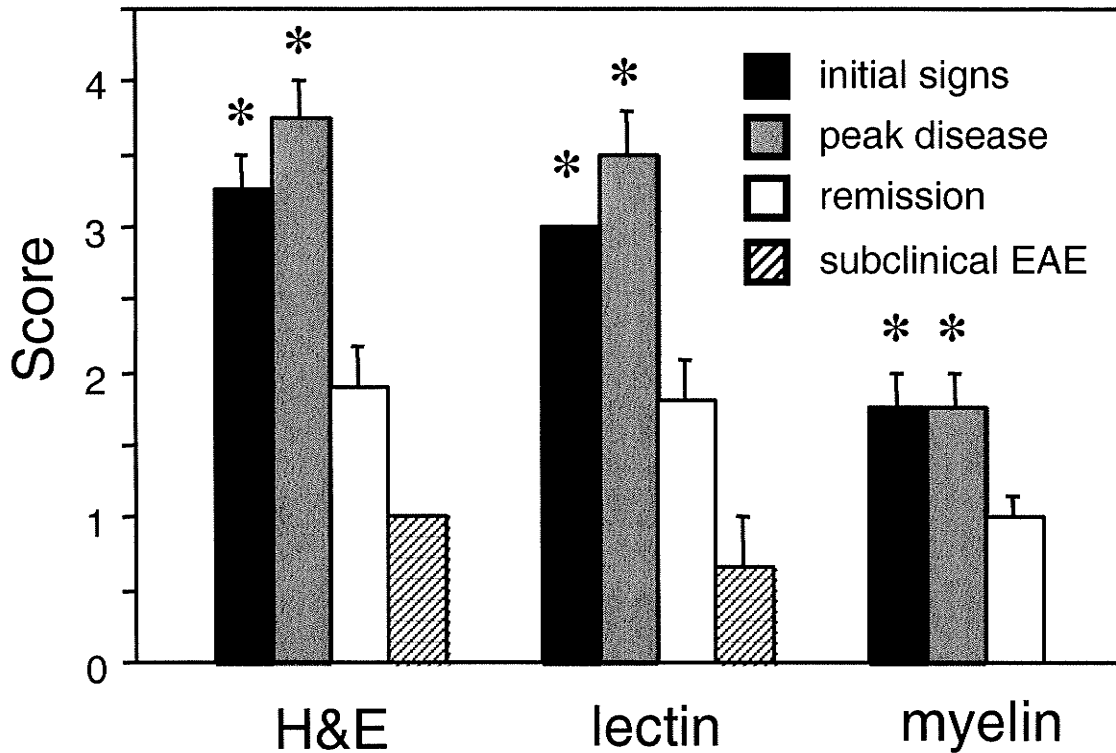


**Figure 5.7.** Histological scores ( $\pm$  SEM) for H&E (for general features of inflammation), lectin (activated microglia and macrophages), and solochrome cyanin (myelin) for mice at the different stages of disease. Scores for control mice were 0 in each case. In each case the score at the initial signs of disease ( $n=4$ ) differs from that at remission ( $n=10$ ;  $p<0.05$ ) and for subclinical EAE ( $n=3$ ;  $p<0.01$ ), the score at peak disease ( $n=4$ ) differs from that at remission ( $p<0.01$  for H&E and lectin and  $p<0.05$  for myelin) and for subclinical EAE ( $p<0.01$ ).

## 5.4 DISCUSSION

In this study, the use of a stable tail vein catheter allowed the intravenous administration of a MR contrast agent (Gd-DTPA) while avoiding repositioning of the experimental animals. The same amount of contrast agent was administered to each mouse, and T<sub>1</sub>-weighted images were acquired with the same pulse sequence and at the same time after administration of contrast agent in each MR examination. This then made it possible to generate precisely corresponding sets of pre- and post-contrast images, and allowed the calculation of reliable values for the contrast enhancement, expressed here as % difference in the intensity in T<sub>1</sub>-weighted MR images obtained before and after administration of the contrast agent. Since the change in relaxation rate and hence the contrast enhancement is proportional to the contrast agent concentration in tissue, the relative contrast enhancement gives a relative measure of the BSB permeability within the mouse lumbar spinal cord during the progression of EAE.

The first sign of disease in this model of EAE occurred 8-14 days after the first MOG inoculation as a drop in weight of the experimental animals. In most animals this was accompanied by tail weakness, although since the animals were observed for signs of disease only once per day it is possible that with more frequent monitoring a drop in weight would have been found to precede functional impairment in these animals as well. Contrast enhancement in the MR images, and hence BSB disruption, was maximum at this first stage of disease, and decreased progressively when the disease signs reached their peak and subsequently resolved. In mice examined before the onset

of signs of disease, or in inoculated mice that did not show signs of disease, no contrast enhancement was evident in the MR images, indicating that the BSB was intact in these animals. It was not possible to obtain contrast-enhanced MR images immediately prior to the appearance of disease signs to determine if contrast enhancement and BSB disruption precedes the onset of disease because daily (or more frequent) MR imaging post-inoculation would be required. This is impractical and it is possible that repeated anesthesia could alter the disease progression. However, MR images obtained in some mice as little as two days before the appearance of clinical disease signs showed no contrast enhancement. The results of the histological staining for IgG are consistent with pronounced BSB disruption in the early stages of disease. Traces of IgG were observed surrounding peripheral vessels only at these early stages of EAE, indicating that the breakdown of the BSB is then severe enough to allow the relatively large IgG molecules ( $M = 150\text{kD}$ ) to extravasate. At the maximum disease stage and in mice in remission no IgG staining was evident in the histological sections, consistent with the BSB being less severely disrupted at these times. Since contrast enhancement was clearly evident in the MR images taken at the time when disease symptoms were maximum, the BSB must be sufficiently disrupted to allow movement of contrast agent into the spinal cord tissue at this stage of disease. Since no histological evidence of BSB disruption was apparent in mice killed immediately after MRI at this stage of disease, the use of contrast-enhanced MRI to detect BSB disruption appears to be more sensitive than histological measures which detect relatively large blood-borne molecules such as IgG.

Disruption of the BBB and BSB in the early stages of disease, as observed in this study, is a feature common to other EAE models, although the subsequent time course of the disruption may vary with the model. In the Lewis rat contrast enhancement in the CNS and immunohistochemical staining for fibrinogen corresponding to BBB and BSB disruption are coincident with the onset of disease signs.<sup>121</sup> While no subsequent decrease in enhancement was observed during remission in one study using this model,<sup>121</sup> in another study a significant decrease in contrast enhancement between the acute and remission stages of disease was observed.<sup>59</sup> Histological studies showed that in the rat lumbar spinal cord BSB disruption precedes clinical signs of disease by about 1 day, although the disruption is sufficient to allow permeability to only small molecules and not to blood-borne proteins.<sup>41</sup> Similarly, in the guinea pig, contrast enhancement in the spinal cord is seen before the onset of disease signs<sup>91,92</sup> as well as during disease.<sup>47,93</sup> Early breakdown of the BSB or BBB appears to be a good indicator of subsequent disease development.

Both in the early stages of disease and at peak disease, contrast enhancement occurred throughout the spinal cord at the level examined in this study. No focal regions of enhancement were apparent at the spatial resolution obtained in this study (98 $\mu$ m $\times$ 98 $\mu$ m $\times$ 750 $\mu$ m). A histogram analysis of the enhancement within the spinal cord, represented as a percent increase in intensity, identified an asymmetrical distribution of pixel intensity. By isolating the pixels with greatest enhancement it was observed that the enhancement was clearly more pronounced in the outer regions of the spinal cord at both stages of disease, and in addition a distinct ring of tissue with high contrast was evident at the periphery of the cord. This suggests that the BSB

breakdown occurred predominantly in the white matter or on the surface of the spinal cord. Subsequent diffusion of the contrast agent during the post-contrast imaging procedure may have contributed to the appearance of enhancement throughout the cord, including in the grey matter where no inflammatory infiltrate was evident. Indeed, a pilot experiment previously described in chapter 4 showed that post-contrast images obtained over the following 10 minute interval (ie acquired over the interval 10-20 minutes after contrast administration) showed more uniform enhancement across the spinal cord.

At the time the first signs of disease became apparent in this study, histological assessment of spinal cord tissue showed foci of inflammatory cells surrounding vessels at the periphery of the spinal cord. Spatially, these features corresponded to the regions of contrast enhancement, and hence BSB disruption, seen on MR images at the periphery of the spinal cord and in the white matter. In EAE in the guinea pig spinal cord, contrast enhancement occurs together with inflammatory infiltrates at a similarly early disease stage,<sup>92</sup> although in the chronic phase of disease the enhancement is lower in regions where demyelination accompanies cellular infiltrates.<sup>93</sup> In the Lewis rat BBB leakage is present only in regions where cellular infiltrates are evident,<sup>54,77</sup> although inflammatory infiltrates are also seen in areas of the brain which do not show contrast enhancement.<sup>56</sup> Other studies, however, have found that the BBB is disrupted prior to the onset of inflammation.<sup>41,45,121</sup> While disruption of the BBB or BSB is not a pre-requisite for CNS inflammation,<sup>125,126</sup> BSB disruption synchronous with, or earlier than, inflammation may indicate that BSB disruption affords an additional mechanism

for inflammatory cells to access the CNS. Further studies are required to examine this, or to test the possibility that CNS inflammation contributes to BBB and BSB damage.

In the present study, prominent regions of myelin loss were observed in the spinal cord at the onset of disease signs and when these signs were at a maximum, and the myelin loss decreased and was more diffuse when the disease signs resolved. The time course of myelin loss during the progression of the disease therefore corresponded quite closely with the time course of inflammatory infiltrates. This differs from EAE in the guinea pig, where myelin loss in the spinal cord is prominent only in the chronic stage of disease.<sup>93</sup> At this disease stage contrast enhancement on MR imaging is lower in demyelinated white matter containing inflammatory infiltrates than in regions containing only cellular infiltrates without demyelination.<sup>93</sup> In mouse spinal cord, on the other hand, the present study found that the contrast enhancement decreased at peak disease, while demyelination and inflammation both remained high. This suggests that ongoing inflammation resulted in progressively increasing tissue injury leading to the observed functional impairment. The decrease in BSB permeability may be an early indication of progression to disease remission in this model, at which time remyelination has occurred and the amount of inflammation has decreased. The almost complete absence of disease signs at remission suggests as well that to a considerable extent the tissue injury was not permanent in this model of a single disease episode.

## **CHAPTER VI**

# **BLOOD-BRAIN BARRIER DISRUPTION IN CCL2 TRANSGENIC MICE DURING PERTUSSIS TOXIN-INDUCED BRAIN INFLAMMATION**

## 6.1 INTRODUCTION

The chemokine CCL2, previously known as monocyte chemoattractant protein (MCP)-1, has a role in the recruitment of inflammatory cells into the CNS.<sup>127,128</sup> CCL2 is expressed within active and chronic MS lesions<sup>128-131</sup> and there are decreased levels in the CSF of MS patients.<sup>128,132,133</sup> Mice lacking CCR2, the receptor for CCL2, are resistant to the development of EAE following induction.<sup>134,135</sup> These mice do not show an increase in the production of proinflammatory chemokines and fail to develop CNS inflammation and signs of disease.<sup>134</sup> CCL2 levels increase before signs of disease begin and reach a maximum at the peak of disease signs in a Lewis rat model of EAE.<sup>136</sup> Astrocytes are believed to be the major source of CCL2 in MS<sup>130,131</sup> and EAE.<sup>137</sup> The role of CCL2 in the initiation and progression of MS and EAE is important, but not clearly defined.

BBB breakdown is often found in MS lesions with active inflammation and can be visualized using T<sub>1</sub>-weighted contrast-enhanced MRI. The MR contrast agent Gd-DTPA is used to detect BBB breakdown as it does not move through an intact BBB. A signal increase on T<sub>1</sub>-weighted MR images due to contrast enhancement is therefore known to correspond to a disrupted BBB. Loss of BBB integrity is an early event in MS lesion development, often preceding changes on other conventional MR images<sup>95,97</sup> and therefore is an important event in the initiation of the disease. The number of Gd-enhancing lesions in the CNS of MS patients has been used as an indicator of disease severity and an outcome measure during treatment in clinical trials.<sup>88</sup> EAE studies have shown histologically with the use of tracers<sup>41,44,47</sup> and with contrast-enhanced

MRI<sup>54,91,92,121</sup> that opening of the BBB is an early event in the development of the disease, though the exact mechanism that causes BBB disruption is currently unknown.

Inflammatory cells accumulate in the perivascular space between the endothelium and astrocytic foot processes of the BBB in transgenic mice that overexpress CCL2 in the CNS under control of a MBP promoter.<sup>138,139</sup> Transgenic mice that overexpress CCL2 show weight loss and infiltration of leukocytes across the BBB following PTx administration.<sup>138</sup> The development of MS is believed to have a genetic component<sup>12</sup> and in this animal model the susceptibility to an environmental toxin increases by genetically upregulating CCL2.<sup>138</sup> Similar observations of CNS inflammation were observed following PTx and CFA administration when CCL2 was overexpressed in astrocytes.<sup>140</sup> PTx is known to increase the permeability of the BBB in animal models of EAE and results in more severe course of disease.<sup>37,113</sup> Results from a previous study provided evidence to support the actions of PTx on endothelial cell plasticity through the promotion of angiogenesis.<sup>141</sup>

The integrity of the BBB in mice overexpressing CCL2 in the CNS pre- and post-PTx compared to wild type mice is currently unknown. Information regarding the relative BBB permeability in this model of inflammation may provide insights into the individual and combined effects of CCL2 upregulation and PTx administration, and thus the overall mechanism of inflammation. This study uses T<sub>1</sub>-weighted contrast-enhanced MRI to detect the relative extent and time course of BBB permeability in PTx and vehicle treated CCL2 transgenic and wild type mice.

## 6.2 METHODS

### 6.2.1 Animal Model

Female and male 11-13 week old transgenic mice (supplied by the University of Southern Denmark) overexpressing CCL2 in the CNS, under control of a MBP promoter,<sup>138,139</sup> were given a single intraperitoneal injection of PTx (Cedarlane Laboratories, Hornby, ON) at doses of 10 $\mu$ g/kg (n=8) or 20 $\mu$ g/kg (n=7). PTx stock solution (50 $\mu$ g/mL in PBS) was diluted to 1 $\mu$ g/mL or 2 $\mu$ g/mL using Hanks' balanced salt solution (HBSS; Invitrogen Corporation, Burlington, ON) for doses of 10 $\mu$ g/kg or 20 $\mu$ g/kg respectively. Transgenic mice that were administered the equivalent volume of HBSS (n=7) served as controls. Similarly, a group of female and male wild type B6D2F1 mice 11 weeks old (Charles River Canada, Saint Constant, QC) were given an injection of either 10 $\mu$ g/kg PTx (n=6), 20 $\mu$ g/kg PTx (n=5), or HBSS (n=5). The B6D2F1 mice are a cross between a female C57BL/6 mouse and a male DBA/2 mouse and the most appropriate control strain for this experiment, since the transgenic mice were generated by injecting transgenes into the eggs from a cross between C57BL/6J  $\times$  DBA/2 mice as previously described.<sup>139</sup> All mice were weighed, monitored daily, and housed in pathogen-free conditions with free access to food and water. All animal procedures were approved by the Institutional Animal Care Committee at the University of Manitoba.

### 6.2.2 MR Imaging

T<sub>2</sub>-weighted MR images and T<sub>1</sub>-weighted contrast-enhanced MR images of the brain were obtained using a quadrature volume coil as described in chapter 3 (slice positioning shown in Figure 3.3E,F). The animals were examined with MR imaging pre-PTx/HBSS injection and at days 1, 3, and where possible at day 5 post injection. Approximately half the transgenic and wild type did not have an imaging session at day 5 post-PTx/HBSS administration due to technical problems with the MR spectrometer.

### 6.2.3 MR Image Analysis

The T<sub>2</sub>-weighted images obtained were used to define the ROI of the brain (previously shown in Figure 3.5) and the contrast enhancement on T<sub>1</sub>-weighted images was quantified as described in chapter 3. The ROIs were superimposed onto the calculated difference images of percent enhancement to obtain the number of pixels above the selected intensity threshold of 20% within the ROI (Figures 6.1 and 6.2). Histograms of the number of pixels within the ROI on percent enhancement images of the brain versus intensity showed a normal distribution with the number of pixels centered on zero intensity and typically ranging between  $\pm 20\%$  intensity in wild type mice and transgenic mice receiving HBSS or before PTx injection. This range in intensity was likely due to random noise and motion artifacts on the T<sub>1</sub>-weighted images. Histograms of transgenic mice following PTx administration showed a distribution that is skewed to higher intensity (Figure 6.2C) with a range of intensities extending past 20%. An intensity threshold of 20% was selected in determining the number of pixels that most likely had an increased intensity due to BBB disruption. An

average histogram was also generated for each slice in transgenic and wild type mice pre-PTx/HBSS by plotting the average number of pixels across all transgenic or wild type mice at each percent intensity.

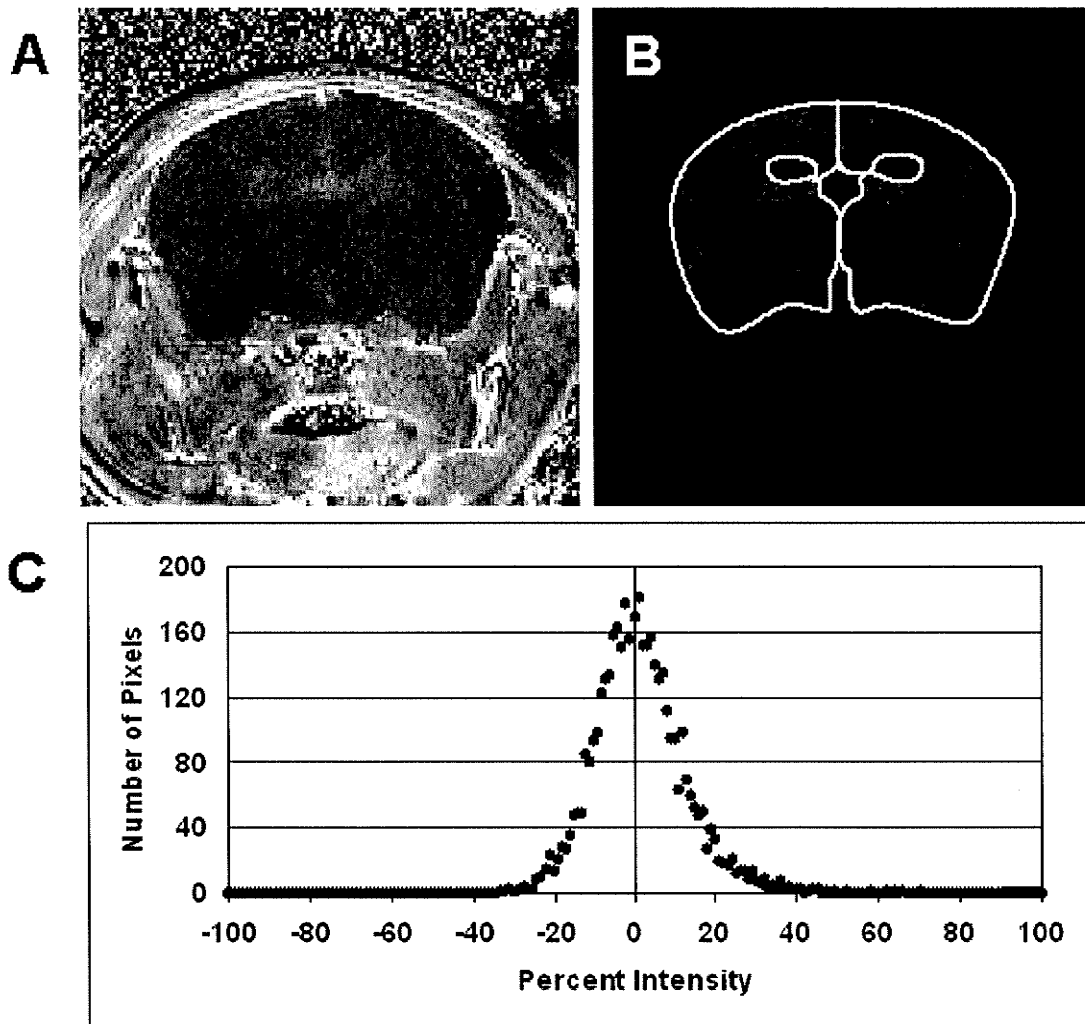


**Figure 6.1.** (A) Calculated image of percent enhancement (fourth slice from the anterior end of the brain; 12mmx12mm) taken from a transgenic mouse pre-PTx injection and (B) selecting only the pixels with 20% enhancement or above located within the ROI. (C) Corresponding histogram of the percent intensity within the ROI.

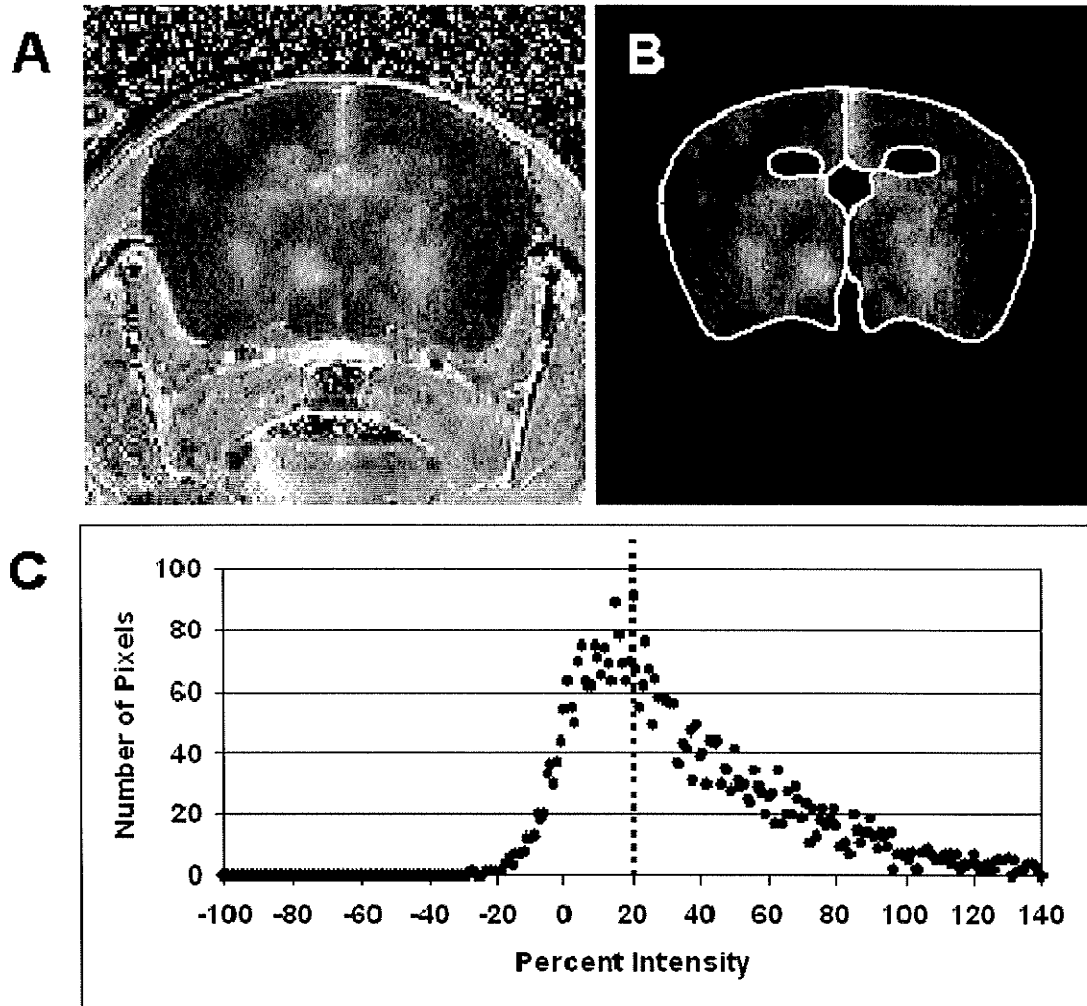


**Figure 6.2.** (A) Calculated image of percent enhancement (fourth slice from the anterior end of the brain; 12mm×12mm) taken from a transgenic mouse 5 days post 20µg/kg PTx injection and (B) selecting only the pixels with 20% enhancement or above located within the ROI. (C) Corresponding histogram of the percent intensity within the ROI indicating the threshold used to select enhancing pixels.

#### *6.2.4 Tissue Processing*

After the last imaging session on day 5 post-PTx/HBSS injection, a solution of 0.25g/kg of 70kD dextran conjugated to fluorescent Texas Red (25mg/mL in PBS, lysine fixable, 3 moles dye/mol dextran; Molecular Probes, Eugene, OR) was injected into the left ventricle of the heart of each mouse. After one minute the mice were perfusion-fixed using phosphate buffered 10% formalin. The imaged region of the brain was sliced into four sections 2mm thick (Figure 6.3). Brain sections were then embedded into paraffin and tissue sections 6 $\mu$ m thick were cut onto glass slides. Laminin was detected by incubating sections overnight using anti-laminin (1:50; rabbit polyclonal antibody Ab-1; NeoMarkers, Fremont, CA) followed by biotin-conjugated secondary antibody, streptavidin-peroxidase, and DAB. Sections were incubated with anti-GFAP (1:250; rabbit polyclonal antibody; DakoCytomation, Mississauga, ON) to detect astrocytes followed by staining for 30 seconds using 4',6-diamidino-2-phenyl indole (DAPI; 1:1000; Sigma, St. Louis, MO) to visualize nuclei. Sections were stained with H&E to visualize general histological features.

#### *6.2.5 Statistical Analysis*

Data were reported as mean  $\pm$  SEM. The percent of pixels above 20% increased enhancement on calculated difference images and the percent change in weight between transgenic and wild type mice before and after PTx/HBSS administration were compared statistically using ANOVA followed by Fisher's PLSD post hoc test.

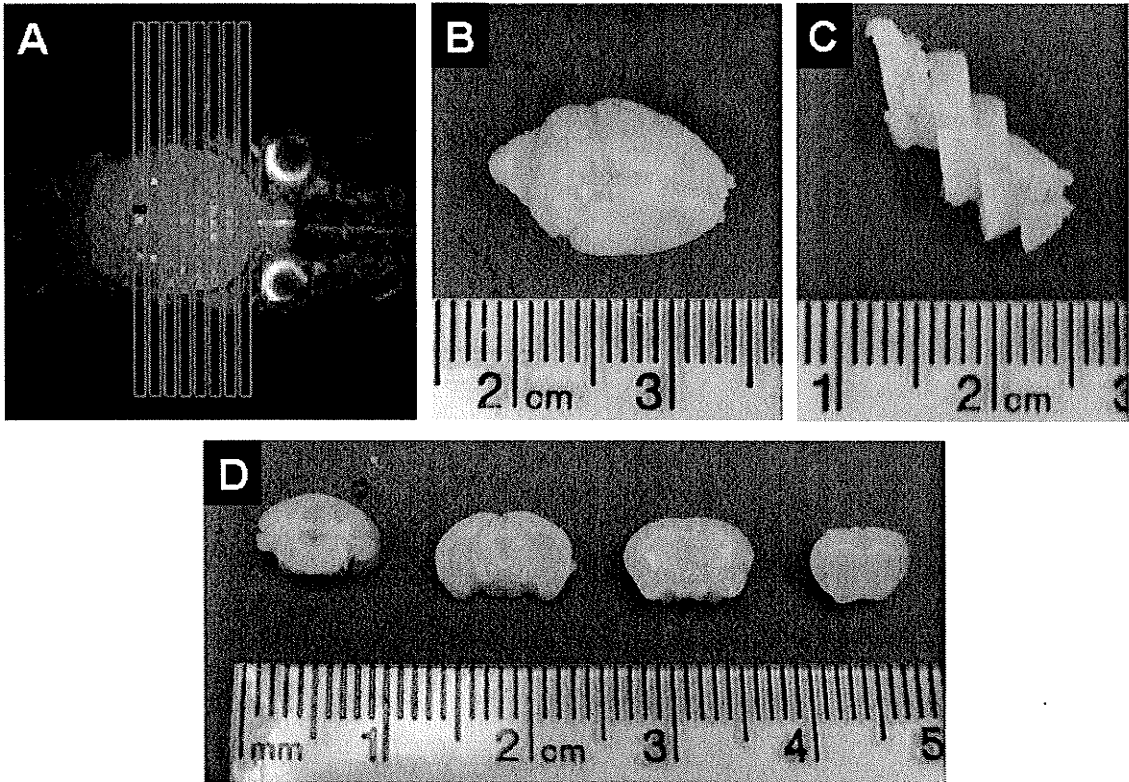


**Figure 6.3.** The imaged region of the brain (A) was removed from the skull (B) and cut into 2mm coronal tissue sections for paraffin embedding (C, D).

## 6.3 RESULTS

### 6.3.1 MR Imaging

A set of 8 coronal T<sub>1</sub>-weighted images of the brain was obtained (pre- and post-contrast enhancement) from each mouse at imaging sessions before and 1, 3, and where possible 5 days after HBSS or PTx injections. One transgenic mouse that received an initial dose of 20μg/kg PTx died under anesthetic during imaging on day 3 and a second transgenic mouse that received an initial dose of 10μg/kg PTx died spontaneously on day 5.

Focal areas of enhancement were scattered throughout coronal brain slices of CCL2 transgenic mice that had been injected with PTx (Figures 6.4, 6.5B). Enhancement was observed predominantly in basal areas of the brain and surrounding the ventricles with fewer regions of enhancement in the cortex. The number and area of focal enhancements increased in more posterior brain slices with greatest enhancement in the midbrain and very little enhancement in the frontal lobes (Figure 6.5). No focal enhancement was observed on contrast enhanced T<sub>1</sub>-weighted images within the brains of CCL2 transgenic mice that were administered HBSS or wild type mice that were administered either dose of PTx or HBSS (Figure 6.4).

A relative measure of BBB disruption over time was determined quantitatively by calculating the percentage of pixels with a contrast enhancement above 20% within the brain on calculated percent difference images. Only the posterior six slices were used to calculate the number of pixels above the 20% intensity threshold because the slices located more anterior had generally very little contrast enhancement. PTx

administration of either dose in CCL2 transgenic mice caused an increase in contrast enhancement that was maximal at day 3 (Figure 6.6). Following the administration of low and high dose PTx, there was a significant increase in the area of enhancement above 20% ( $p < 0.01$  and  $p < 0.005$  respectively) within the brain at day 3 post-PTx relative to HBSS (Figure 6.6). No significant differences were found between groups of CCL2 transgenic mice pre-PTx/HBSS administration and following HBSS administration at days 1, 3, or 5 or between wild type mice pre- and post-PTx/HBSS. Pre-PTx/HBSS injection there was a significant difference ( $p < 0.0001$ ) in the percentage of pixels with an enhancement greater than 20% between transgenic and wild type mice, though this could not be observed visually from the calculated percent difference images. The difference in the area of enhancement with intensity greater than 20% between wild type and transgenic mice receiving HBSS was constant and did not vary significantly with time. Average histograms from transgenic mice pre-PTx/HBSS showed greater asymmetry with more skewing to higher intensities than wild type mice (Figure 6.7).

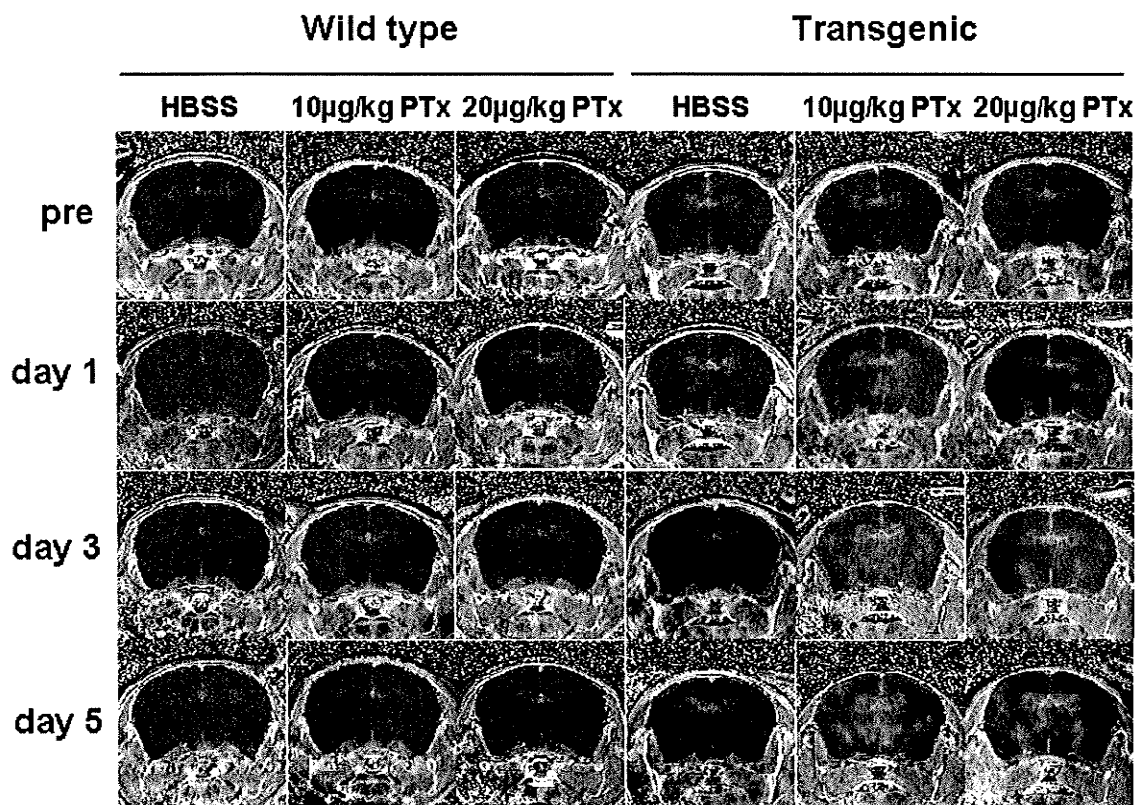


**Figure 6.4.** Representative coronal calculated difference images of contrast enhancement (12mm $\times$ 12mm) of the fourth anterior slice taken from wild type and transgenic mice that were administered HBSS, 10 $\mu$ g/kg PTx, or 20 $\mu$ g/kg PTx. MR images were obtained pre-injection, days 1, 3 and 5 post-injection from the same animal.

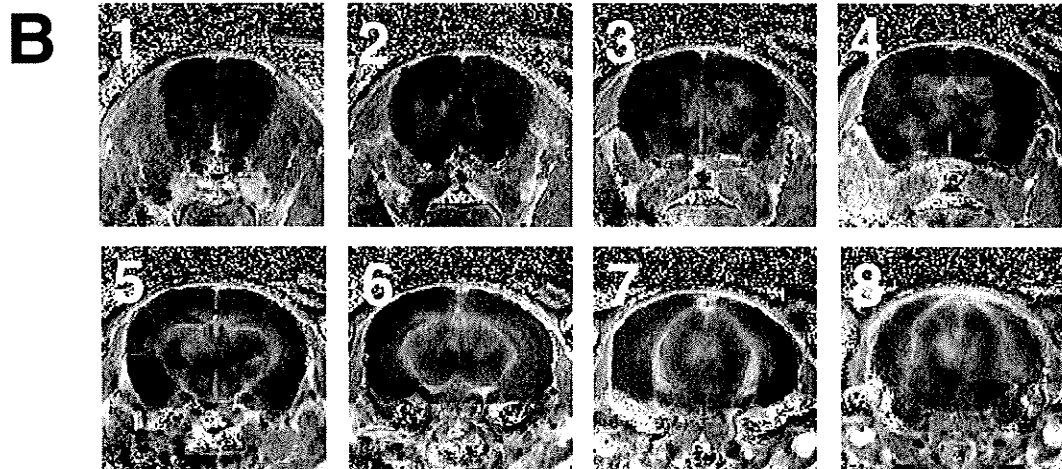
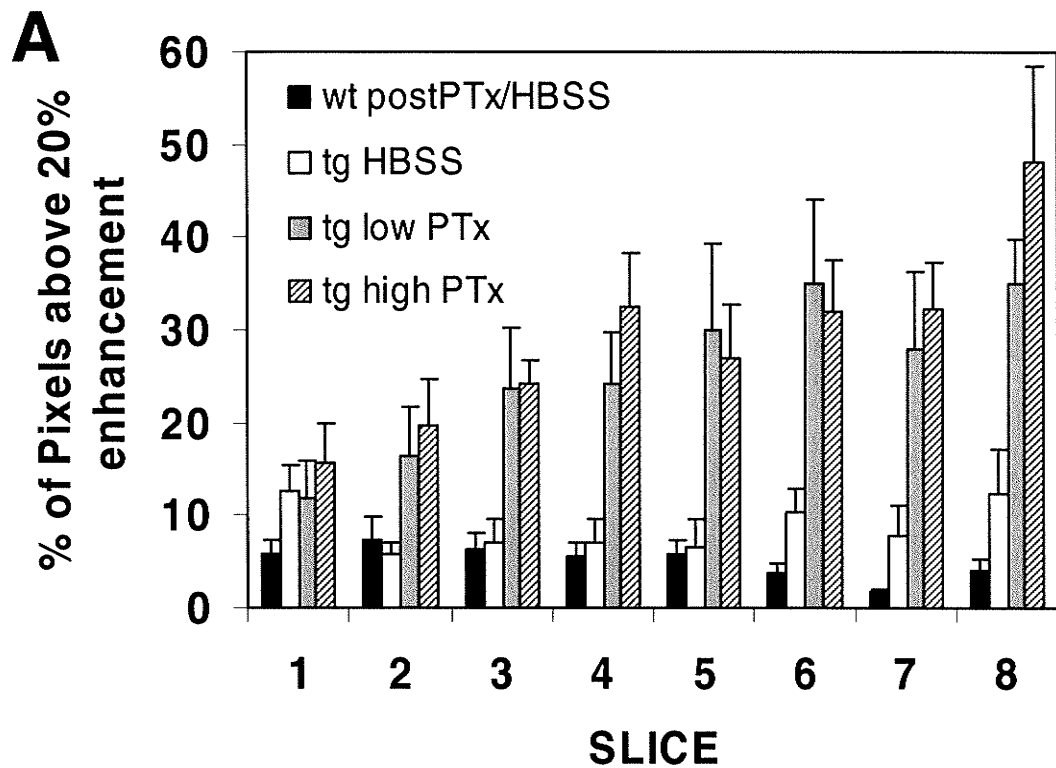


**Figure 6.5.** (A) The percentage of enhancing pixels within each brain slice that have an intensity of 20% or greater at day 3 post injection. (B) A complete set of calculated difference images obtained from a transgenic mouse following 20µg/kg PTx on day 3.

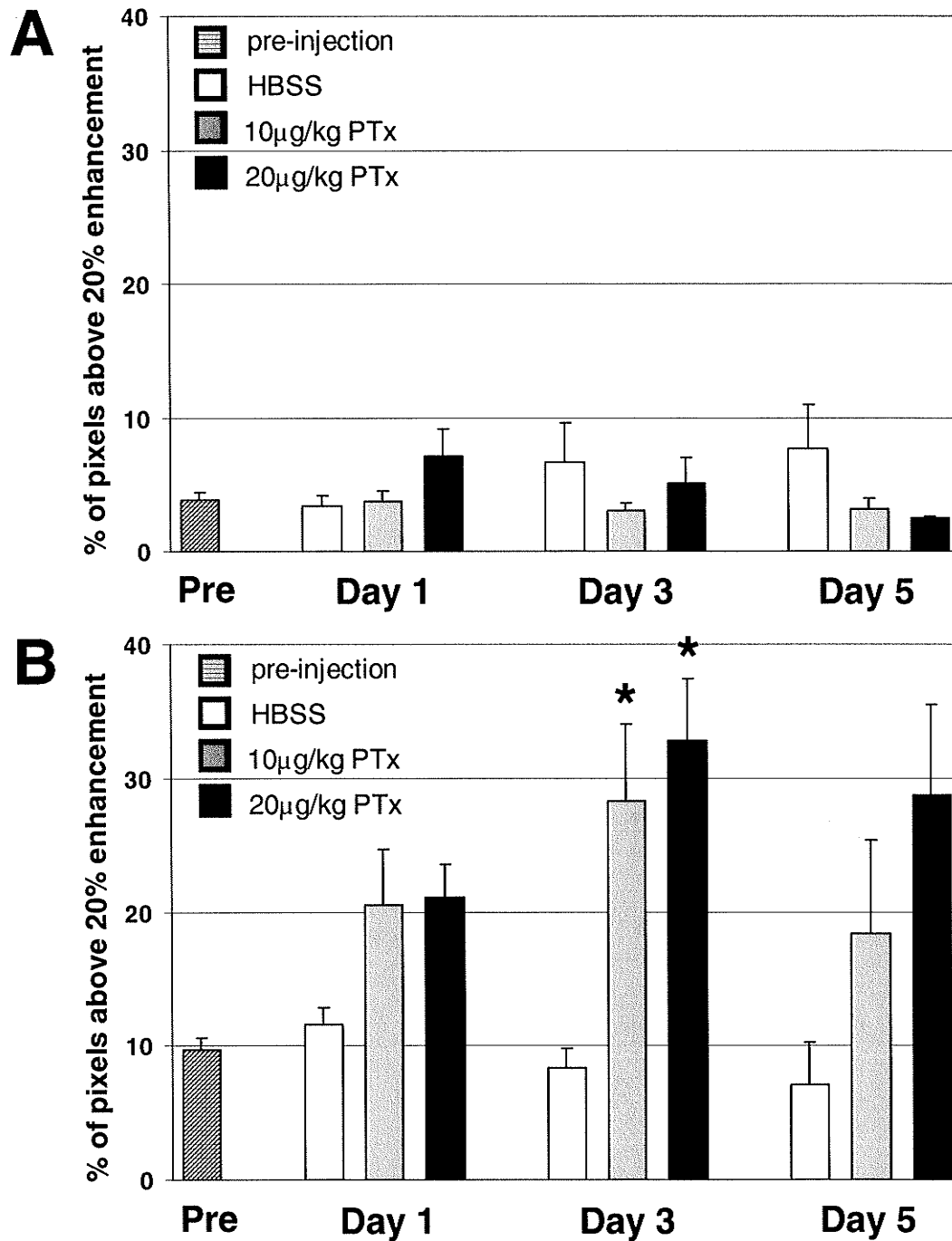


**Figure 6.6.** The percentage of pixels in the posterior 6 slices of the brain showing a 20% or greater increase in intensity on calculated percent enhancement images for (A) wild type and (B) transgenic mice pre-injection and days 1, 3 and 5 post HBSS, post 10µg/kg PTx, and post 20µg/kg PTx.

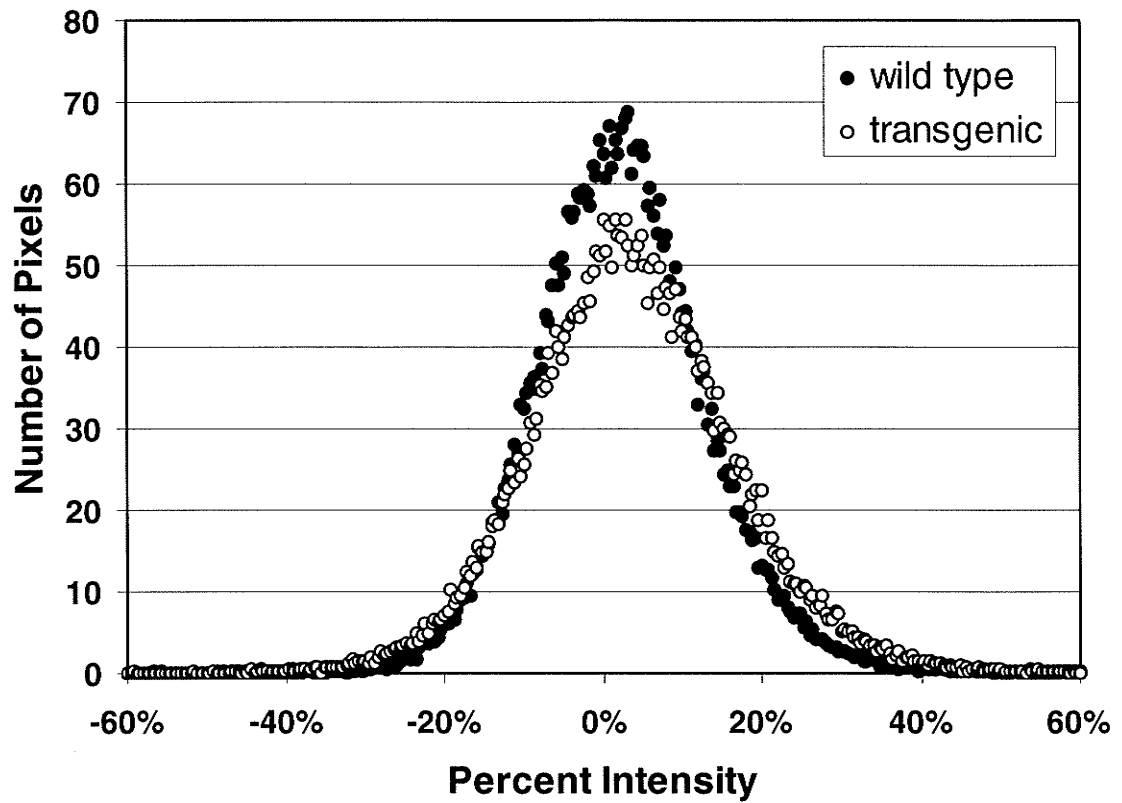


**Figure 6.7.** Average histogram of the third anterior slice for wild type and transgenic mice before the administration of PTx or HBSS.

### 6.3.2 *Clinical Signs*

There were no significant differences in the change in weight between any of the groups of mice at day 1 post-PTx/HBSS injection (Figure 6.8). Subsequently, a loss in weight was observed only in CCL2 transgenic mice after PTx injection, with greater losses in mice receiving the higher dose. At days 2, 3, 4, and 5 post-PTx/HBSS injection there was a significantly greater loss in weight in CCL2 transgenic mice injected with PTx at either dose compared to wild type mice (for low dose PTx:  $p < 0.005$ ,  $p < 0.01$ ,  $p < 0.0005$ ,  $p < 0.001$  respectively and for high dose PTx:  $p < 0.0001$  at each day) as well as in transgenic mice that received either dose of PTx compared to transgenic mice that received HBSS (for low dose PTx:  $p < 0.05$  at each day and for high dose PTx:  $p < 0.005$  at day 2 and  $p < 0.0005$  at days 3 to 5). Changes in weight were not significantly different between CCL2 transgenic mice injected with HBSS and wild type mice at any time point (Figure 6.8). A significant dose dependent difference in weight loss was present between transgenic mice that received the high and low doses of PTx at days 3 ( $p < 0.05$ ) and 4 ( $p < 0.05$ ). The largest drop in weight was at day 5 in transgenic mice that were administered the low dose PTx (average 5.5%) and the high dose PTx (average 9.6%). On average, the trend was that transgenic mice receiving the high dose PTx lost twice as much weight as transgenic mice receiving the low dose PTx (Figure 6.8).

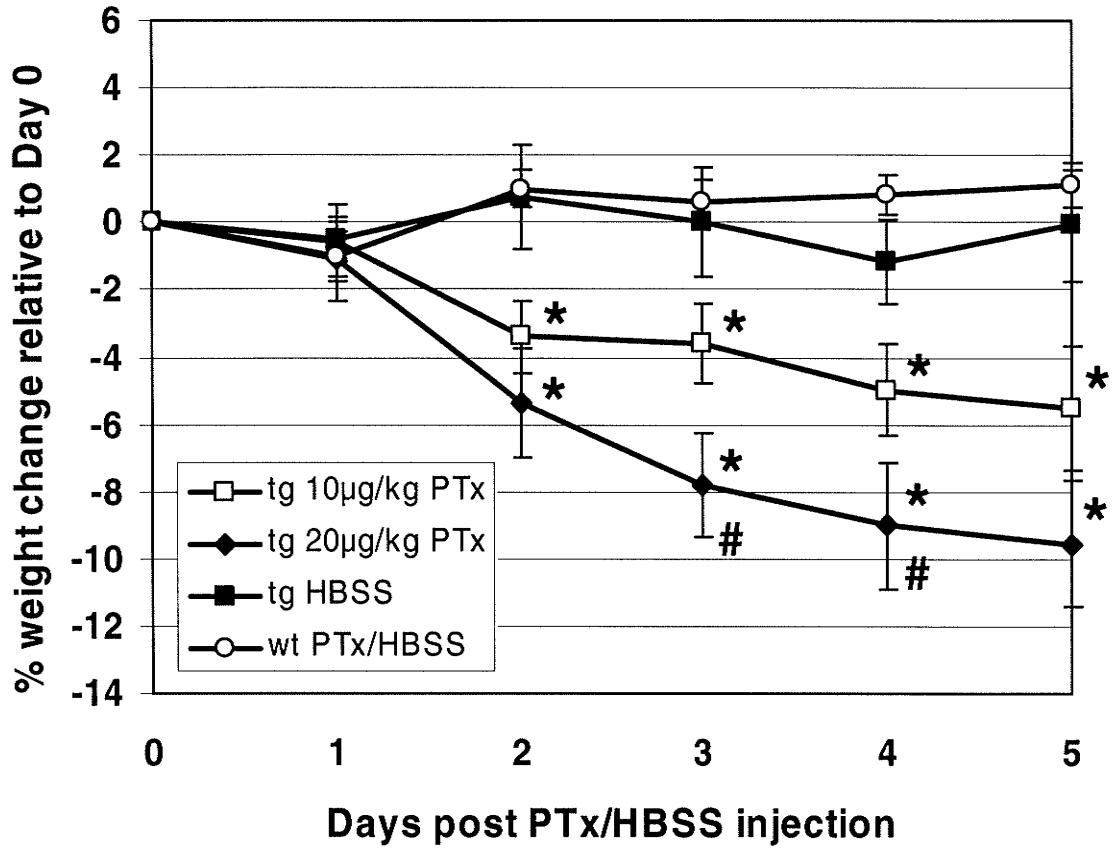
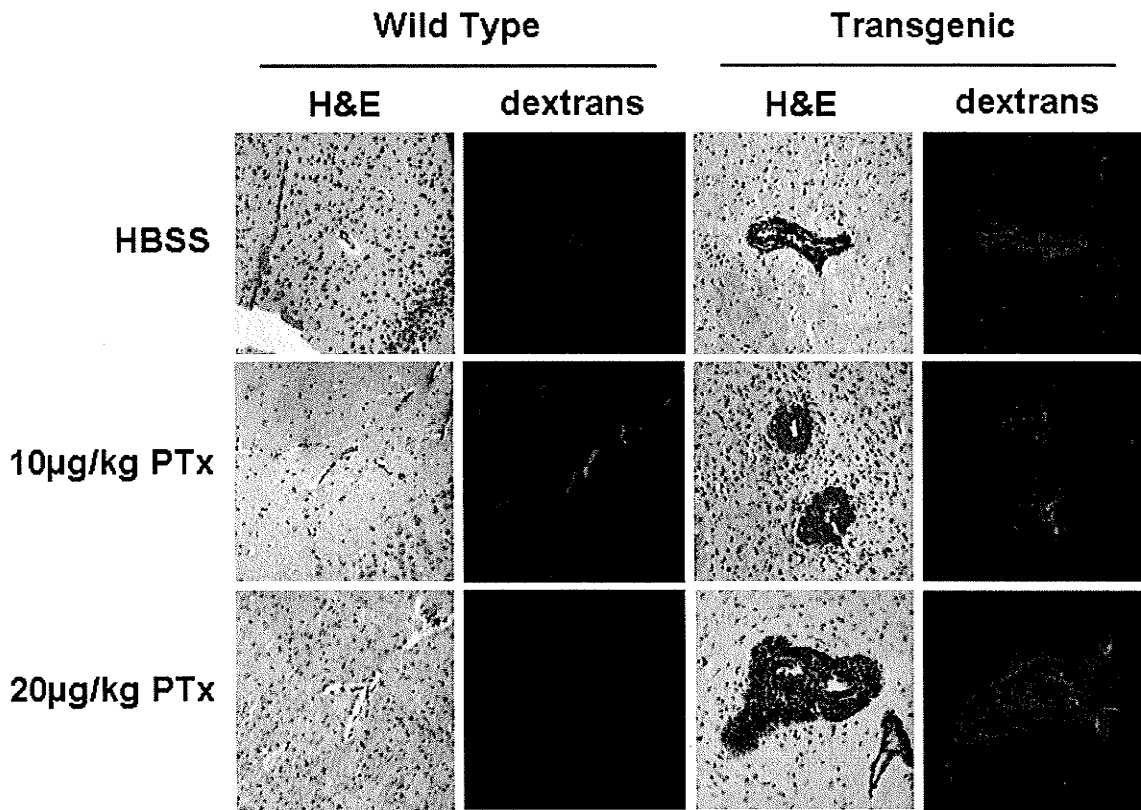


**Figure 6.8.** The change in weight following the injection of HBSS or PTx in transgenic and wild type mice over 5 days. \* differs from wt PTx/HBSS and tg HBSS, # differs from tg 10µg/kg PTx.

### 6.3.3 Histology

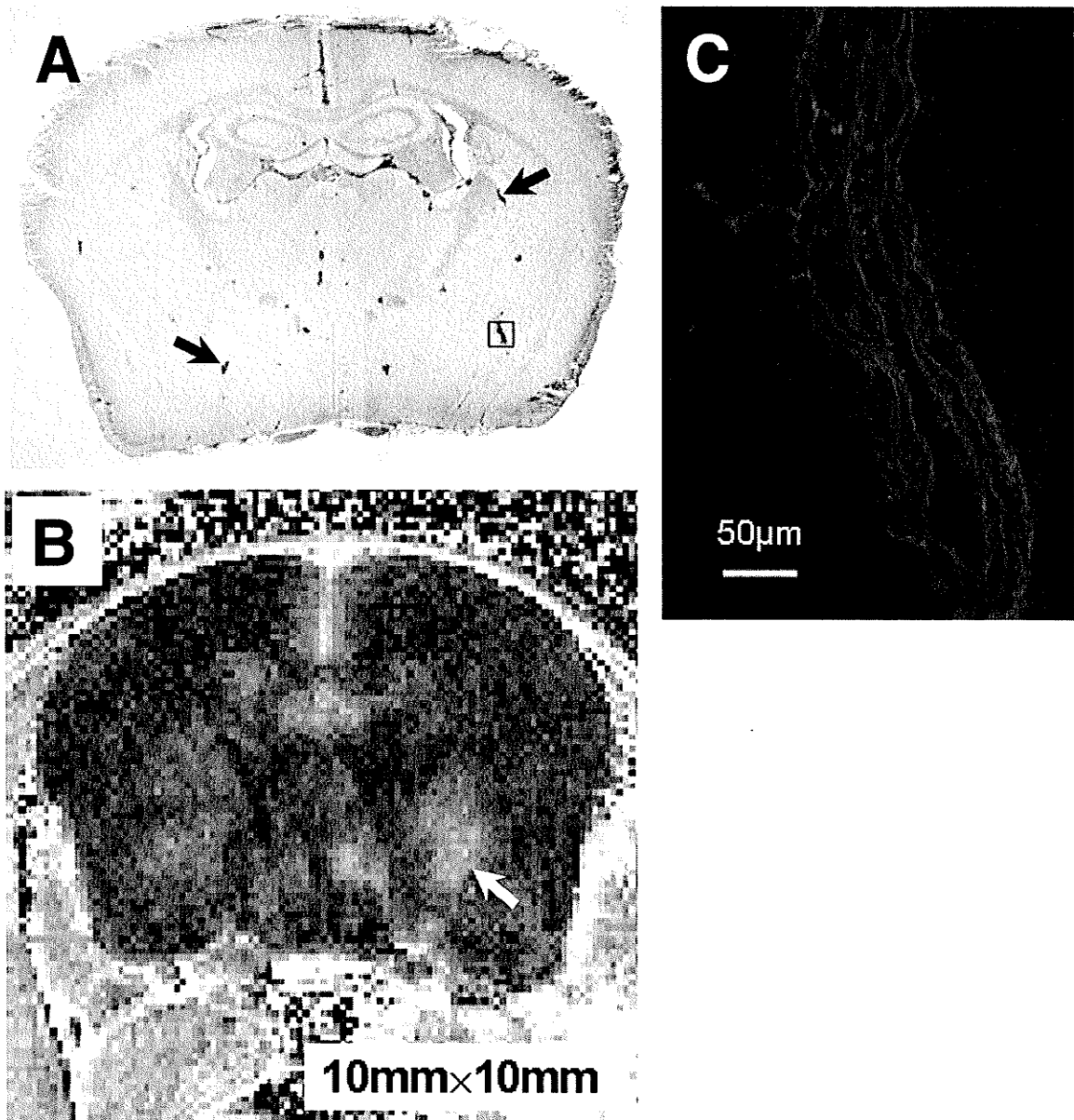
Mice were perfusion-fixed following the last imaging session and tissue sections of the brains were examined for inflammatory cell infiltrates on H&E stained sections. Sites of BBB opening were revealed by the presence of fluorescent dextrans, which were observed by epifluorescence microscopy. Large numbers of inflammatory cells and fluorescent dextrans were observed within the perivascular spaces of veins in the brains of all CCL2 transgenic mice (Figure 6.9). These inflammatory cells surrounded veins in the cerebral cortex, striatum and white matter, as well as large veins in the medulla and cerebellar white matter. Inflammatory cells were prominent in the subarachnoid space surrounding large veins and followed along their superficial sites of penetration. However, not all the large vessels were surrounded by inflammatory cells in the perivascular space, rather the inflamed vessels were randomly distributed.

Following PTx administration, inflammatory cells were observed within the brain parenchyma surrounding veins in CCL2 transgenic mice. Fluorescent dextrans were also present in the parenchyma (Figure 6.9). In transgenic mice that received HBSS, inflammatory cells remained confined to the perivascular space with no evidence of dextrans in brain parenchyma (Figure 6.9). Transgenic mice that received an injection of either PTx or HBSS showed fragmented nuclear debris among the inflammatory cells suggesting that approximately 10% of the inflammatory cells were apoptotic. Based on nuclear morphology approximately 5% of the infiltrated cells were neutrophils. No inflammatory cells were observed within the perivascular space of brain sections of wild type mice following PTx or HBSS (Figure 6.9).

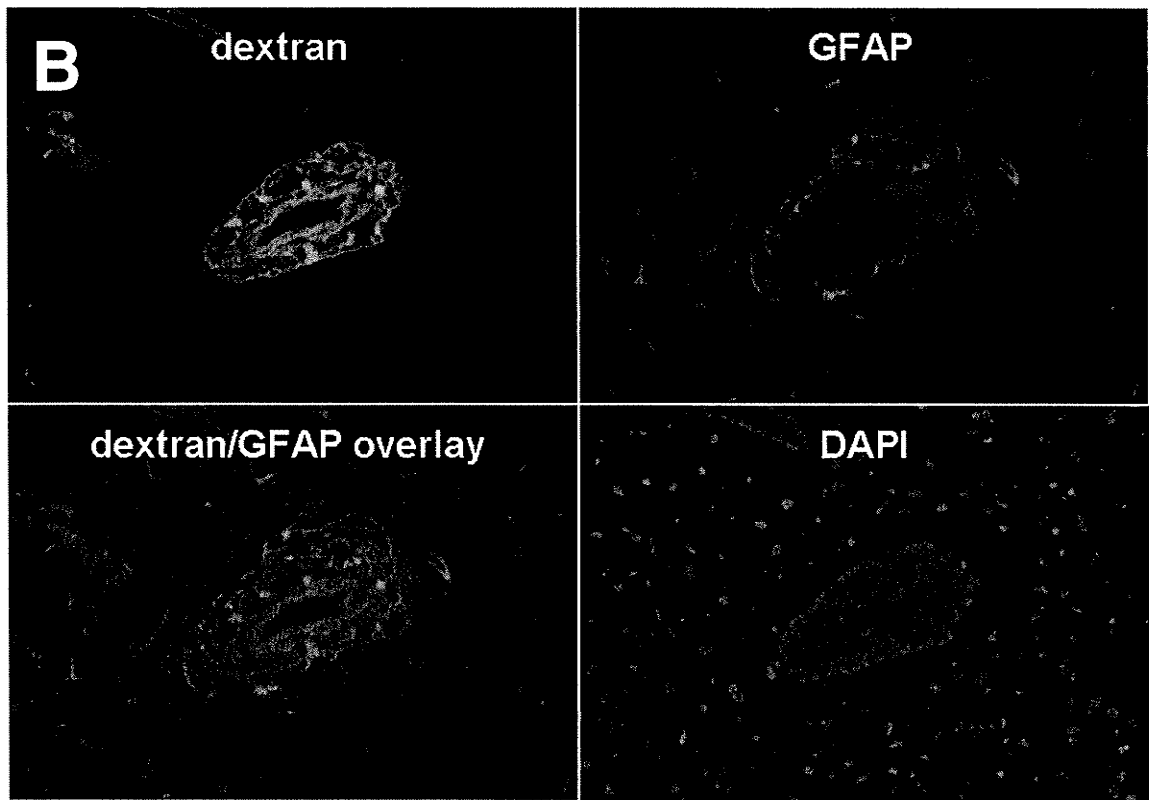
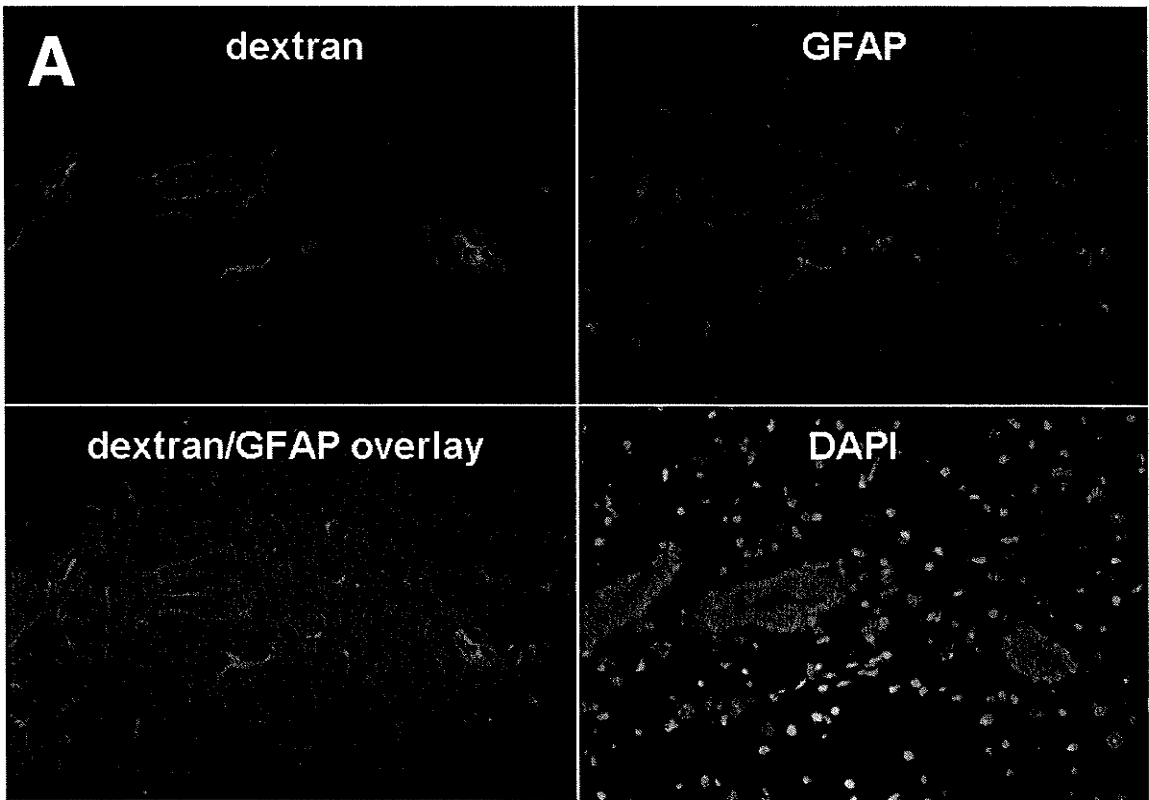


**Figure 6.9.** Histological sections stained with H&E to observe general features of inflammation and corresponding unstained sections to visualize regions of fluorescence due to dextrans surrounding blood vessels. Sections were taken from representative wild type and transgenic mice following HBSS or PTx administration and correspond to the final imaging session on day 5 post injection.

Histologically identifiable perivascular inflammation corresponded well to sites of Gd-DTPA enhancement on the MR images. However, the distribution of these cells and the spread of dextrans were much more confined than the areas of MR enhancement (Figure 6.10). Staining for nuclei with DAPI confirmed the presence of large numbers of inflammatory cells within the perivascular space. The endothelial barrier was visualized by staining for laminin and dextrans were present across the endothelial barrier in all groups of transgenic mice (Figure 6.11C). The overlay of GFAP immunolabeling with fluorescent dextrans around inflamed vessels of the brains from CCL2 transgenic control mice showed that dextrans were confined to the perivascular space, i.e. they did not cross the astrocytic barrier. However, in transgenic mice that received PTx, dextrans moved beyond the astrocytic barrier (Figure 6.11A,B).



**Figure 6.10.** (A) A histological coronal section of the brain (6 $\mu$ m thick) of a CCL2 transgenic mouse at day 5 following the administration of 20 $\mu$ g/kg PTx stained with H&E for general features of inflammation (arrows indicate aggregates of inflammatory cells) and (B) the corresponding calculated contrast-enhanced percent difference MR image (750 $\mu$ m slice thickness). (C) The inflamed vessel outlined in (A) at a higher magnification shows leaking dextrans, which corresponds to the focal area of enhancement seen in (B).



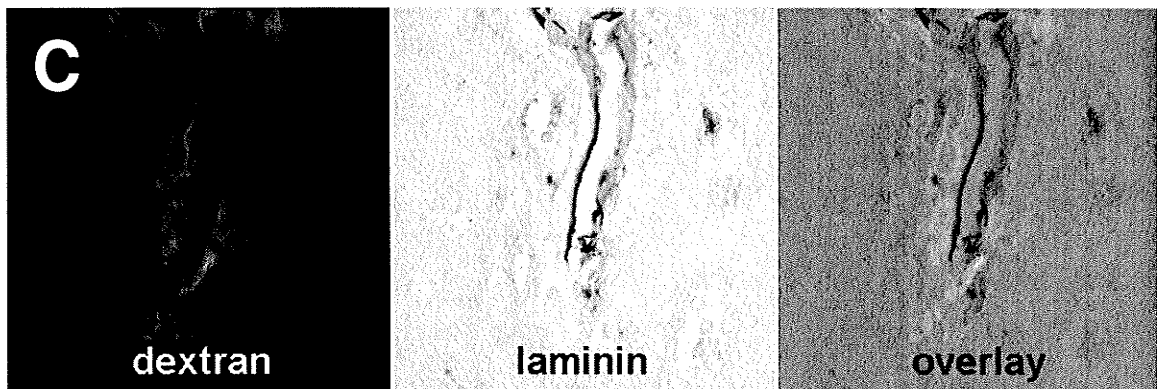


**Figure 6.11.** (A) A histological section of a vessel that is leaking dextrans with corresponding staining for GFAP and DAPI from a CCL2 transgenic mouse that was administered 20 $\mu$ g/kg PTx. An overlay of dextrans and GFAP indicates that the dextrans have moved past the astrocytic barrier. (B) The same assessment of a histological section of a non-leaking vessel shows dextrans confined to the perivascular space. (C) A similar histological section taken from a CCL2 transgenic mouse that was administered 10 $\mu$ g/kg PTx stained for laminin shows that the corresponding dextrans have crossed the endothelial barrier as seen in the overlay image.

## 6.4 DISCUSSION

The breakdown of the BBB and the presence of CCL2 are both known to have a role in the initiation of disease signs in EAE and MS. Therefore, the effects of upregulated CCL2 before and after PTx injection was studied in this model using T<sub>1</sub>-weighted contrast-enhanced MRI. As previously described, the upregulation of CCL2 within the CNS caused inflammatory cells to cross the endothelial cell barrier and accumulate within the perivascular space of vessels in the brain;<sup>138</sup> however, these mice did not show any clinical signs of disease. In this study, contrast-enhanced MR images did not show any evidence of BBB breakdown and histological examination of tissue sections did not show the presence of dextrans in the CNS parenchyma outside vessels in mice with upregulated CCL2.

In a previous study of mice with EAE using electron microscopy, there was no evidence of loss of integrity of the BBB during leukocyte migration.<sup>125</sup> These observations provided supporting evidence for a transcellular migration pathway across the endothelium with tight junctions remaining intact. Considering a paracellular migration pathway, CCL2 has been found to have a role in the alteration of tight junctions in the endothelium both in vitro and in vivo.<sup>142-144</sup> A decrease in the expression of the tight junction proteins occludin, claudin-5, ZO-1, and ZO-2 were observed following intracerebral injection of CCL2 in mice.<sup>143</sup> The effects of CCL2 on a BBB co-culture model with astrocytes showed increased barrier permeability when endothelial cells were CCR2<sup>+/+</sup> and astrocytes CCR2<sup>-/-</sup>, but not when endothelial cells were CCR2<sup>-/-</sup> and astrocytes CCR2<sup>+/+</sup>.<sup>143</sup> These results suggest that CCL2 specifically

acts on the endothelium to cause increased BBB permeability. In our animal model, no signs of BBB disruption could be visualized on calculated contrast-enhanced MR images where inflammatory cells crossed the endothelium and accumulated in the perivascular space. The presence of CCL2 alone was not enough to cause an inflammatory response into the CNS and complete BBB breakdown. However, histograms obtained from calculated images of contrast enhancement showed subtle asymmetry in the curves from wild type and CCL2 transgenic mice pre-PTx/HBSS with greater skewing to higher intensities in the transgenic mice. This suggests an accumulation of Gd-DTPA contrast agent within the perivascular space surrounding vessels in transgenic mice, which cannot be visualized on the calculated images. The distribution asymmetry with slight skewing to higher intensities observed on the average histograms in wild type mice may be due to the presence of the contrast agent in the blood stream. The presence of fluorescent dextran accumulation in the perivascular space in CCL2 transgenic mice before the administration of PTx or HBSS confirms that the endothelial barrier is permeable to the tracer; however, dextrans were not found to cross the astrocytic barrier. The more confined spread of dextrans in comparison to the areas of MR enhancement, suggests either greater sensitivity using MR imaging or greater diffusion of the smaller molecule used for MR contrast. These observations from histology and contrast-enhanced MR imaging indicate increased permeability through the endothelial barrier while the astrocytic barrier remains intact and prevents the movement of inflammatory cells, dextran tracer, and Gd-DTPA contrast agent into the brain parenchyma.

Wild type mice following PTx administration did not show any signs of BBB disruption. Previously, PTx caused increased permeability to horseradish peroxidase tracer in a monolayer of brain capillary endothelial cells.<sup>145</sup> Enhanced leakage across the microvasculature in mice due to PTx was also observed following histamine administration<sup>146,147</sup> as well as during the onset of EAE.<sup>147</sup> However, in a previous study of a SJL/J mouse model of EAE, the group of mice that only received PTx did not show any indications of BBB permeability.<sup>37</sup>

When PTx was injected into CCL2 transgenic mice, inflammatory cells infiltrated into the brain tissue surrounding blood vessels and dextran tracer had leaked into the brain parenchyma. The maximum area of focal enhancements on contrast-enhanced MR images was found to be at day 3 following both doses of PTx in CCL2 transgenic mice, suggesting a transient BBB opening in this model. BBB opening begins to resolve by day 5. Only the combination of PTx and the overexpression of CCL2 in the CNS resulted in increased contrast enhancement and weight loss in this model indicating that both genes and the environment play a role in the initiation of BBB permeability and infiltration of inflammatory cells into the CNS. The perivascular cuffing of inflammatory cells increased the susceptibility of mice to weight loss and CNS inflammation. This is relevant to MS, as a genetically predisposed individual may be more prone to disease onset following an environmental stimulus. This may provide insight into the mechanism needed to disrupt the BBB.

Metalloproteinases are known to degrade the extracellular matrix components of the BBB, and metalloproteinase genes were previously, MMP-8 and MMP-10 were found to be significantly upregulated in this CCL2 transgenic mouse model following

PTx administration.<sup>138</sup> This occurs along with an increase in proinflammatory cytokines IL-1 $\beta$  and TNF- $\alpha$ , which have been shown to play a role in leukocyte migration into the CNS.<sup>138</sup> CCL2 transgenic mice showed increased levels of MMP-10, MMP-12, IL-1 $\beta$  and TNF- $\alpha$  even before PTx injection, but our results indicate these levels were not sufficient to cause complete BBB permeability. The addition of PTx to the model was the additional stimulus needed to cause BBB breakdown and stimulate the cells accumulated in the perivascular space to cross the astrocytic cell barrier and enter the brain parenchyma.

## **CHAPTER VII**

# **MAGNETIC RESONANCE IMAGING OF THE SPINAL CORD OF A1 ADENOSINE RECEPTOR KNOCKOUT MICE WITH EXPERIMENTAL AUTOIMMUNE ENCEPHALOMYELITIS**

## 7.1 INTRODUCTION

Adenosine receptors are G protein-coupled receptors found on most cells and tissues in the body with four known subtypes (A1, A2a, A2b, and A3).<sup>148,149</sup> The A1 adenosine receptor (A1AR) is highly expressed within the CNS<sup>149</sup> and is known to have a role in neuroprotection and the reduction of inflammation in the CNS during pathological conditions.<sup>150</sup> The anti-inflammatory effects of A1AR activation make it a potential therapeutic target in MS. A decrease in the expression of A1AR was observed on peripheral blood monocytes and in brain tissue of patients with MS as compared to peripheral blood monocytes in healthy controls and brain tissue from patients who died of other causes.<sup>151,152</sup> This suggests that decreased levels of the A1AR may play a role in the pathogenesis of MS.

An A1AR agonist caused a decrease in the release of the proinflammatory cytokine TNF- $\alpha$  following the stimulation of promonocytic cells *in vitro*<sup>153</sup> as well as a decrease in the plasma levels of TNF- $\alpha$  following lipopolysaccharide (LPS) treatment in mice.<sup>154,155</sup> Adenosine was also found to inhibit the LPS-induced release of TNF- $\alpha$  on activated human monocytes *in vitro*,<sup>154,156</sup> while enhancing the expression of the anti-inflammatory cytokines IL-6 in astrocytes<sup>157</sup> and 1L-10 in monocytes<sup>158</sup> *in vitro*. The levels of TNF- $\alpha$  in brain tissue<sup>151</sup> and plasma<sup>152</sup> of MS patients were significantly elevated when compared to control subjects and plasma levels of adenosine were decreased.<sup>152</sup> Activation of A1AR on peripheral blood monocytes in culture from healthy subjects caused a significant decrease in TNF- $\alpha$  production within the tissue culture supernatants following stimulation, but the same did not occur using peripheral

blood monocytes taken from MS patients.<sup>152</sup> A correlation between the levels of TNF- $\alpha$  in the CSF of patients with chronic progressive MS and disease severity was found, suggesting the importance of TNF- $\alpha$  in disease progression.<sup>159</sup> Messenger RNA levels of TNF- $\alpha$  in peripheral blood monocytes were found to increase in patients with relapsing-remitting MS during the 4 weeks before a relapse.<sup>30</sup>

A strong correlation was found between the levels of TNF- $\alpha$  and albumin in the CSF and serum in patients with active MS.<sup>160</sup> The ratio of albumin in CSF to serum provides a measure of the degree of BBB disruption and therefore suggests a possible role of TNF- $\alpha$  in the breakdown of the BBB in active disease.<sup>160</sup> A decrease in the release of proinflammatory cytokines such as TNF- $\alpha$  following the activation of the A1AR may contribute to improved stability of the BBB.

A previous study showed that A1AR<sup>-/-</sup> mice with EAE developed more demyelination, more axonal damage, greater severity of clinical signs, and increased activation of microglia and macrophages as compared to A1AR<sup>+/+</sup> mice with EAE.<sup>111</sup> A1AR<sup>-/-</sup> mice had increased gene expression of the various proinflammatory mediators IL-1 $\beta$ , iNOS, and MMP-9 and -12, while levels of anti-inflammatory cytokines IL-10 and IL-4 were decreased in the lumbar spinal cord.<sup>111</sup> These results provide further evidence that A1AR has a role in the regulation of inflammation.

The effects of increased A1AR expression on BBB or BSB permeability in mouse models of EAE or patients with MS are currently unknown. The objective of this study was to use T<sub>1</sub>-weighted contrast-enhanced MRI to determine the relative BSB permeability within lumbar spinal cord at the initial onset of signs and at disease remission in A1AR<sup>+/+</sup>, A1AR<sup>+/-</sup>, and A1AR<sup>-/-</sup> mice with EAE.

## 7.2 METHODS

### *7.2.1 Induction of EAE and Scoring System*

EAE was induced in 20 female C57/BL6/129 mice (supplied by the University of Calgary) at ages ranging from 4 to 8 months as described in chapter 3. The mice were grouped as A1AR<sup>+/+</sup> wild type (n=7), A1AR<sup>+/-</sup> heterozygous (n=5), and A1AR<sup>-/-</sup> knockout (n=8) mice. The A1AR<sup>+/+</sup>, A1AR<sup>+/-</sup>, and A1AR<sup>-/-</sup> mice were littermates that were generated as previously described.<sup>161</sup> A group of control C57/BL6/129 mice (n=5) received the same preparations used for EAE induction but without MOG<sub>35-55</sub> and were grouped as A1AR<sup>+/+</sup> wild type (n=2), A1AR<sup>+/-</sup> heterozygous (n=1), and A1AR<sup>-/-</sup> knockout (n=2) mice. An additional group of control C57/BL6 mice (n=4) was injected with saline only. Mice were weighed and scored daily as described in chapter 3.

### *7.2.2 MR Imaging*

MR images of the lumbar spinal cord were obtained using a quadrature surface coil as described in chapter 3. The same imaging protocol (T<sub>2</sub>- and T<sub>1</sub>-weighted MRI followed by contrast-enhanced T<sub>1</sub>-weighted MRI) using two sets of interleaved slices as detailed in chapter 3 and Figure 3.3A,B was applied in this study. A1AR<sup>+/+</sup> (n=1) and A1AR<sup>-/-</sup> (n=1) mice were imaged before disease signs were observed. MR imaging was then performed at the initial onset of disease signs and again between day 30 and 33 post-MOG injection for all groups of mice. After the last imaging session animals were sacrificed by perfusion-fixation through the heart using phosphate buffered formalin.

### *7.2.3 MR Image Analysis*

The contrast enhancement within the spinal cord on contrast-enhanced T<sub>1</sub>-weighted images was quantified as previously described in chapter 3. The spinal cord volume across all 11 T<sub>2</sub>-weighted images obtained as two interleaved sets of images was calculated as the sum of all ROI areas (mm<sup>2</sup>) x 0.75mm slice thickness.

### *7.2.4 Statistical Analysis*

Data from each group of animals were reported as mean ± SEM. Scores were analyzed in terms of maximum score, disease burden (the sum of scores divided by the number of days starting with day 8), and day of disease onset. The maximum and minimum weight that was reached for each mouse was determined during the disease progression and the difference between these two weights was the calculated drop in weight. Percent intensity, maximum score, disease burden, day of disease onset, drop in weight, and spinal cord volume data were compared statistically using ANOVA followed by post hoc t tests or simply a t test in the case of only 2 groups.

## 7.3 RESULTS

### *7.3.1 Behaviour Scores and Changes in Weight*

A1AR<sup>+/+</sup> (n=5), A1AR<sup>+/-</sup> (n=4), and A1AR<sup>-/-</sup> (n=8) mice with EAE were examined with MR imaging at the first signs of disease, which was at day 11 to 18 post-inoculation for the majority of the mice with an additional two mice at day 22 and 28 post-inoculation. Control mice (n=4 C57Bl/6, n=1 A1AR<sup>+/+</sup>, n=2 A1AR<sup>-/-</sup>) were examined between day 11 and 18 following initial injections and grouped together with the mice imaged at pre-disease (n=2). One control mouse died during the first imaging session and two mice died following the first imaging session (n=1 control, n=1 A1AR<sup>-/-</sup>). One A1AR<sup>+/-</sup> and two A1AR<sup>+/+</sup> mice did not develop signs of disease and were not examined during the time frame in which disease signs usually began. All groups of mice including A1AR<sup>+/+</sup> (n=3), A1AR<sup>+/-</sup> (n=4), A1AR<sup>-/-</sup> (n=5), controls (n=4 C57Bl/6, n=1 A1AR<sup>+/+</sup>, n=2 A1AR<sup>-/-</sup>), and inoculated mice showing no sign of disease (n=2 A1AR<sup>+/+</sup>, n=1 A1AR<sup>+/-</sup>) underwent a second imaging session at remission between day 30 and 33 post-inoculation. However, one of the A1AR<sup>+/-</sup> mice included in this group was imaged at day 27 upon reaching endpoint. One A1AR<sup>-/-</sup> mouse reached endpoint of disease at day 20 and was sacrificed, and therefore was not included in the second imaging session.

A1AR<sup>-/-</sup> and A1AR<sup>+/-</sup> mice were found to have a trend towards more persistent disease than A1AR<sup>+/+</sup> mice; however, no significant differences in maximum score, disease burden, or day of disease onset were present. In general the A1AR<sup>+/+</sup> mice had a more complete recovery at day 30 post-inoculation (Figure 7.1). Only one A1AR<sup>-/-</sup>

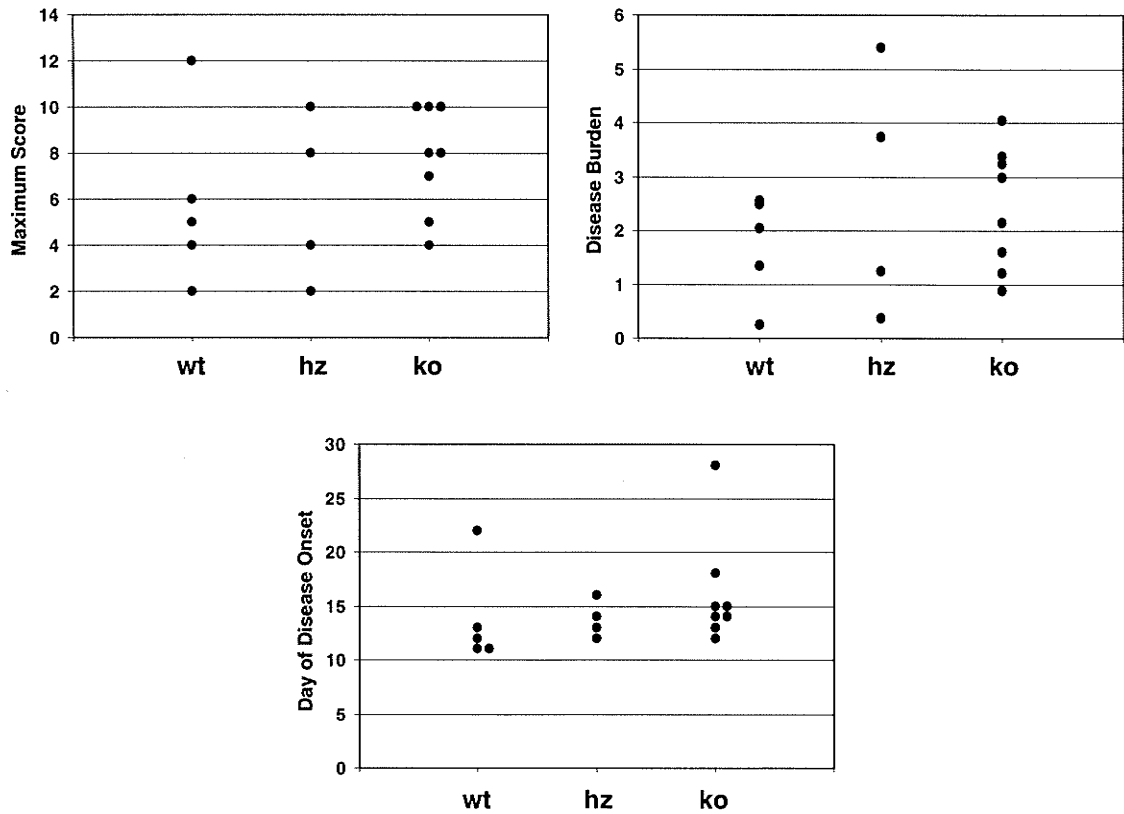
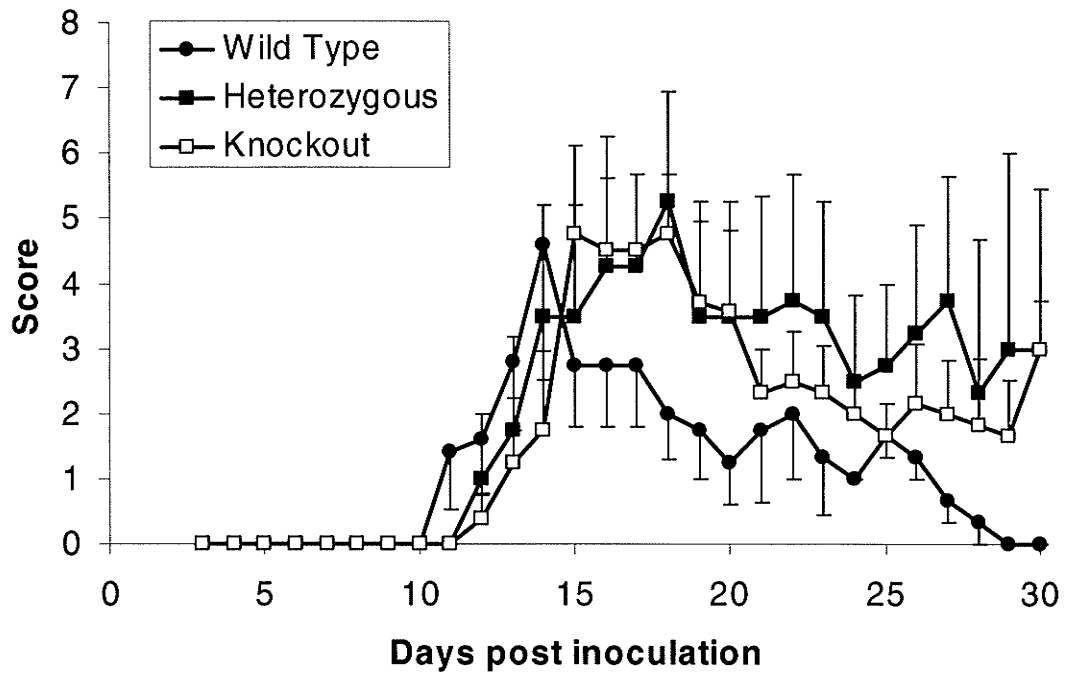


**Figure 7.1** Average scores of A1AR<sup>+/+</sup> (wt), A1AR<sup>+/-</sup> (hz) and A1AR<sup>-/-</sup> (ko) mice during the progression of EAE and calculations of maximum score, disease burden and day of disease onset for each animal. Error bars represent SEM.

mouse that reached day 30 to 33 had a full recovery back to a score of zero, while the three wild type mice all had a full recovery with a score of zero. Two of the four heterozygous mice at the second imaging session had a complete recovery. There were no differences in the drop in weight between the three groups of mice during the time course of the experiment (Figure 7.2).

### *7.3.2 Contrast Enhancement*

It was previously demonstrated in chapter 5 that contrast enhancement in the spinal cord of this EAE model was maximal at the beginning of disease signs. In this study T<sub>1</sub>-weighted contrast-enhanced imaging was performed at the onset of signs in each group of animals. MR images that were obtained from control mice examined between day 11 and 18 post-inoculation did not show any contrast enhancement within the imaged region of the lumbar spinal cord (Figure 7.3A). At the first sign of disease, a significant increase in enhancement on the calculated MR images of the spinal cord was observed in all groups of inoculated mice with EAE relative to control animals ( $p < 0.001$ ), but there were no significant differences between A1AR<sup>+/+</sup>, A1AR<sup>+/-</sup>, or A1AR<sup>-/-</sup> mice (Figures 7.3B,C,D and 7.4). Contrast-enhanced MR images obtained at day 30 to 33 post-inoculation did not show any enhancement in the spinal cord of control mice and there was reduced enhancement in the spinal cords in all other groups relative to the enhancement found at the onset of disease signs (Figure 7.3E,F,G). Contrast-enhanced MR images acquired during this second imaging session showed a significant increase in the % intensity in A1AR<sup>+/+</sup> ( $p < 0.05$ ), A1AR<sup>+/-</sup> ( $p < 0.05$ ) and A1AR<sup>-/-</sup> ( $p < 0.005$ ) mice compared to the control group (Figure 7.4).

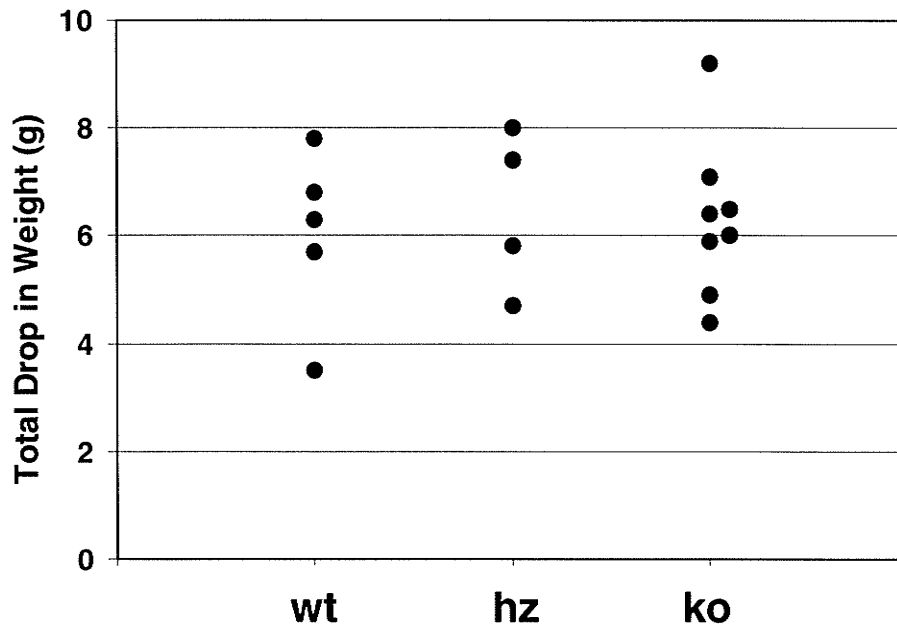
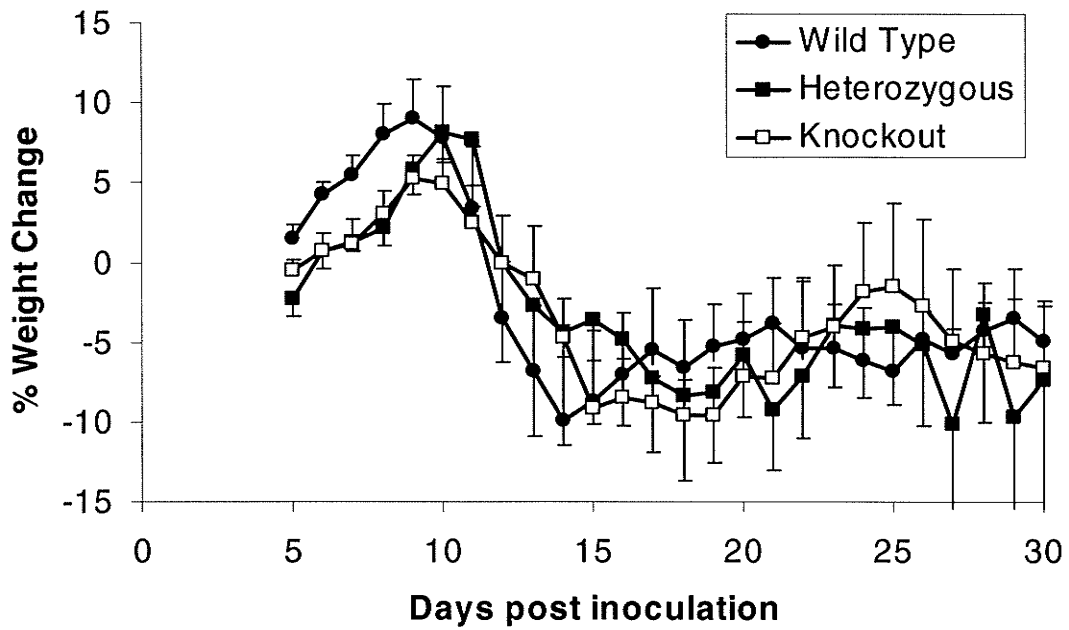


**Figure 7.2** Average weight changes of  $A1AR^{+/+}$ (wt),  $A1AR^{+/-}$  (hz) and  $A1AR^{-/-}$  (ko) mice during the progression of EAE and the calculation of total drop in weight for each animal. Error bars represent SEM.

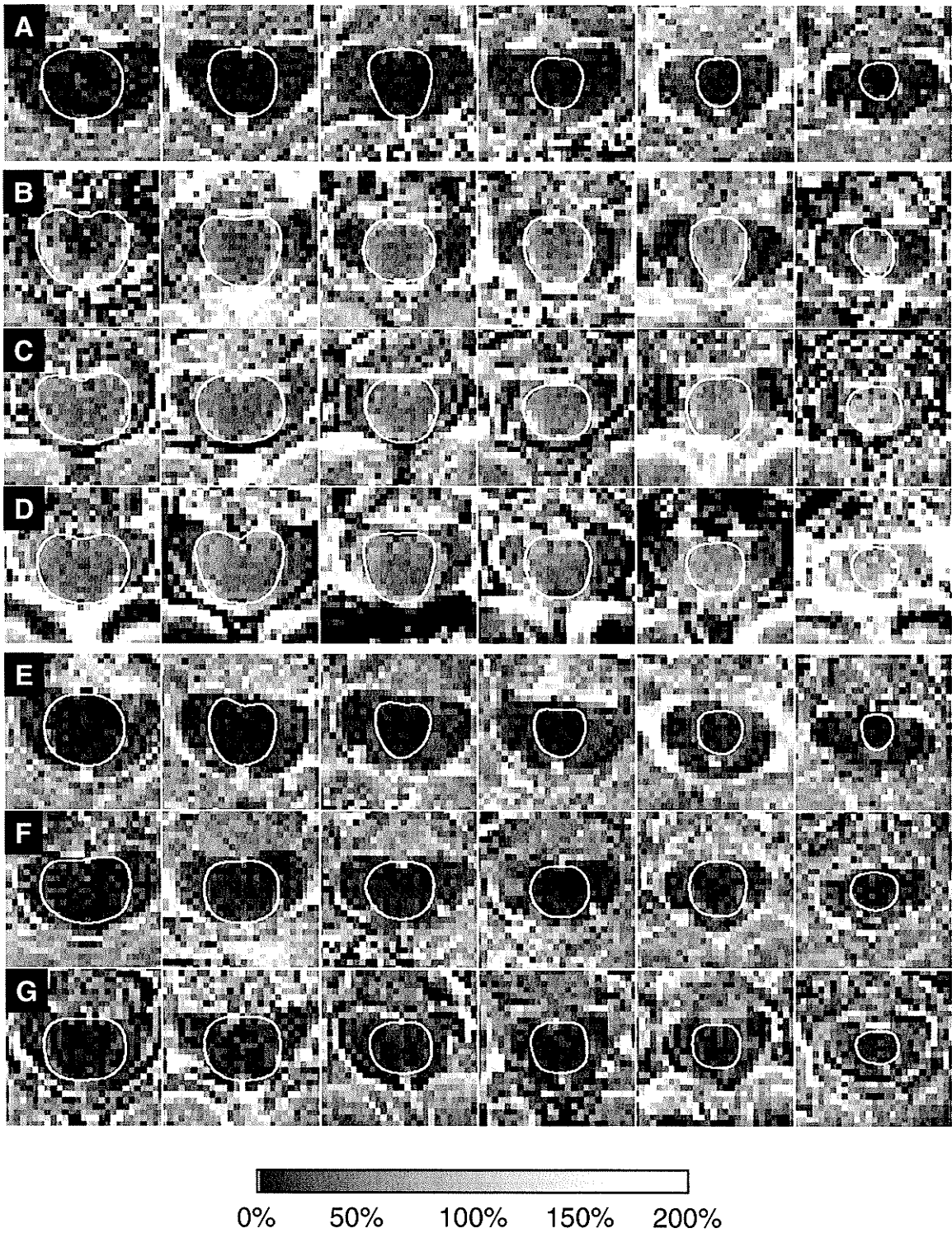


**Figure 7.3.** Representative sets of calculated contrast-enhanced images for (A) a control mouse, (B)  $A1AR^{+/+}$ , (C)  $A1AR^{+/-}$ , and (D)  $A1AR^{-/-}$  mouse at the initial stage of disease, and (E)  $A1AR^{+/+}$ , (F)  $A1AR^{+/-}$ , and (G)  $A1AR^{-/-}$  mouse at remission.

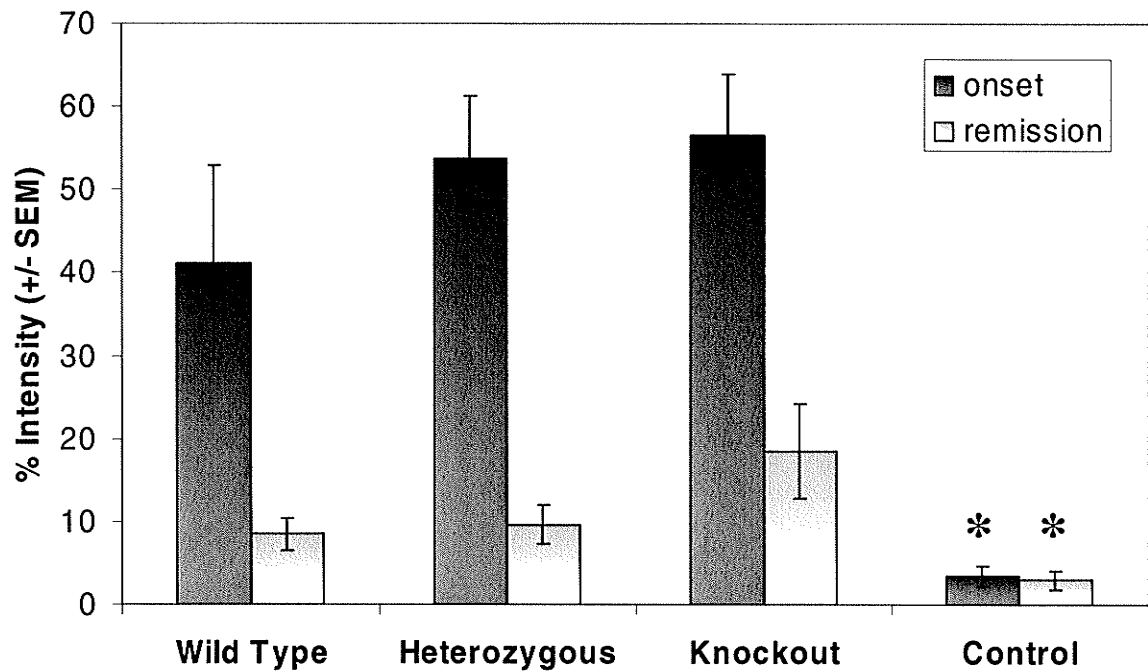


**Figure 7.4.** The average percent intensity for the entire set of slices in each group of animals at onset and remission stages of disease. \* differs significantly from all other groups at the corresponding time point.

### 7.3.3 Spinal Cord Volume

Previous MRI pilot experiments using mice with EAE indicated that the spinal cord becomes swollen at the initial onset of disease signs compared to pre-disease, followed by a decrease in spinal cord volume from the initial onset of disease signs to remission. In this experiment, MR images of the spinal cord were obtained pre-disease for only two mice and the MR images showed an increase in cord volume from pre-disease to the initial onset of signs of EAE (Figure 7.5). The percent change in spinal cord volume from the imaging session at disease onset to the second imaging session at disease remission was calculated in A1AR<sup>+/+</sup> (n=3), A1AR<sup>+/-</sup> (n=4), A1AR<sup>-/-</sup> (n=6), and control mice (n=8). The spinal cord volume data obtained from MR images acquired at the initial stages of disease and day 30 post-inoculation appears to indicate that the spinal cords of the knockout mice do not recover from swollen state as much as the spinal cords of wild type mice (Figure 7.6A), but differences in the reduction of spinal cord volume were not statistically significant. Comparing the A1AR<sup>+/-</sup> (n=2) and A1AR<sup>-/-</sup> (n=5) mice that continue to show signs of disease (incomplete recovery) at day 30 post-inoculation to the A1AR<sup>+/+</sup> (n=3), A1AR<sup>+/-</sup> (n=2), A1AR<sup>-/-</sup> (n=1) mice that had a full recovery at day 30 indicates that spinal cords of mice with persisting disease signs remained more swollen (Figure 7.6B; p<0.05).

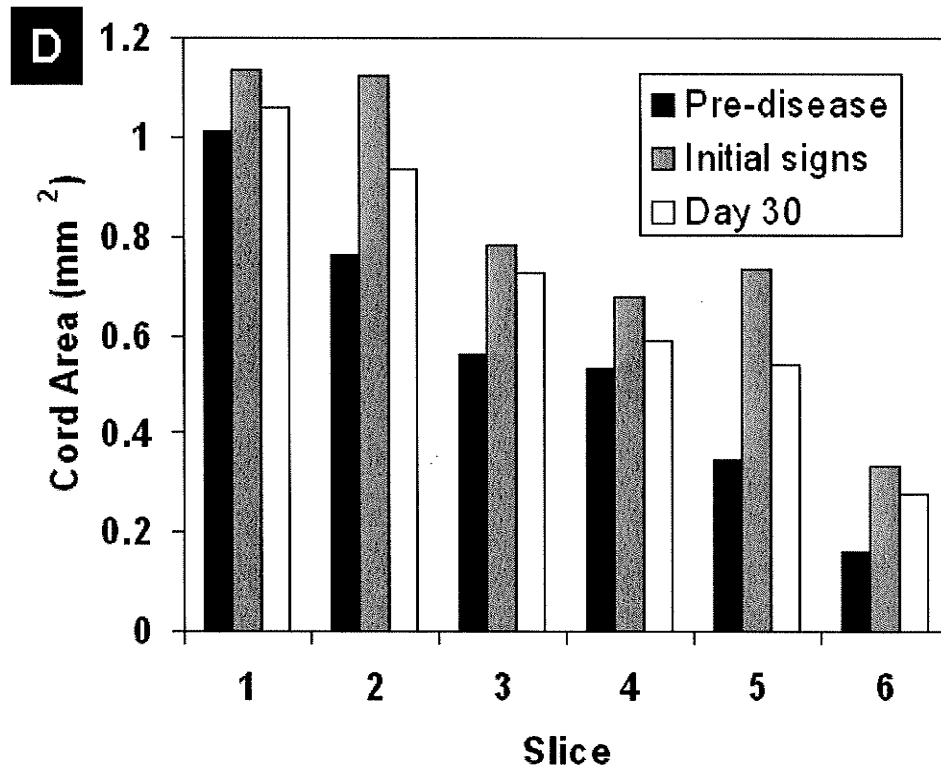
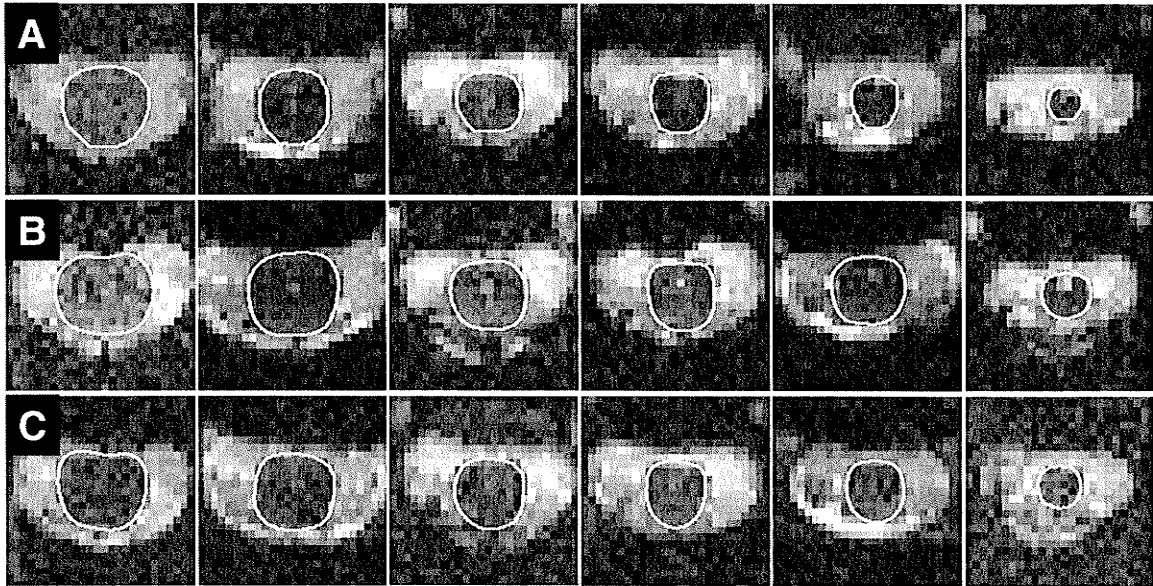


**Figure 7.5.** Complete sets of T<sub>2</sub>-weighted images from the same A1AR<sup>+/+</sup> mouse that was imaged at (A) pre-disease, (B) early stage of disease and (C) day 30. The spinal cord is outlined in each image. (D) The corresponding area of the spinal cord in each slice from this mouse was quantified at each time point.

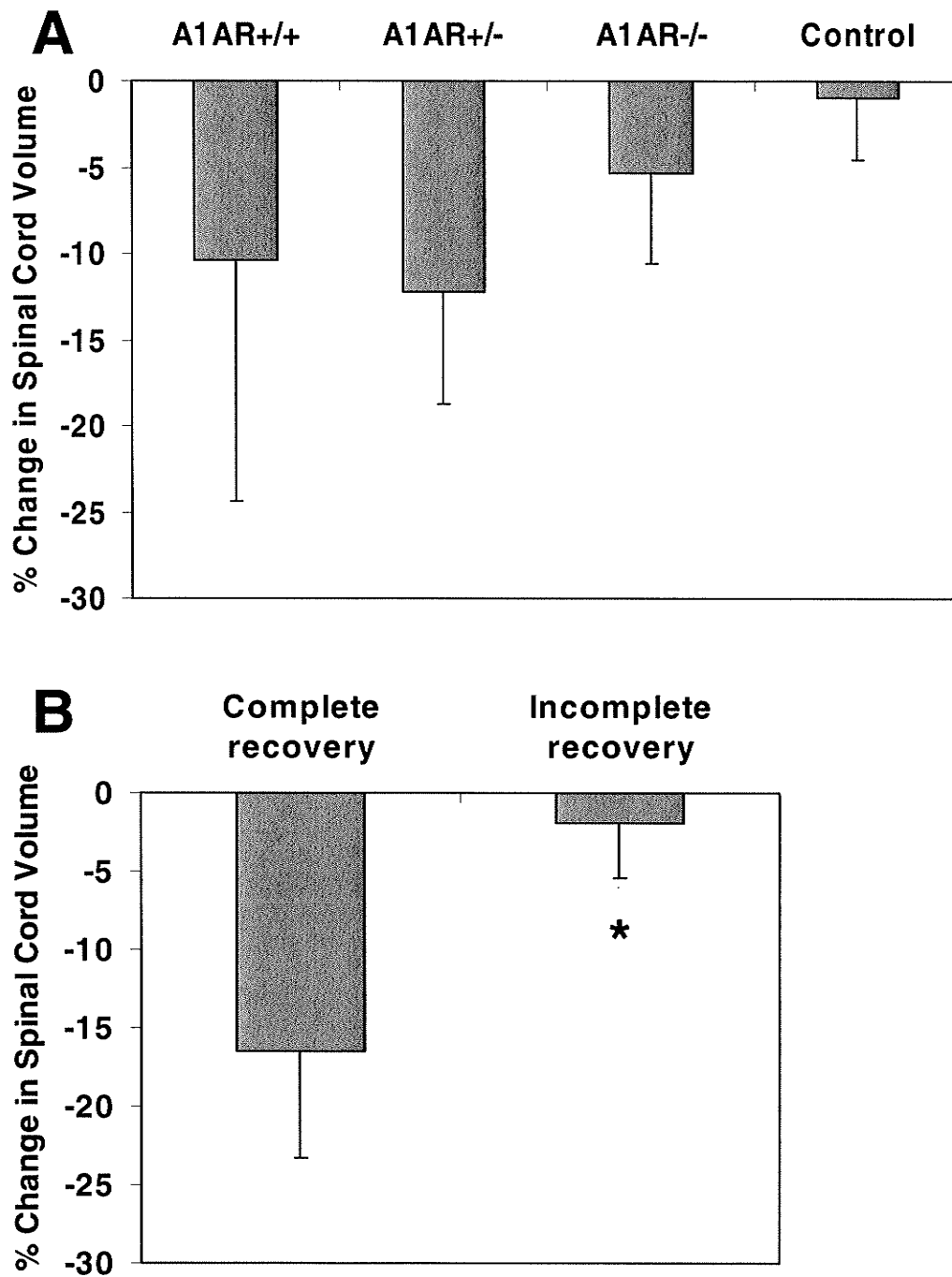


**Figure 7.6.** (A) The average change in spinal cord volume calculated across all 11 T<sub>2</sub>-weighted images from initial onset of signs to remission for each group of mice and (B) grouped according to complete versus incomplete recovery at the remission imaging session.

## 7.4 DISCUSSION

Activation of the A1AR is known to have anti-inflammatory effects *in vivo* as previous studies have demonstrated.<sup>111,150,153</sup> However, it is unknown whether the activation of the A1AR contributes to improved BSB stability. This study used T<sub>1</sub>-weighted contrast-enhanced imaging to determine the relative BSB permeability in A1AR<sup>+/+</sup>, A1AR<sup>+/-</sup>, and A1AR<sup>-/-</sup> mice induced with EAE.

No significant differences were found in the intensity of enhancement within the spinal cords on contrast-enhanced T<sub>1</sub>-weighted images of A1AR<sup>+/+</sup>, A1AR<sup>+/-</sup> and A1AR<sup>-/-</sup> mice at onset and remission stages of disease. These observations suggest that either the A1AR did not have a significant effect on the stability of the BSB during disease progression in this model of EAE or too much variability was introduced into the study.

MR imaging at the onset of disease signs took place anywhere from a few hours up to 24 hours after signs of disease actually first began, since mice were scored only once daily. It is possible that the state of BSB permeability is changing during the initial development of disease signs, and since imaging sessions occurred only upon first detection of a significant weight loss with tail weakness or paralysis, the imaging session may have occurred at the point where the disruption of the BSB was not yet at maximum or past the point of maximum disruption in some cases. These factors may have introduced some variability in the study and therefore increased the chance for type II error to occur.

The age of the mice upon induction of EAE ranged from 4 to 8 months, due to the lack of enough available mice caused by breeding difficulties. In a study comparing disease progression in young versus middle-aged Wistar rats with EAE, differences were found in the time of disease onset and severity.<sup>162</sup> Young Wistar rats (7 weeks) showed more severe signs of disease than the older rats (15 months), but the disease completely resolved. The group of older rats showed a delay in the onset of disease signs.<sup>162</sup> Smith et al also demonstrated an age effect on the expression of signs of EAE in SJL mice.<sup>163</sup> SJL mice that were younger (less than 6 weeks) at the time of disease induction were found to have delays in the development of observable signs of disease, but by 6-7 weeks the disease had an earlier onset and more rapid progression.<sup>163</sup> Since disease severity may similarly have been affected by the age of the mouse in this study, this was another cause of variability.

The volume of the imaged region of the lumbar spinal cord was determined from the T<sub>2</sub>-weighted images. A significant difference was observed between changes in spinal cord volume between imaging sessions in mice that had a full functional recovery versus mice that had residual signs of disease at the time of second imaging. Mice that underwent a complete recovery had a significantly greater recovery in spinal cord volume at the time of second imaging, suggesting that spinal cord volume measurements can reliably detect changes between mice with unresolved signs of disease and mice that have undergone a full recovery. No significant differences in changes in spinal cord volume between A1AR<sup>+/+</sup>, A1AR<sup>+/-</sup> and A1AR<sup>-/-</sup> mice were found, though there was a trend showing that the spinal cord of A1AR<sup>-/-</sup> mice remained in a more swollen state at the second imaging session.

## **CHAPTER VIII**

### **EFFECTS OF SPHINGOSINE 1-PHOSPHATE IN MICE WITH EXPERIMENTAL AUTOIMMUNE ENCEPHALOMYELITIS**

## 8.1 INTRODUCTION

Sphingosine is an endogenous lysolipid that can be phosphorylated by sphingosine kinase 1 to form sphingosine 1-phosphate (S1P), which is released into the circulation by activated platelets. There are five S1P receptors (S1P<sub>1-5</sub>), formerly known as endothelial differentiation gene (Edg) receptors (Edg-1, Edg-5, Edg-3, Edg-6, and Edg-8 respectively), that are expressed on the endothelium and lymphocytes.<sup>164</sup>

S1P has been shown to promote angiogenesis and chemotaxis, decrease vascular leak and edema formation, rearrange the actin cytoskeleton within endothelial cells, promote adherens junction assembly, inhibit apoptosis, increase lymphocyte homing, and decrease the number of lymphocytes in peripheral blood.<sup>164-167</sup> Previous work has shown that lymphocytes require the S1P<sub>1</sub> receptor and S1P gradients to exit the thymus and peripheral lymphoid tissue.<sup>168</sup>

2-amino-2-(2-[4-octylphenyl]ethyl)-1,3-propanediol hydrochloride (FTY720) is a newly developed immunosuppressant and synthetic analog of sphingosine that is currently being used in human kidney transplantation. FTY720 is produced through the chemical modification of myriocin, a metabolite of the fungus *Isaria sinclairii*.<sup>169</sup> The phosphorylated form of FTY720 (FTY720-P) is an agonist at four S1P receptors (S1P<sub>1</sub>, S1P<sub>3</sub>, S1P<sub>4</sub>, S1P<sub>5</sub>).<sup>164,170</sup> FTY720 does not inhibit T cell activation or proliferation and acts analogous to S1P by sequestering T cells in peripheral lymph nodes.<sup>171,172</sup>

The actions of S1P and the S1P receptor agonist FTY720 may be potentially useful in reducing the autoimmune inflammatory attack on myelin within the CNS in patients with MS. The administration of S1P or FTY720 during a period of remission

in patients with relapsing-remitting MS could potentially sequester autoimmune CD4<sup>+</sup> T cells in secondary lymphoid tissue. The additional role of S1P in enhancing endothelial barrier properties may be effective in decreasing disease progression in MS as BBB disruption is a critical early event in active lesion formation. Clinical trials are currently underway using the S1P receptor agonist FTY720 in patients with relapsing-remitting MS with promising results.<sup>173</sup>

The objective of this study was to determine the effect of S1P on functional deficit, BBB permeability, inflammation, and demyelination in a monophasic EAE model in C57Bl/6 mice using contrast-enhanced T<sub>1</sub>-weighted and MT-weighted MR imaging.

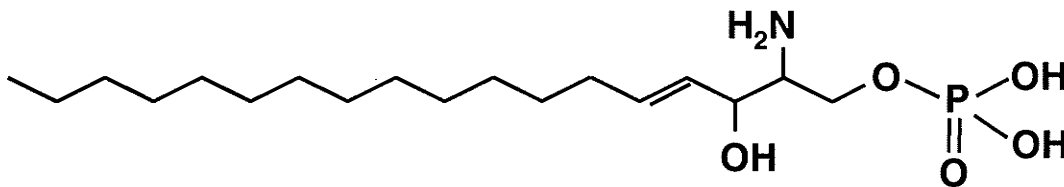


**Figure 8.1.** The molecular structure of S1P.

## 8.2 METHODS

### 8.2.1 *Induction of EAE and Scoring System*

EAE was induced in 61 female C57Bl/6 mice (Genetics Model Centre, University of Manitoba) 11 weeks old as described in chapter 3. Weight and disease severity was measured daily using the scoring system outlined in chapter 3.

### 8.2.2 *S1P Administration*

The treatment groups received daily intravenous injections of S1P (Sigma-Aldrich, Saint Louis, MO) dissolved in 0.3% bovine serum albumin (BSA; fatty acid free, low endotoxin; Sigma-Aldrich, Saint Louis, MO) beginning either at day 7 post-inoculation (before signs of disease) or at the onset of EAE as outlined in Table 8.1. The S1P stock solution (0.5 mM or 0.19 mg/mL in 0.3% BSA) was used for mice receiving the 0.5mg/kg dose and diluted to 0.1mM or 0.01mM using 0.3% BSA for 0.1mg/kg or 0.01mg/kg doses respectively. S1P was injected into the tail vein of each mouse with volumes typically in the range of 0.05 - 0.06 mL using a 30 gauge needle while the mouse is under brief anesthetic (isoflurane). The equivalent volume of 0.3% BSA was injected into control mice.

### 8.2.3 *MR Imaging*

T<sub>2</sub>- and MT-weighted images of the lumbar spinal cord were acquired using a quadrature volume coil. MT-weighted imaging requires a uniform calibrated B<sub>1</sub> field, which was much easier to achieve using a volume coil. This was followed by

acquisition of pre- and post-contrast-enhanced T<sub>1</sub>-weighted MR images using a quadrature surface coil using the parameters given in chapter 3. A single set of slices was obtained at the level of the lumbar spinal cord as described in chapter 3 and slice positions shown in Figure 3.3C,D. Groups of mice were examined with MRI at pre-disease, initial signs of disease, peak disease, and remission as outlined in Table 8.1. The mice that received daily dosing of S1P or BSA beginning at the onset of disease signs were examined at the first indication of disease signs, followed by the injection of S1P or BSA and another imaging session 6 hours after the administration of S1P or BSA. MT-weighted MR imaging was not performed at the onset of disease signs for mice that were imaged again 6 hours after S1P or BSA injection to reduce imaging time and stress on the animals.

**Table 8.1.** S1P/BSA treatment groups and imaging protocol.

<b>Number of mice</b>	<b>S1P dose</b>	<b>Time daily dosing began</b>	<b>Imaging times</b>
5	0.01mg/kg	Day 7 (Pre-disease)	T <sub>2</sub> w, T <sub>1</sub> w, MTw: pre-disease, onset signs, peak disease, remission
5	0.1mg/kg		
5	0.5mg/kg		
3	0.3% BSA		T <sub>2</sub> w, T <sub>1</sub> w: pre-disease, onset signs, peak disease, remission
6	0.1mg/kg		
4	0.3% BSA		
5	0.01mg/kg	Onset of signs	T <sub>2</sub> w, T <sub>1</sub> w, MTw: pre-disease, peak disease, remission T <sub>2</sub> w, T <sub>1</sub> w: onset signs & 6hr
6	0.1mg/kg		
5	0.5mg/kg		
9	0.3% BSA		T <sub>2</sub> w, T <sub>1</sub> w: pre-disease, onset signs & 6hr, peak disease, remission
5	0.1mg/kg		
3	0.3% BSA		

#### *8.2.4 MR Image Analysis*

The spinal cord was outlined on T<sub>2</sub>-weighted images as described in chapter 3 and these ROIs were superimposed onto MT-weighted images that were acquired with a saturation pulse. The regions of grey and white matter within the defined area of the spinal cord were outlined on MT-weighted images as described in chapter 3 and shown in Figure 3.6. The ROIs outlining separately the grey and white matter within the spinal cord were superimposed onto MTR maps and percent difference images of contrast enhancement that were calculated using the formulae in chapter 3. The spinal cord volume across all 6 T<sub>2</sub>-weighted images obtained as a single set of images was calculated as the sum of each ROI area (mm<sup>2</sup>) x 0.95mm (slice thickness of 0.75mm + interslice gap of 0.2mm).

#### *8.2.5 Statistical Analysis*

Data from each group of animals were reported as mean ± SEM. Disability was analyzed in terms of maximum score, disease burden (the sum of scores divided by the number of days starting with day 8), and day of disease onset. The maximum and minimum weight that was reached for each mouse was determined during the disease state; the difference between these two weights was the calculated drop in weight. Parametric data (percent intensity, day of disease onset, drop in weight, and spinal cord volume) were compared statistically using ANOVA followed by post hoc t tests, whereas the Kruskal-Wallis test followed by Mann-Whitney post hoc test was used for non-parametric data (maximum score, disease burden). Statistical significance was considered to be at  $p < 0.05$ .

## 8.3 RESULTS

### 8.3.1 Behaviour Scores

Groups of mice were examined with MRI before signs of disease, at the first signs of disease, at maximum disease score, and at remission. Three mice that did not develop any signs of disease were removed from the analysis. These mice were originally designated to be in the treatment groups of 0.01mg/kg (n=2) and 0.5mg/kg (n=1) S1P dosing at the onset of disease signs. The mice that developed signs of disease generally followed a monophasic disease course, though some mice (n=12) underwent a second relapse (Figure 8.2).

The administration of S1P did not affect the time of disease onset (a disease score  $\geq 1$ ), which ranged from 10 - 17 days post-MOG injection in all mice that received BSA treatment (n=19; Figure 8.3). The day of onset (post-MOG injection) for groups of mice that received S1P treatment beginning at the onset of disease signs ranged from 14 - 15 days (0.01mg/kg S1P; n=3), 11 - 16 days (0.1mg/kg S1P; n=11), and 11 - 19 days (0.5mg/kg S1P; n=4) and for groups of mice that were administered S1P beginning at pre-disease on day 7, the day of onset ranged from 13 - 16 days (0.01mg/kg S1P; n=5), 12 - 17 days (0.1mg/kg S1P; n=11), and 12 - 18 days (0.5mg/kg S1P; n=5).

There were no differences in maximum score and disease burden between groups of mice that were injected daily with S1P or BSA starting at the onset of disease signs (Figure 8.3), whereas mice that received 0.5mg/kg S1P beginning at the earlier time point of day 7 showed a significantly lower maximum score when compared to

mice that received BSA ( $p < 0.05$ ; Figure 8.3). A trend of reduced disease burden was observed in mice that received 0.5mg/kg S1P (Figure 8.3), but this difference was not found to be statistically significant.

### *8.3.2 Changes in Weight*

A significant loss in weight was observed in all groups of mice that received either S1P or BSA (Figure 8.4), but there were no significant differences in weight loss between groups (Figure 8.5). Mice that were first administered S1P at the onset of disease signs showed a trend of increased weight gain before the onset of disease signs compared to mice that were administered S1P beginning at day 7 (Figure 8.4).

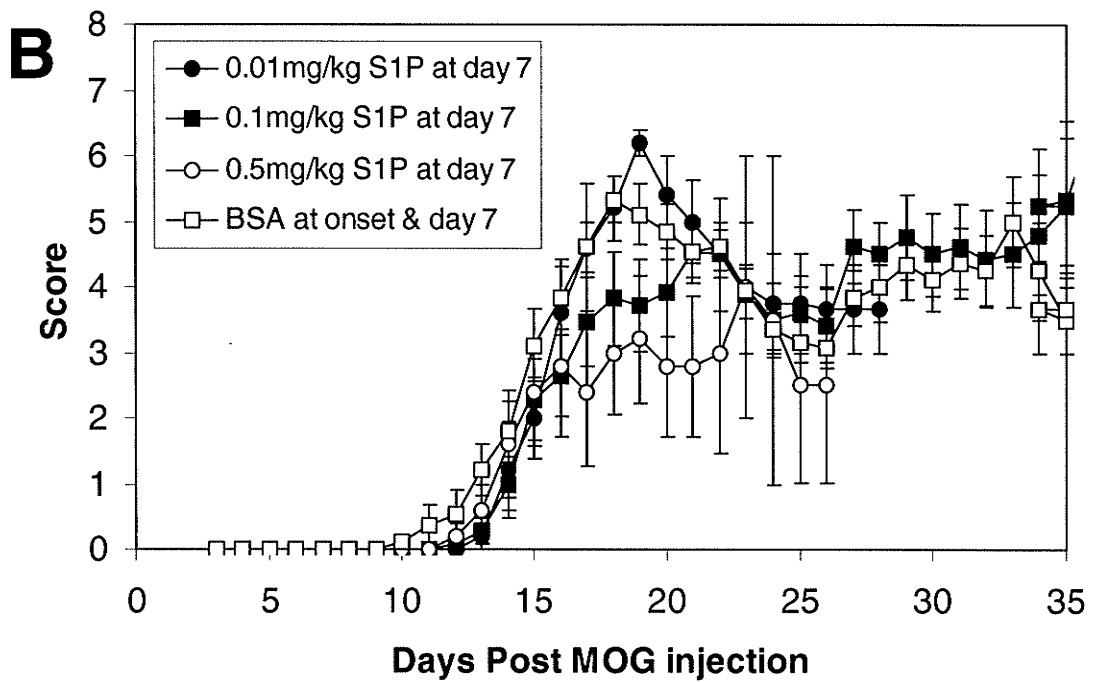
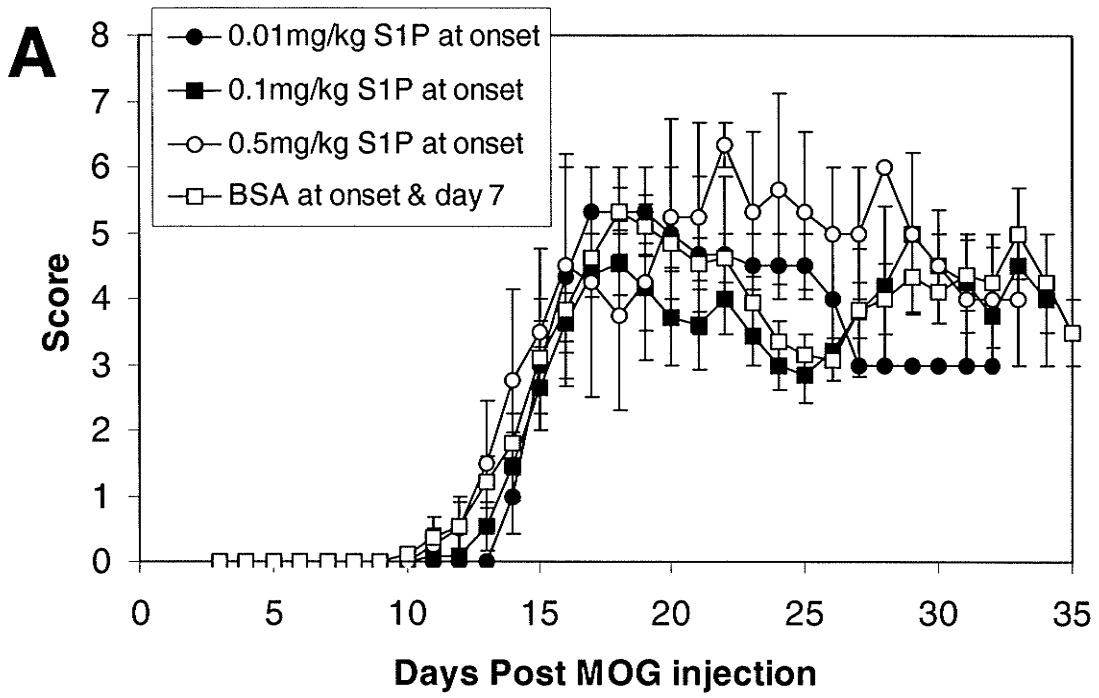


**Figure 8.2.** Average scores of mice during disease progression that received daily doses of 0.01mg/kg S1P, 0.1mg/kg S1P, 0.5mg/kg S1P or 0.3% BSA (A) beginning at the onset of disease signs and (B) at day 7 before signs of disease were first evident. Error bars represent SEM.

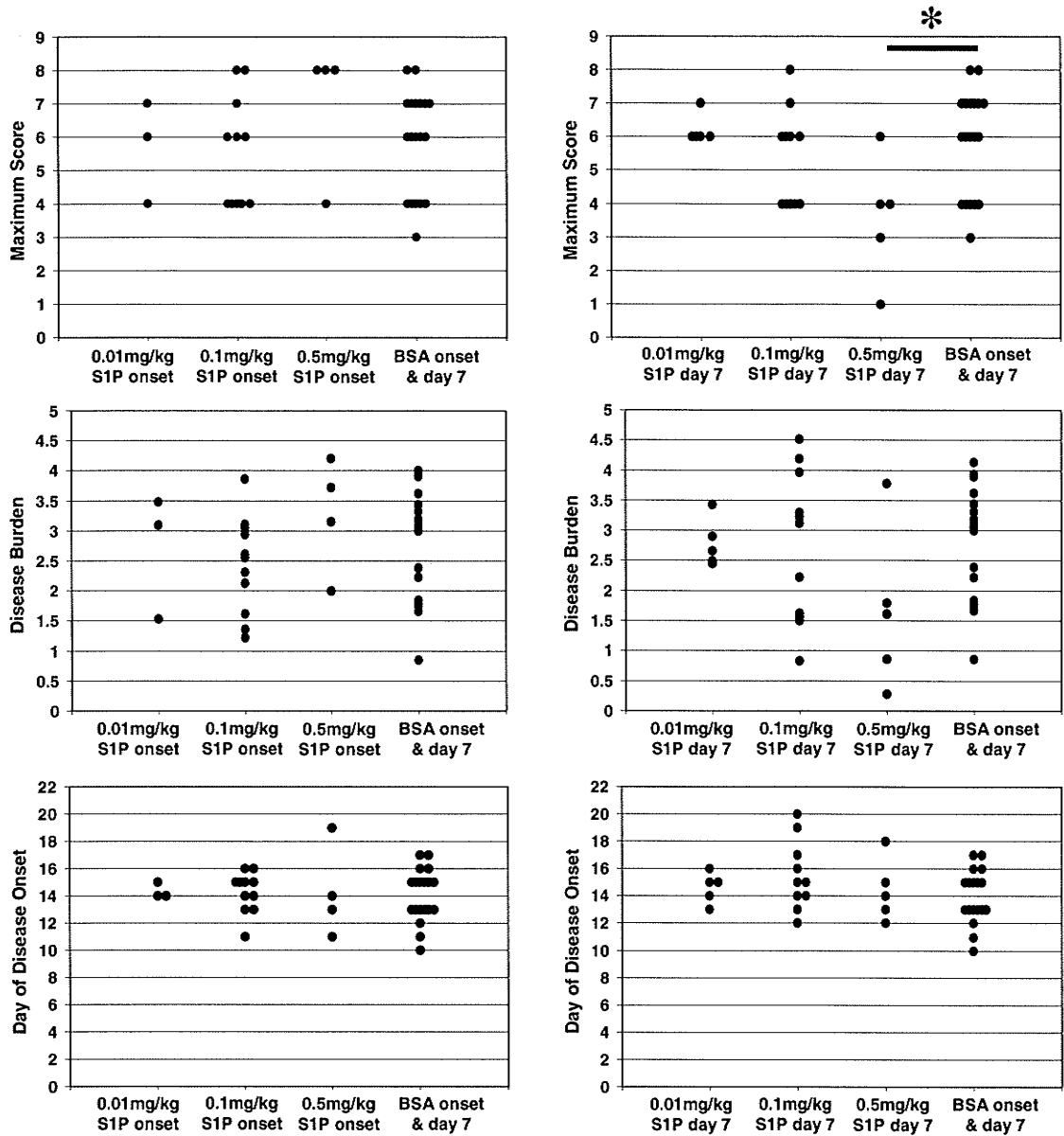


**Figure 8.3.** The maximum score, disease burden, and day of disease onset for each animal according to the S1P or BSA dosing regimen. The average maximum score for mice administered 0.5mg/kg S1P at day 7 was significantly lower ( $p < 0.05$ ) than mice administered BSA.

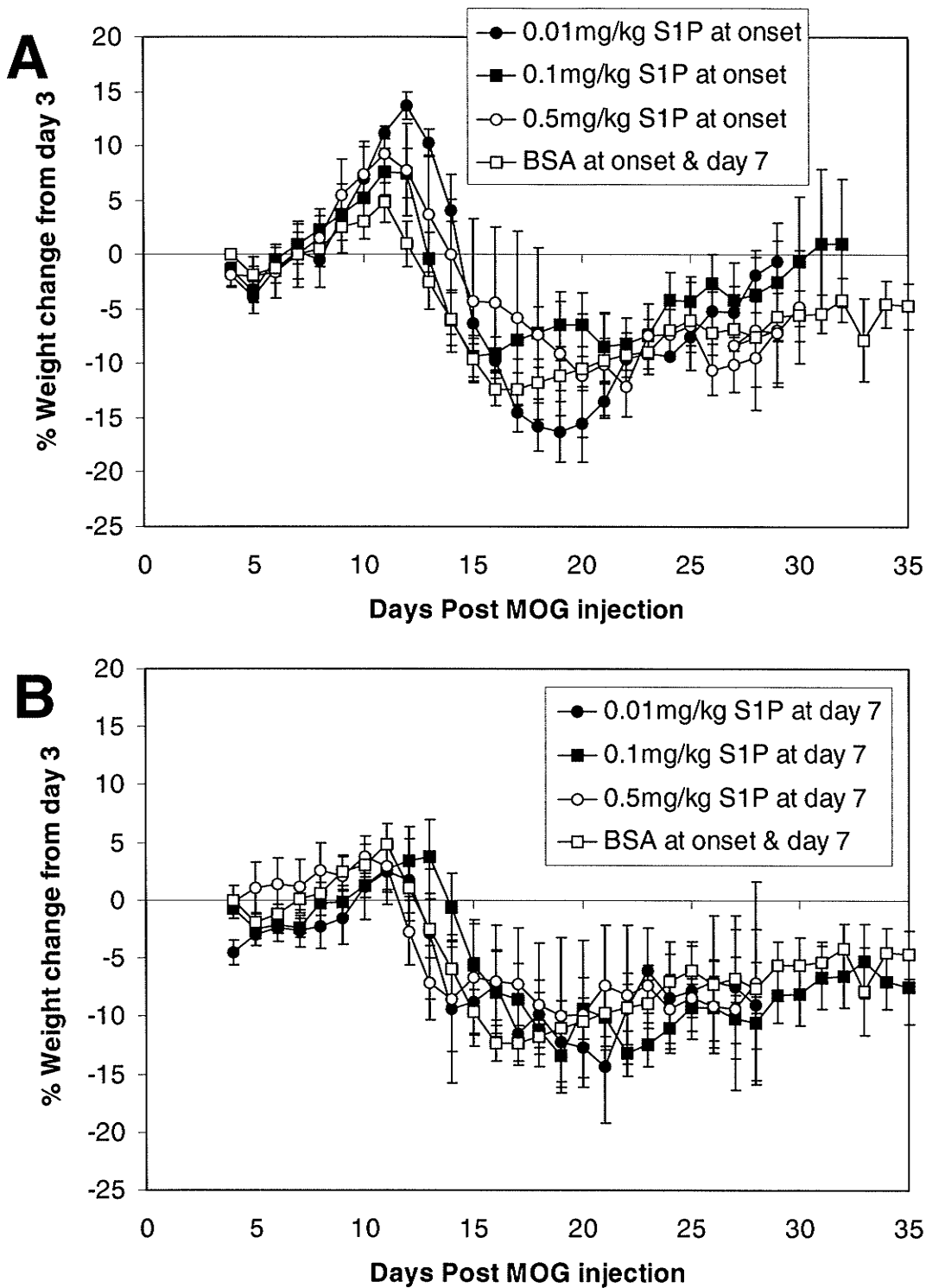


**Figure 8.4.** Average weight changes of mice during disease progression that received daily doses of 0.01mg/kg S1P, 0.1mg/kg S1P, 0.5mg/kg S1P or 0.3% BSA (A) beginning at the onset of disease signs and (B) at day 7 before signs of disease were first evident. Error bars represent SEM.

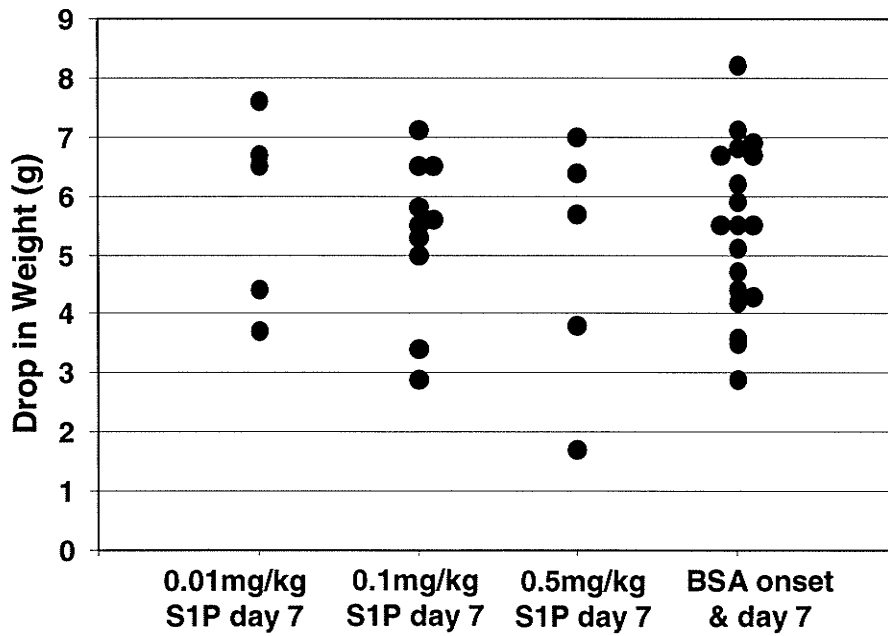
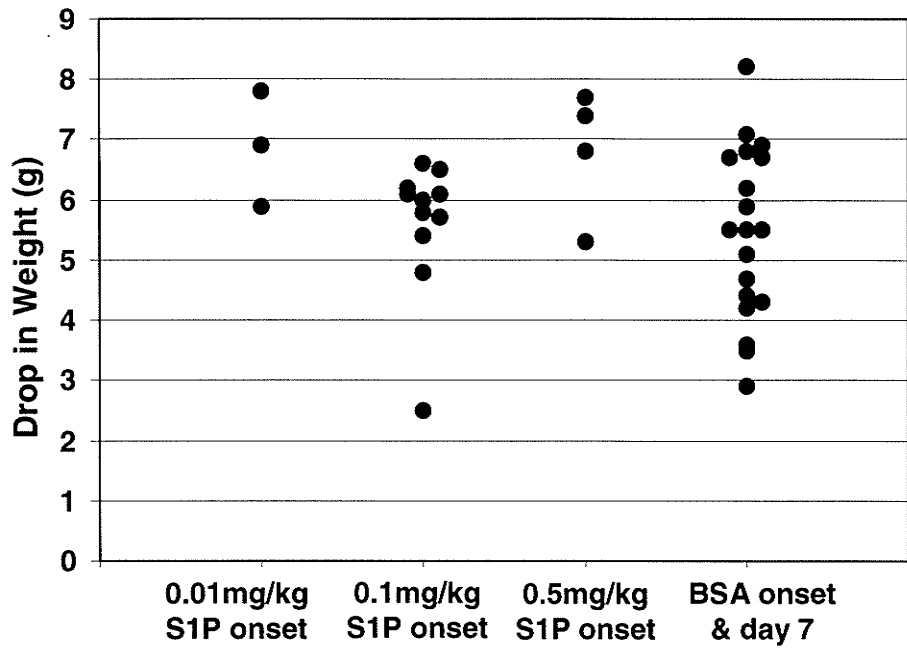


**Figure 8.5.** The drop in weight for each animal according to the S1P or BSA dosing regimen. No significant differences were present.

### 8.3.3 Contrast Enhancement

Calculated difference images of contrast enhancement were used to measure the intensity on MR images of the spinal cord at pre-disease, onset of signs of disease, peak disease, and remission. There was no significant contrast enhancement within the spinal cord at pre-disease in any of the mice examined (Figures 8.6A, 8.8), whereas the maximum contrast enhancement within the spinal cord occurred at the onset of signs of EAE (Figures 8.6B, 8.8). An important observation was that the pixels of highest intensity were located within the white matter of the spinal cord (Figure 8.7). At peak disease there was a decrease in contrast enhancement within the spinal cord in all groups of mice and the pixels of highest intensity were also located within the ROI outlining the white matter (Figures 8.6C, 8.8). The contrast enhancement was minimal within the spinal cord at remission (Figures 8.6D, 8.8).

The contrast enhancement within the spinal cord at pre-disease in all the mice examined was significantly lower than the contrast enhancement at all other time points of mice first receiving S1P or BSA at the onset of disease (at onset: all groups ( $p < 0.0001$ ), at peak disease: all groups ( $p < 0.0001$ ), at remission: 0.01mg/kg S1P ( $p < 0.0001$ ), 0.1mg/kg S1P ( $p < 0.05$ ), 0.5mg/kg S1P ( $p < 0.0005$ ), and BSA ( $p < 0.005$ )), and for dosing beginning at day 7 (at onset: all groups ( $p < 0.0001$ ), at peak disease: all groups ( $p < 0.0001$ ), and remission: 0.01mg/kg S1P ( $p < 0.0001$ ), 0.1mg/kg S1P, 0.5mg/kg S1P, and BSA ( $p < 0.005$ )). Mice that were first administered S1P or BSA at the onset of disease showed enhancement within the spinal cord at the onset of disease signs that was significantly greater than at all other time points (at peak disease: 0.01mg/kg S1P ( $p < 0.01$ ), 0.1mg/kg S1P ( $p < 0.0005$ ), 0.5mg/kg S1P ( $p < 0.01$ ), and BSA

(0.0001); at remission: 0.01mg/kg S1P ( $p < 0.005$ ), 0.1mg/kg S1P ( $p < 0.0001$ ), 0.5mg/kg S1P ( $p < 0.001$ ), and BSA( $p < 0.001$ ). No significant differences in contrast enhancement were found between treatment groups at onset of disease for mice that began treatment at day 7. The contrast enhancement for mice in all S1P treatment groups at peak disease and remission did not differ from the BSA control group at the corresponding time point.

Mice that received S1P or BSA beginning at the onset of signs of disease were examined with MRI before the administration of the first dose followed by a second examination 6 hours later. The change in the intensity of contrast enhancement was calculated for each treatment group (Figure 8.9). The group of mice receiving the 0.1mg/kg S1P was found to have a significant decrease in the average percent intensity ( $p < 0.05$ ) within the spinal cord after 6 hours compared to the BSA control group.

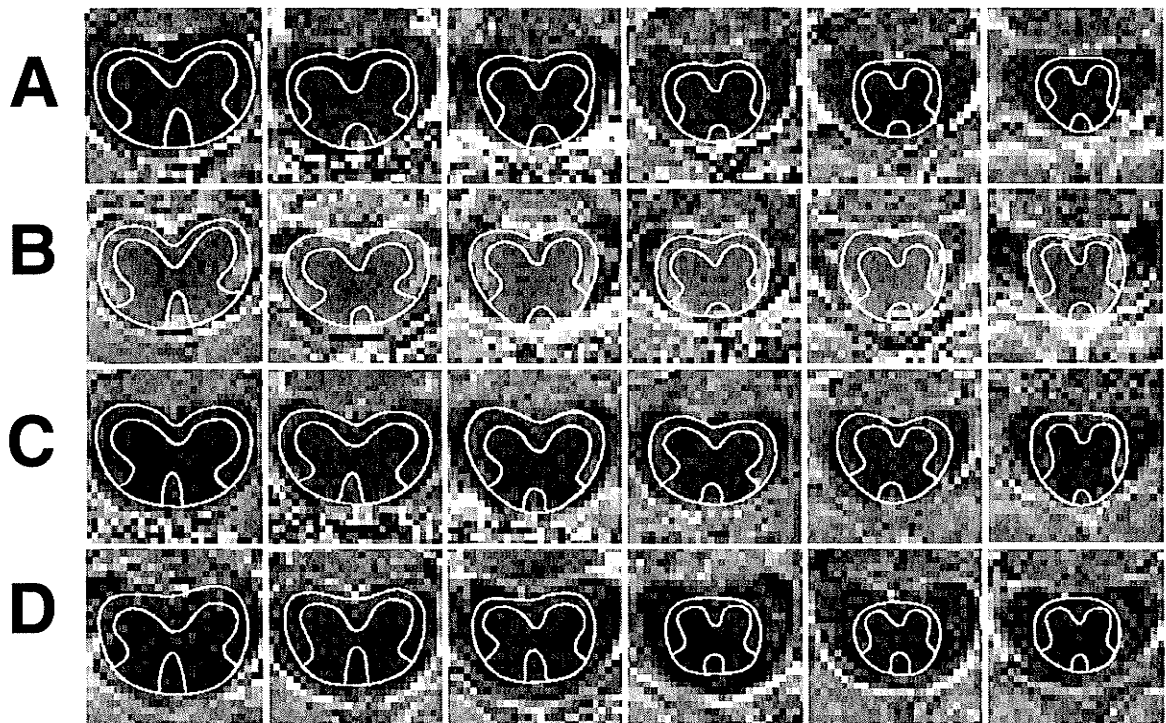


**Figure 8.6.** Representative sets of calculated contrast-enhanced images of the lumbar spinal cord with ROIs outlining the areas of grey and white matter of (A) a mouse before the onset of signs, (B) a mouse at the initial stages of disease, (C) a mouse at the peak of disease, and (D) a mouse in remission.

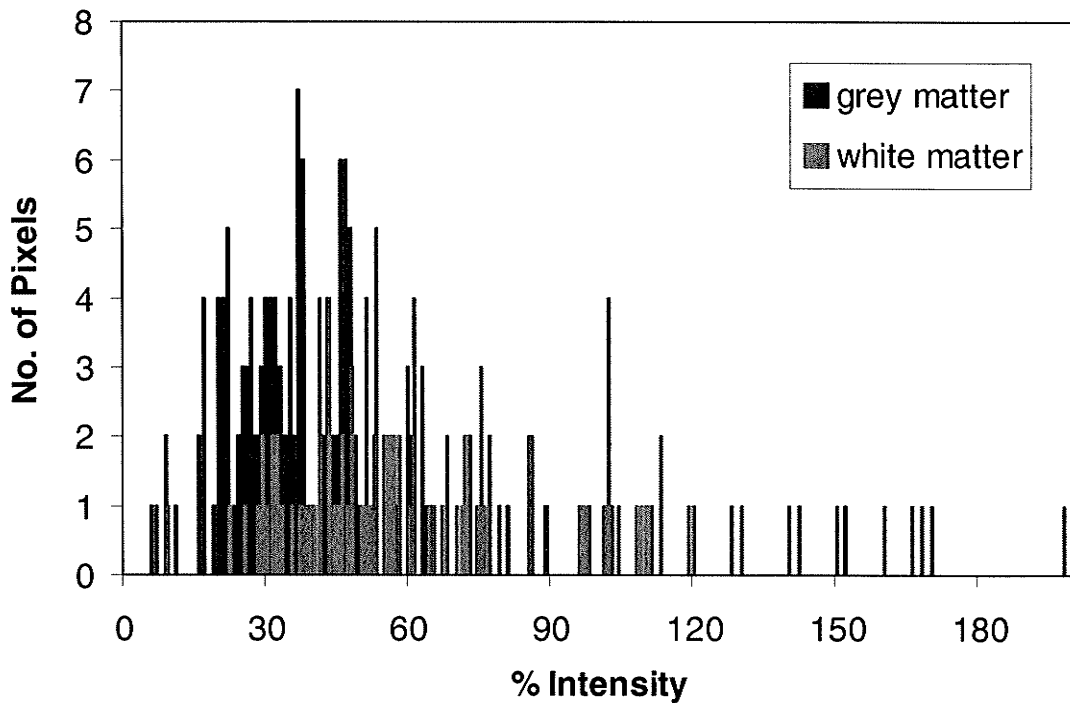
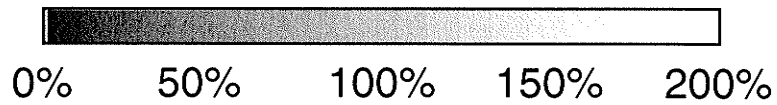
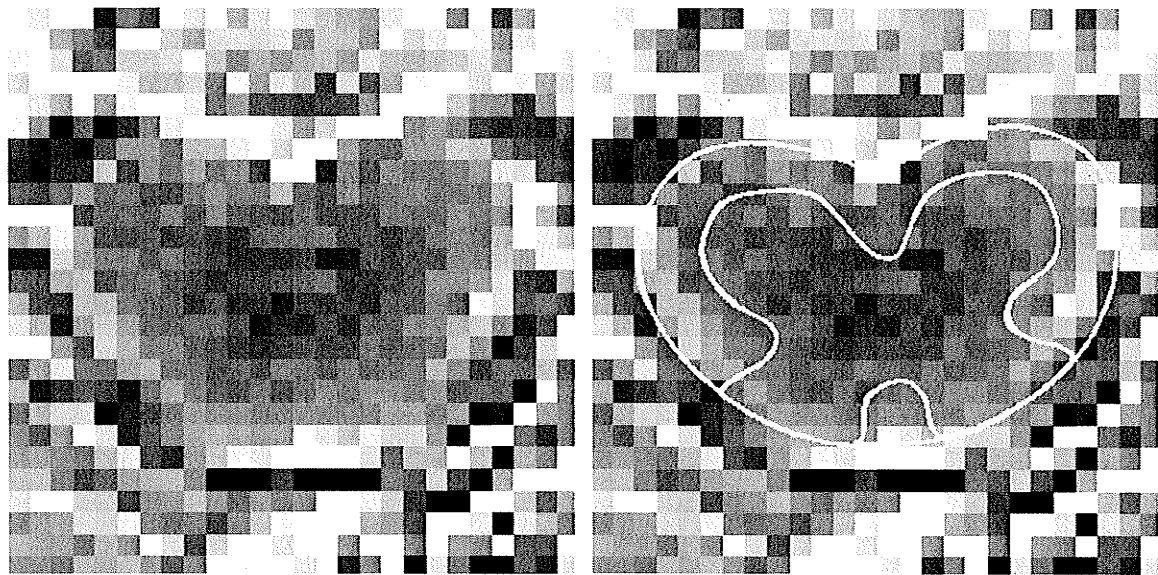


**Figure 8.7.** A representative calculated difference image of percent enhancement of the lumbar spinal cord (2.5mm×2.5mm) from a control mouse at the onset of disease signs indicating the regions of grey and white matter and the corresponding histogram.

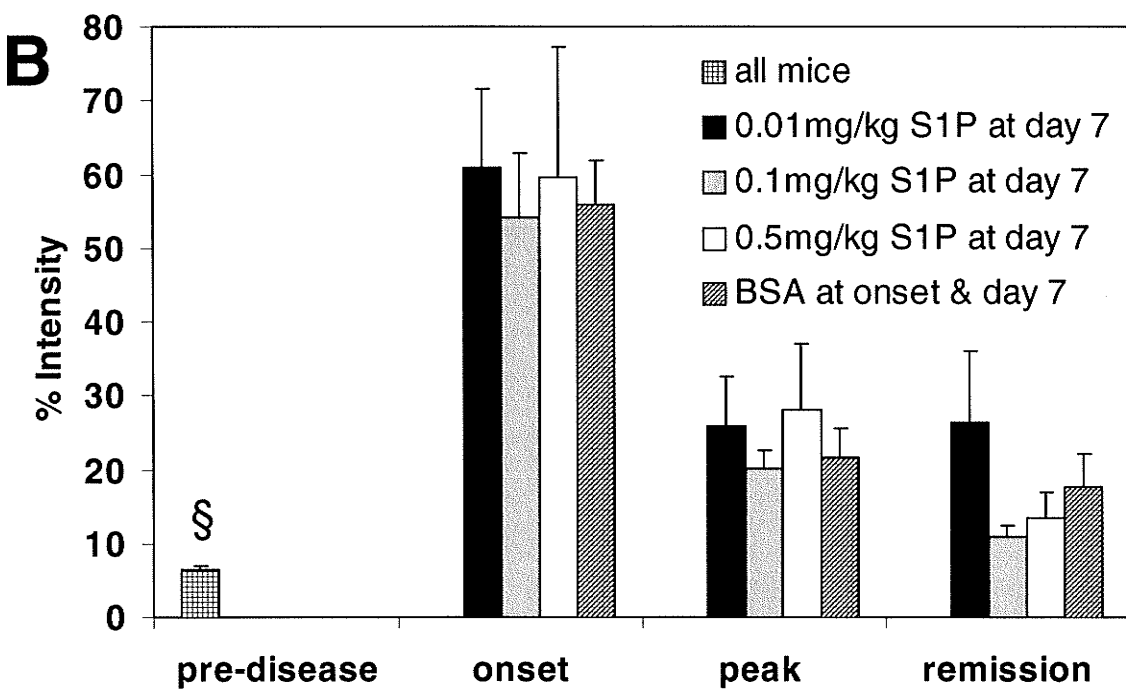
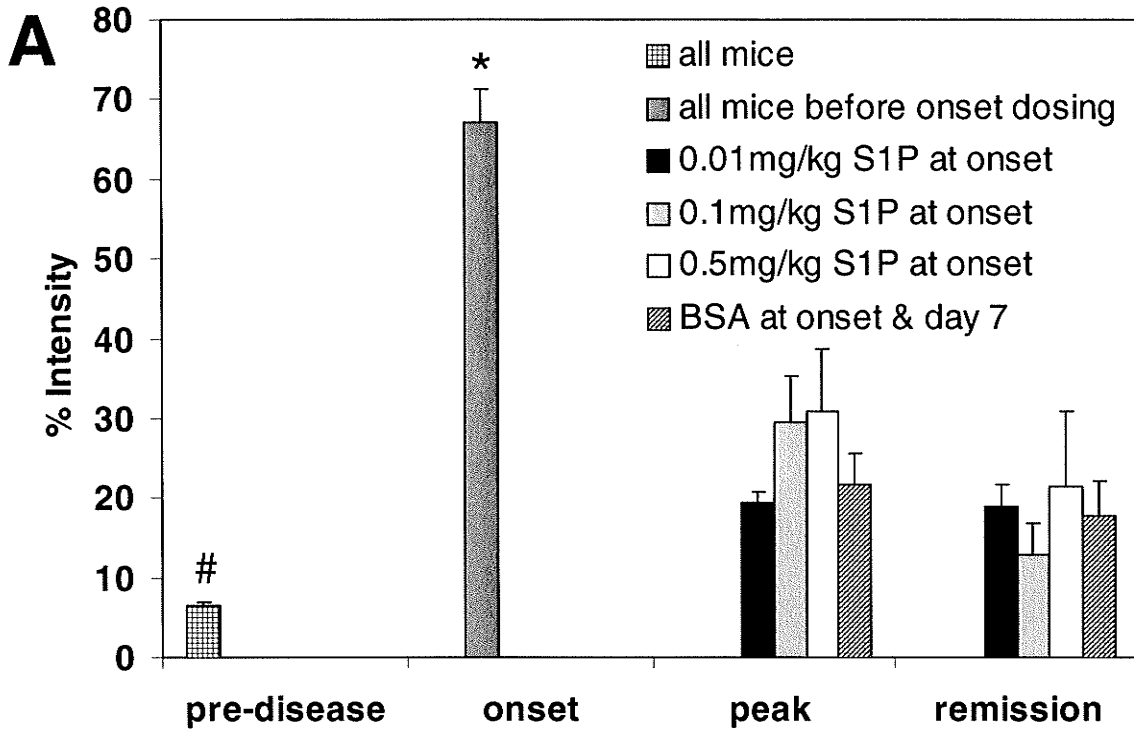


**Figure 8.8.** The average  $\pm$  SEM across the 6 slices examined in this study for the % intensity change in T<sub>1</sub>-weighted MR images of the lumbar spinal cord following Gd-DTPA administration. #, \*, and § differ from all other groups.

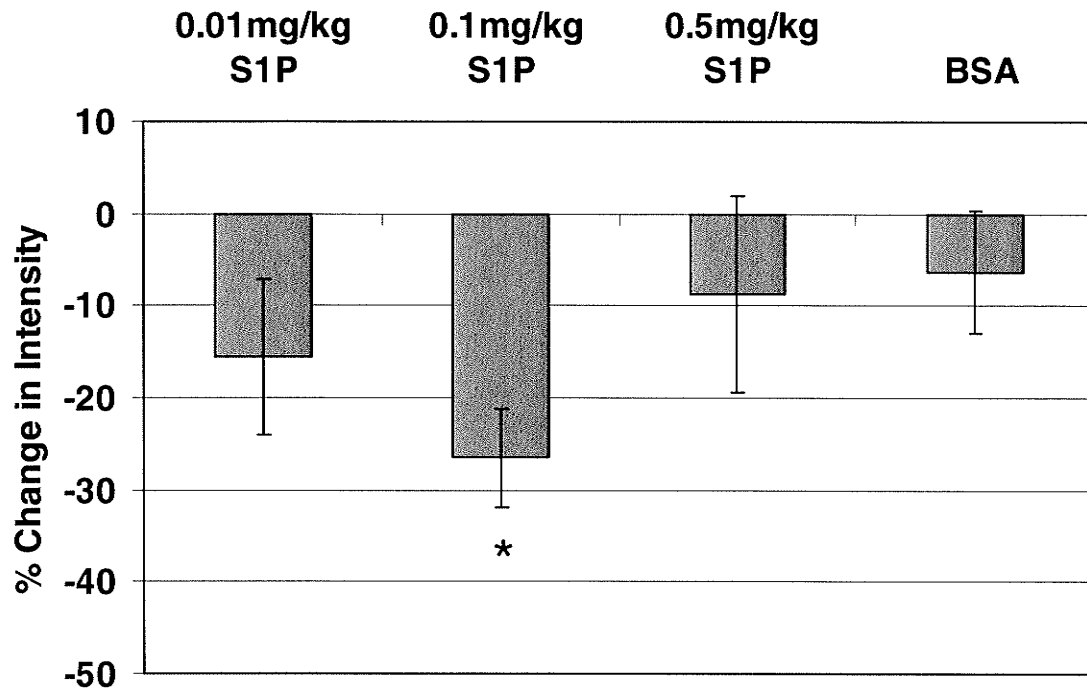


**Figure 8.9.** The average percent change in intensity within the spinal cord on calculated contrast enhanced difference images at the initial stage of disease (pre-dosing) relative to 6hr post S1P/BSA administration. \* differs from BSA ( $p < 0.05$ ).

### 8.3.4 MTR

The average MTR within the white and grey matter of the spinal cord was measured from calculated MTR maps (Figure 8.10). There was a significant decrease in the MTR within the white matter at peak disease compared to pre-disease values in groups of mice that received 0.01mg/kg S1P ( $p<0.0001$ ), 0.1mg/kg S1P ( $p<0.001$ ) and BSA ( $p<0.001$ ) with dosing beginning at the onset of disease, but no significant decrease was found for the group of mice that received 0.5mg/kg S1P (Figure 8.11B). MTR values within the white matter at remission for mice receiving treatment starting at the onset of disease all showed a significant decrease from the pre-disease values (Figure 8.11B) for 0.01mg/kg S1P, 0.1mg/kg S1P, and BSA ( $p<0.0001$ ), and 0.5mg/kg S1P ( $p<0.001$ ). The MTR values within the white matter were generally higher in comparison to the values in the grey matter. Groups of mice that began S1P or BSA treatment at the onset of disease signs showed a significant decrease in the MTR in the grey matter of the spinal cord at peak disease following 0.01mg/kg S1P ( $p<0.0005$ ), 0.1mg/kg S1P ( $p<0.05$ ), and BSA ( $p<0.005$ ), but no significant decrease was found following 0.5mg/kg S1P (Figure 8.11A). Similar results were observed at remission where there was a significant decrease in MTR from pre-disease within the grey matter of the spinal cord for the groups of mice that received 0.01mg/kg S1P ( $p<0.001$ ), 0.1mg/kg S1P ( $p<0.001$ ), and BSA ( $p<0.05$ ), but no significant decrease was found following 0.5mg/kg S1P (Figure 8.11A). For mice where treatment was begun at day 7 pre-disease, there was a decrease in MTR relative to pre-disease values within the grey matter at peak disease following 0.1mg/kg S1P ( $p<0.01$ ) and BSA ( $p<0.005$ ) and at remission following 0.01mg/kg S1P ( $p<0.05$ ), 0.5mg/kg S1P ( $p<0.01$ ), and BSA

( $p < 0.05$ ). MTR values within the grey matter at peak disease following 0.01mg/kg S1P and 0.5mg/kg S1P and at remission following 0.1mg/kg S1P did not differ from pre-disease values. Within white matter, there was a decrease in the MTR compared to pre-disease values at peak and remission in all groups of mice, except following 0.5mg/kg S1P at peak disease (at peak disease: 0.01mg/kg S1P ( $p < 0.05$ ), 0.1mg/kg S1P ( $p < 0.0001$ ), BSA ( $p < 0.001$ ) and at remission: all groups ( $p < 0.0001$ )).

### 8.3.5 *Spinal Cord Volume*

The spinal cord volume spanning the imaged region of the spinal cord was calculated at the various time points of disease progression. The percent change in cord volume at the initial stage of disease, peak disease, and remission in the different S1P treatment groups did not differ from the BSA control group at the respective time point (Figure 8.13).

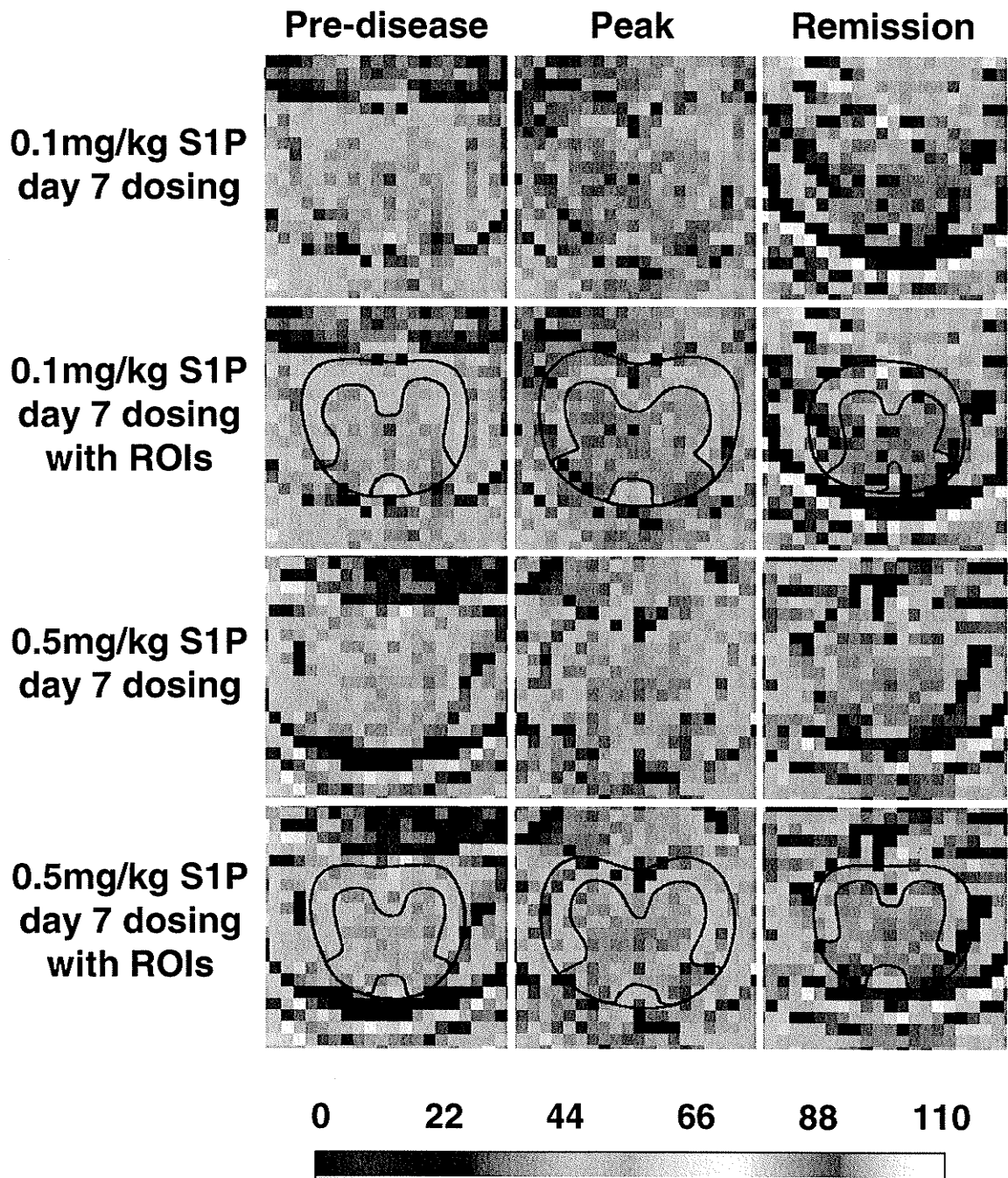


**Figure 8.10.** Representative MTR maps (2mm×2mm) at various time points of disease progression of mice that were administered 0.1mg/kg and 0.5mg/kg S1P.

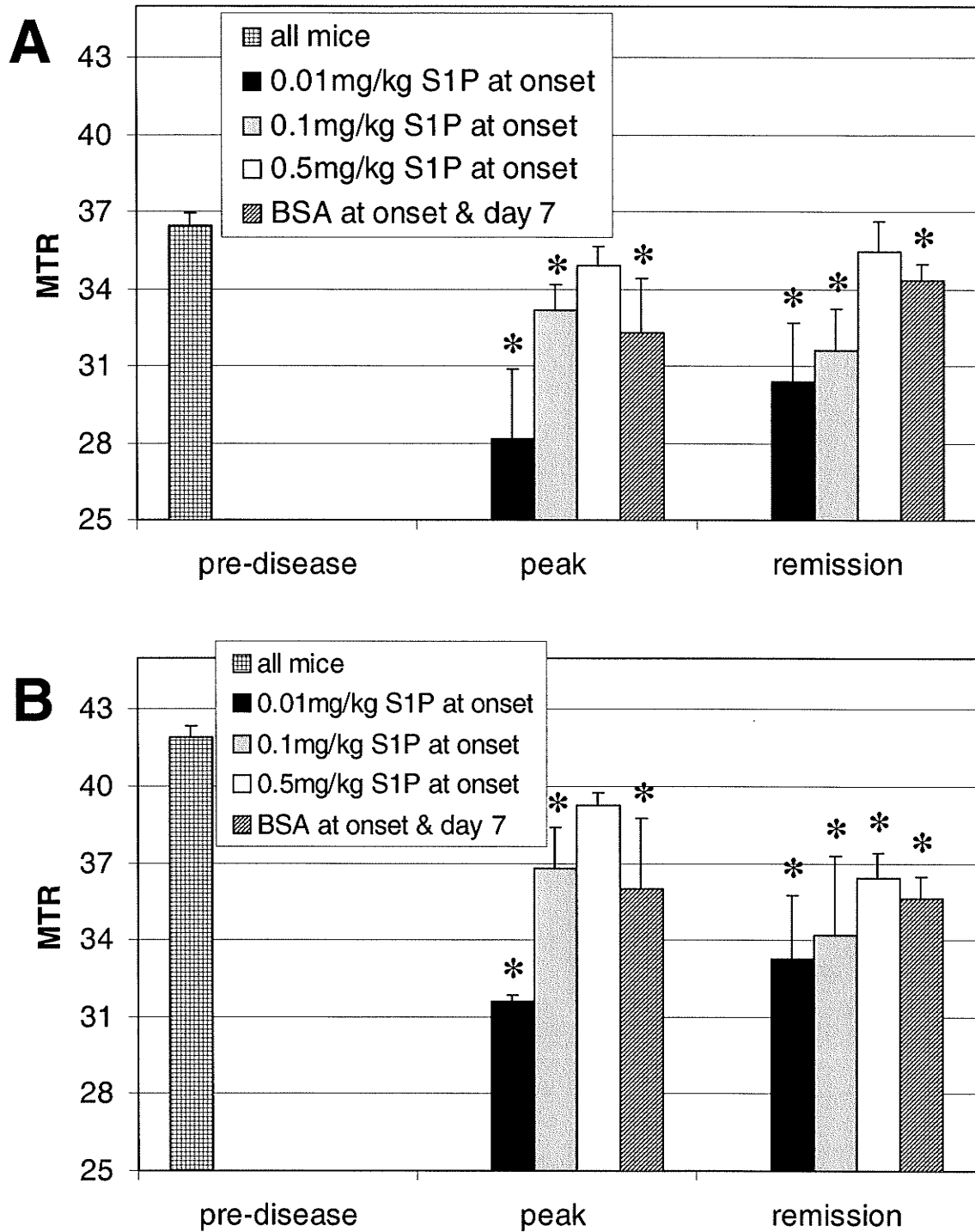


**Figure 8.11.** The average MTR  $\pm$  SEM within the (A) grey and (B) white matter of the spinal cord of mice that were administered S1P or BSA beginning at the onset of disease signs. \* differs from pre-disease.

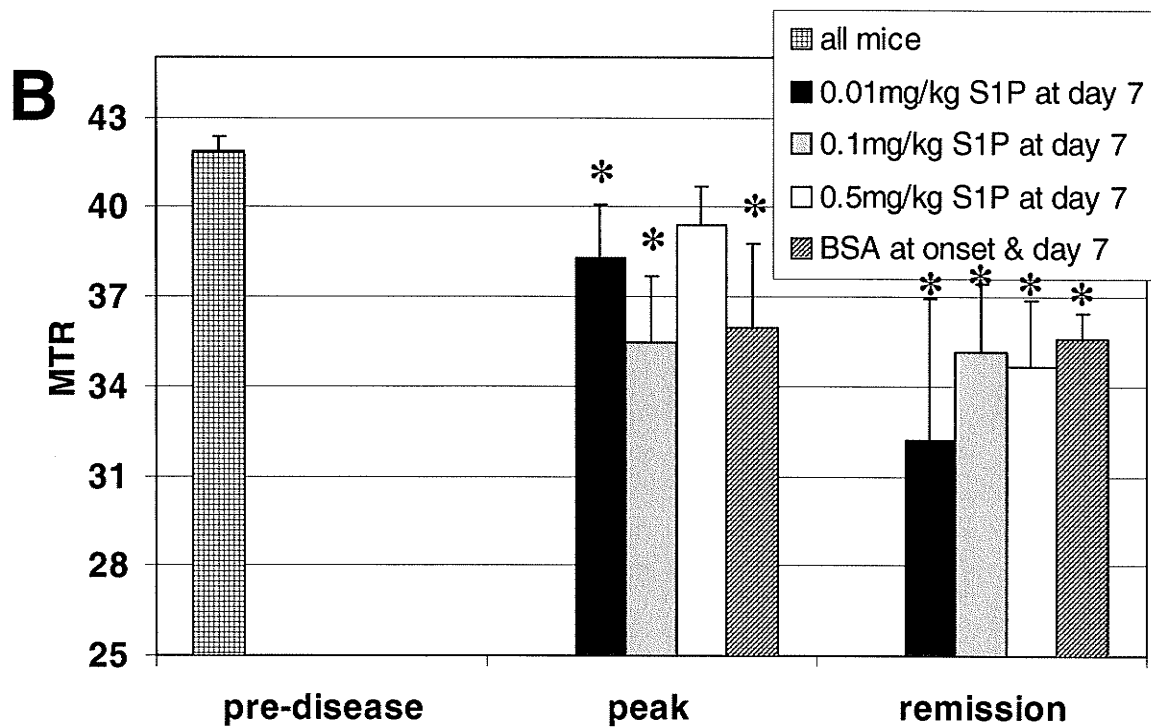
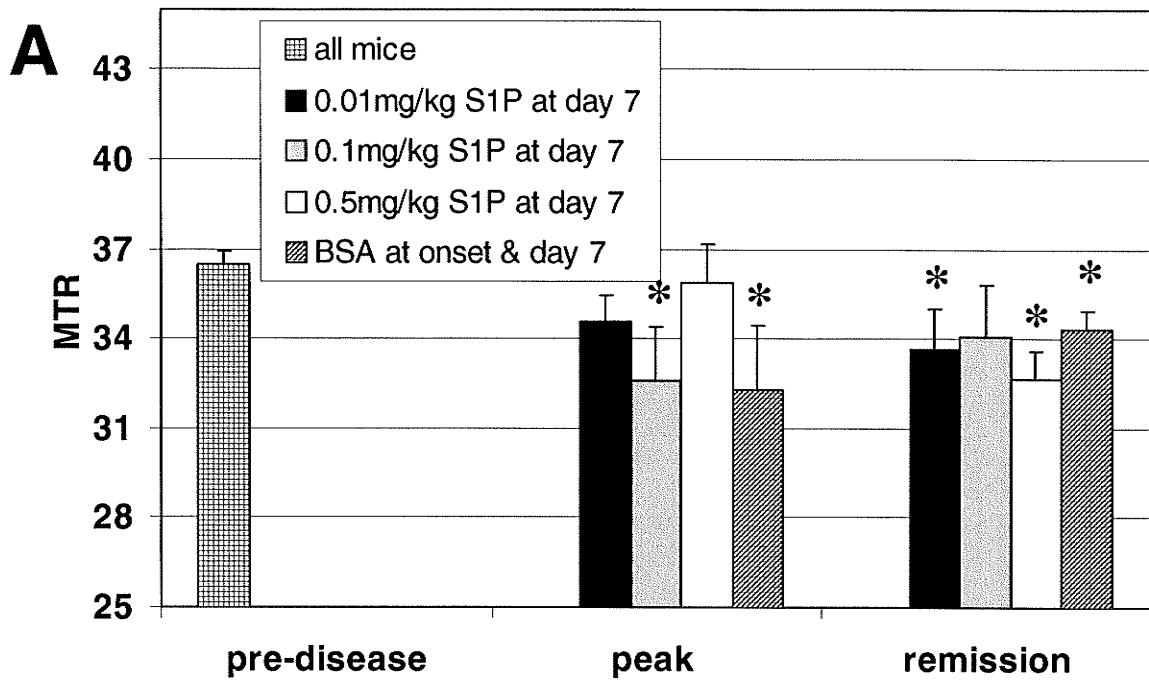


**Figure 8.12.** The average MTR  $\pm$  SEM within the (A) grey and (B) white matter of the spinal cord of mice that were administered S1P or BSA beginning at day 7. \* differs from pre-disease.

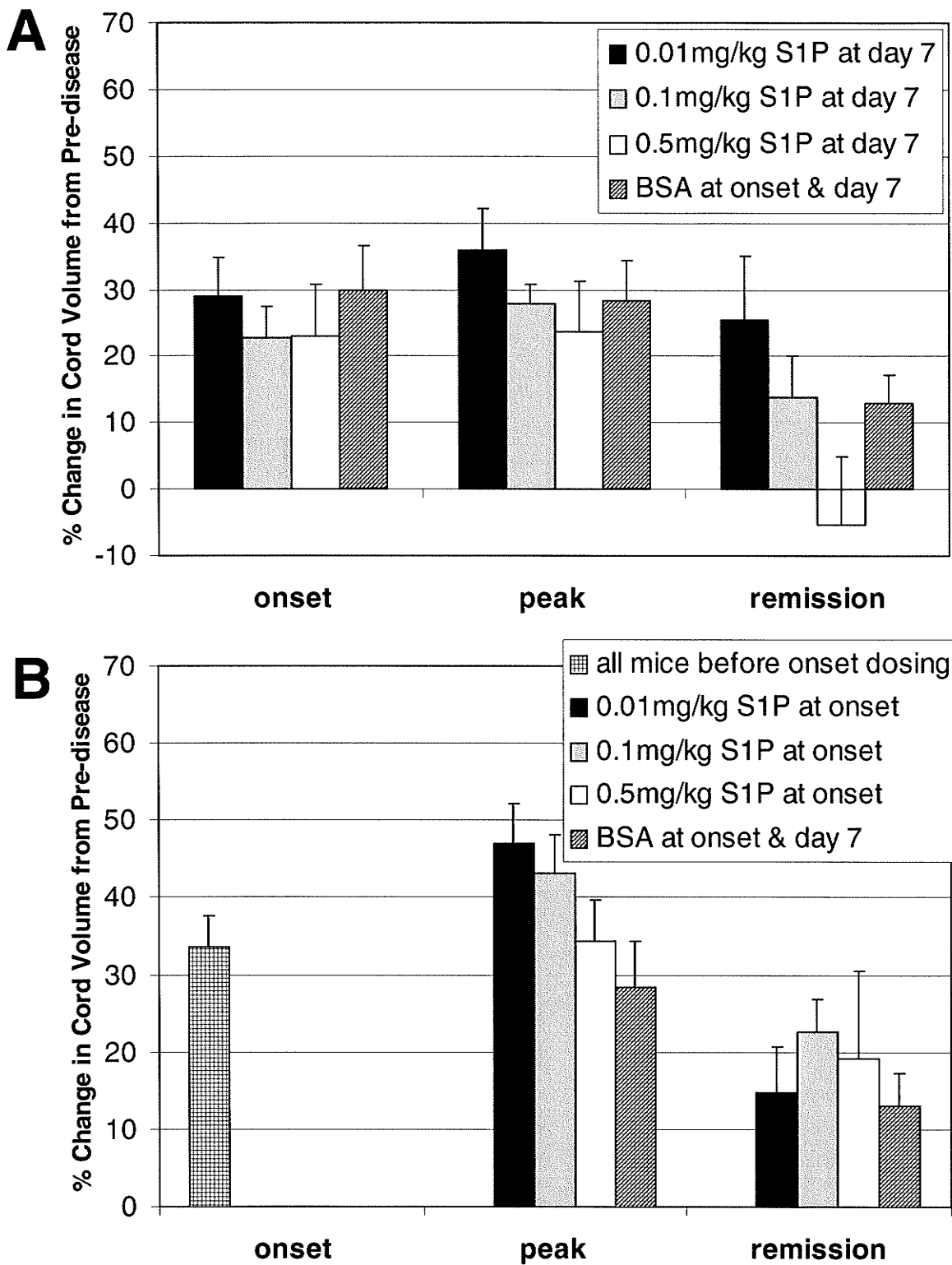


**Figure 8.13.** The average percent change in cord volume  $\pm$  SEM relative to pre-disease values with first administration of S1P/BSA at (A) day 7 and at (B) initial signs of disease.

## 8.4 DISCUSSION

### 8.4.1 Behavioural Scores

The day of disease onset did not differ between any of the treatment groups, indicating that the administration of S1P, regardless of the dose or onset of first dosing, did not affect the rate of disease development. The treatment group that had a significantly lower maximum score compared to the BSA control group was the group receiving 0.5mg/kg S1P that was first administered before any signs of disease were evident. The administration of this high dose of S1P before inflammation and BSB breakdown had begun was important in reducing disease severity. Previous studies have demonstrated that the S1P receptor agonist FTY720 has been successful in reducing disease in various models of EAE. The daily dosing of FTY720 in SJL mice with relapsing-remitting EAE when signs of disease were already evident resulted in a significant improvement of disease score<sup>174,175</sup> and inhibited further relapses and disease progression in Lewis rat models of EAE.<sup>171,176</sup> The administration of FTY720 before signs of disease were evident resulted in a delayed onset of disease with reduced severity in SJL mice,<sup>174,175</sup> while signs of disease did not develop in Lewis rats.<sup>175-177</sup> FTY720-P was found to have a higher potency than S1P at receptors S1P<sub>1</sub> and S1P<sub>4</sub>,<sup>170</sup> which may cause it to be more effective in reducing signs of disease and delaying onset in these previous studies.

#### *8.4.2 Changes in Weight*

Mice that received S1P/BSA beginning at the onset of disease signs showed a general trend of reaching a higher initial weight at pre-disease than mice that first received treatment at day 7. The daily administration of S1P was conducted by briefly anesthetizing each mouse using isoflurane as the intravenous injection was performed. The natural increase in weight prior to disease onset may have been disrupted in the mice that received treatment beginning earlier due to the administration of daily anesthetic.

#### *8.4.3 Contrast Enhancement*

The degree of contrast enhancement throughout disease progression was the same as previously described in detail in chapter 5, where maximum enhancement occurred at the very first signs of disease. This study provided further information by dividing the spinal cord into grey and white matter regions. ROIs that were determined from MT-weighted images were superimposed onto calculated  $T_1$ -weighted difference images, which confirmed that the ring of greatest enhancing pixels was located within the white matter. Increased vascular permeability within the white matter correlated to the area of maximum inflammation and demyelination in this mouse model of EAE as described in chapter 5.

Mice that received 0.1mg/kg S1P showed a significant decrease in Gd-DTPA enhancement after 6 hours compared to control mice. This dose of S1P was effective in reducing the permeability of a disrupted BSB following a short period of time. S1P is

known to enhance the function of vascular endothelium by rearranging the actin cytoskeleton of endothelial cells.<sup>166,167</sup>

There were no significant differences in contrast enhancement between any groups of mice at any time point suggesting that S1P may not have a long-term protective effect on the BSB or that the experiment lacked statistical power. Previous studies have shown that BBB/BSB disruption is dependent on metabolic changes resulting in increased vesicular transport across endothelial cells.<sup>119</sup> Other mechanisms where the actions of S1P are ineffective may contribute to the increased permeability of the BSB in the long term.

#### *8.4.4 MTR*

In this study the average MTR within the grey and white matter of the spinal cord at pre-disease was 36.4% and 41.9% respectively. The MTR in normal white matter was calculated to be 40% - 45% in an earlier study of humans and animals, whereas the MTR within the grey matter was 35% - 38%.<sup>104</sup> There was no significant decrease in MTR within white matter at peak disease in the group of mice receiving 0.5mg/kg S1P beginning at day 7. MTR is believed to reflect the amount of myelin content in tissue; therefore a significant decrease in MTR indicates demyelination. Previous studies of EAE in rat showed a reduced MTR within the brain during acute disease that correlated with infiltrated macrophages, which are the major contributors of demyelination.<sup>56,59</sup> Lesions of demyelination seen histologically in rat brain have also been directly correlated with a decrease in MTR and subsequent remyelination corresponded to a return to normal values.<sup>178,179</sup> The lack of significant decrease in

MTR at peak disease following 0.5mg/kg SIP with early dosing at day 7 suggests that this dosing regimen reduced the inflammatory response and subsequent demyelination. The number of peripheral blood lymphocytes in circulation decreased following FTY720 dosing in models of EAE,<sup>174</sup> leading to reduced inflammation in the CNS.<sup>171,176,177</sup> When dosing of FTY720 was discontinued, the numbers of circulating lymphocytes increased indicating that the decline in peripheral blood lymphocytes is a reversible effect.<sup>174</sup>

The presence of edema could be the explanation for the decrease in MTR within the grey matter in this model of EAE. Lesions within the brain of guinea pigs that showed edema with very little demyelination had a MTR that was decreased by 5% - 8%.<sup>104</sup> No differences in spinal cord volume were present at each respective time point, suggesting that the amount of edema formation within the spinal cord was similar across all groups.

## **CHAPTER IX**

### **CONCLUSIONS**

The inflammatory processes resulting in demyelination in the MOG-induced mouse model of EAE are representative of the autoimmune inflammation observed in MS in humans. An understanding of the mechanisms that initiate lesion formation and disability in mice with EAE are important in order to study the effects of pharmacological interventions and genetic alterations.

Each C57Bl/6 mouse with MOG-induced EAE examined using T<sub>1</sub>-weighted contrast-enhanced MRI at the earliest stage of disease demonstrated disruption of the BSB at the level of the lumbar spinal cord. BSB opening was an early event during disease progression that preceded maximum inflammation of the lumbar spinal cord. A reproducible MRI protocol to accurately examine mouse lumbar spinal cord that involved administering a consistent amount of Gd-DTPA contrast agent for contrast-enhanced MRI was developed and proved to be reliable in obtaining quantitative data. This tool was used to examine the effects of genetic alterations in a mouse model of EAE. Knockout mice for the A1AR receptor did not show any significant differences in relative BSB permeability within the lumbar spinal cord than corresponding wild type mice at any stage of disease.

The relative degree of BBB disruption was examined in a mouse model of CNS inflammation induced through the upregulation of chemokine CCL2 and the administration of PTx. Permeability of the endothelial cell barrier and the glia limitans barrier was required to cause complete disruption of the BBB as visualized with T<sub>1</sub>-weighted contrast-enhanced MR imaging and histological tracers. Cellular infiltrates into the brain parenchyma accompanied a disrupted BBB, which specifically

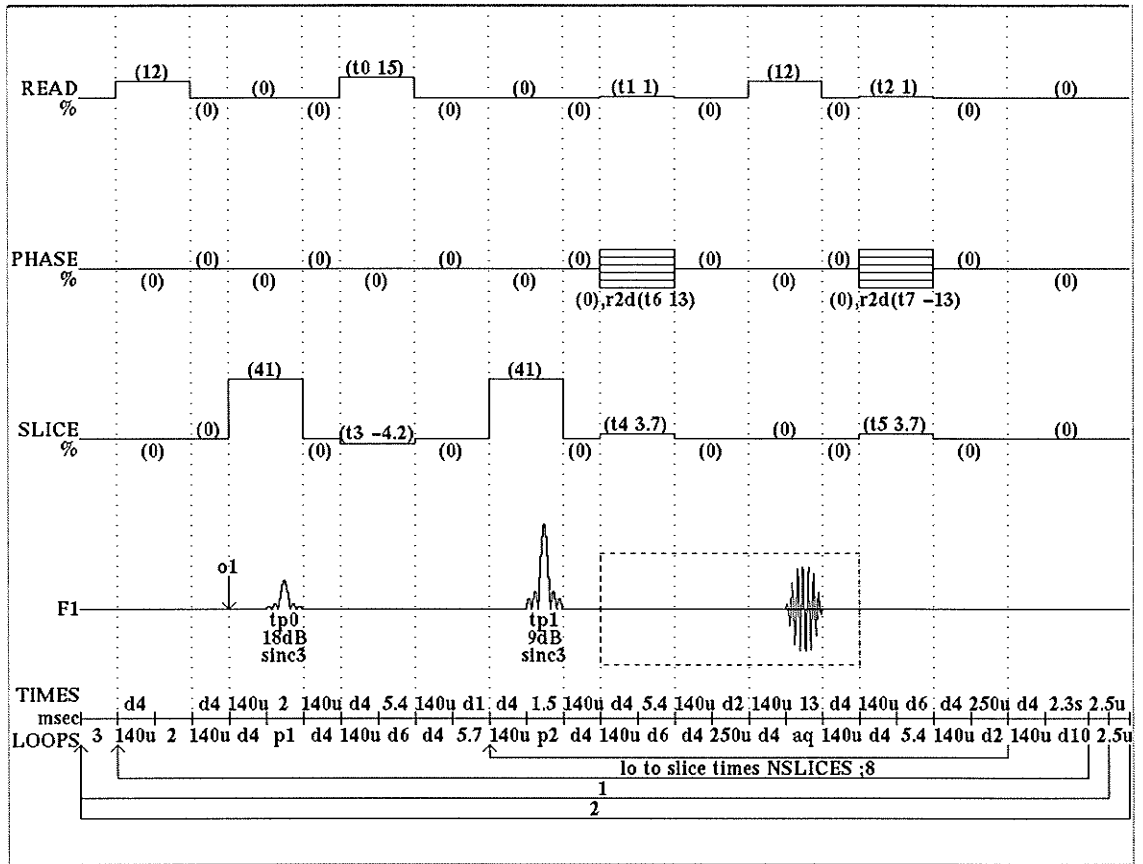
demonstrated a dual role of the endothelium and glia limitans in the regulation of cellular migration across the BBB.

Currently for patients with MS there are no treatments available that are completely effective in inhibiting the destructive autoimmune processes that occur within the CNS. SIP is a possible candidate for treating MS through the actions of sequestering harmful autoimmune CD4<sup>+</sup> T cells within peripheral lymph nodes. The use of SIP in the MOG-induced mouse model of EAE demonstrated long-term effects of reduced demyelination using MT-weighted MRI. A further study comparing the demyelination seen histologically would be beneficial to investigate the changes in MTR observed using MT-weighted MRI.

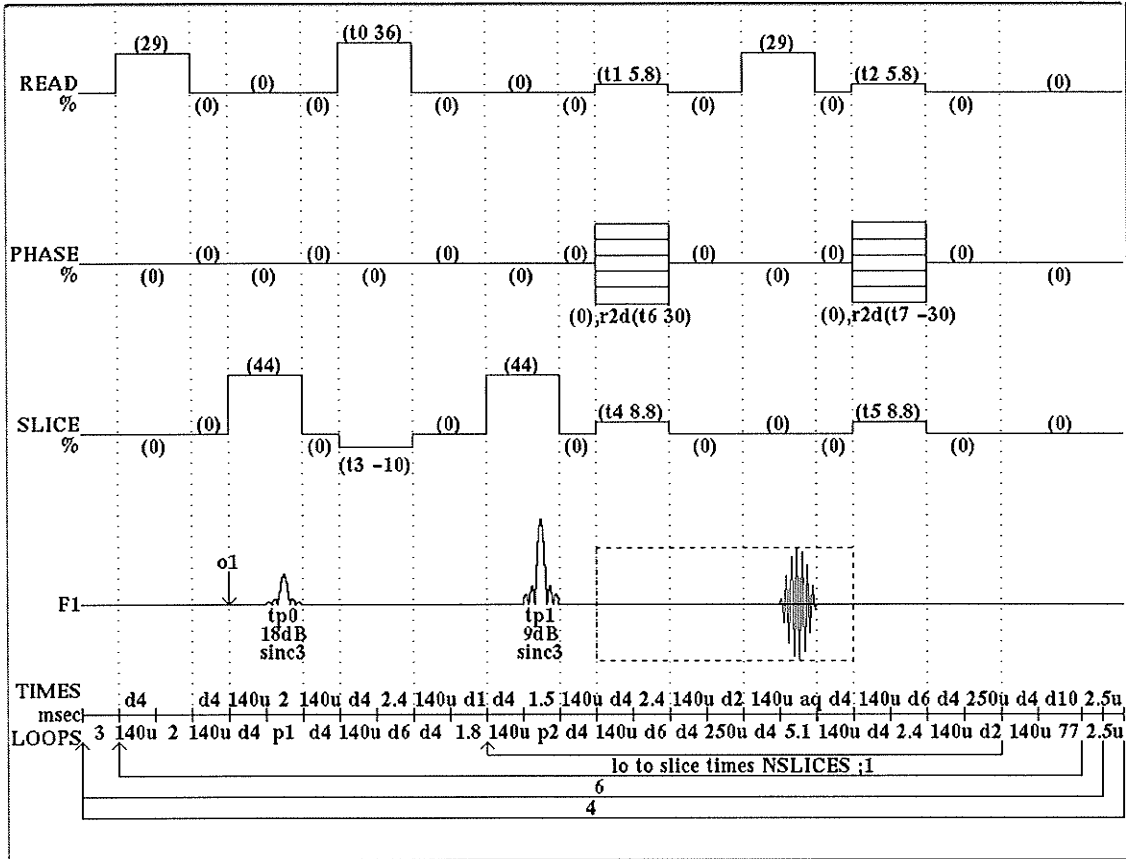
A future study looking at the effects of a MMP inhibitor on BBB/BSB permeability in a model of EAE and using contrast-enhanced MRI may help in further identifying the mechanism of BBB/BSB breakdown. In particular, MMP-9 has been found to be elevated in demyelinating lesions,<sup>71</sup> serum<sup>67,70,180</sup> and CSF<sup>69</sup> of patients with MS and may be a good target for inhibition and a possible candidate for future treatment of MS.

## **APPENDIX A**

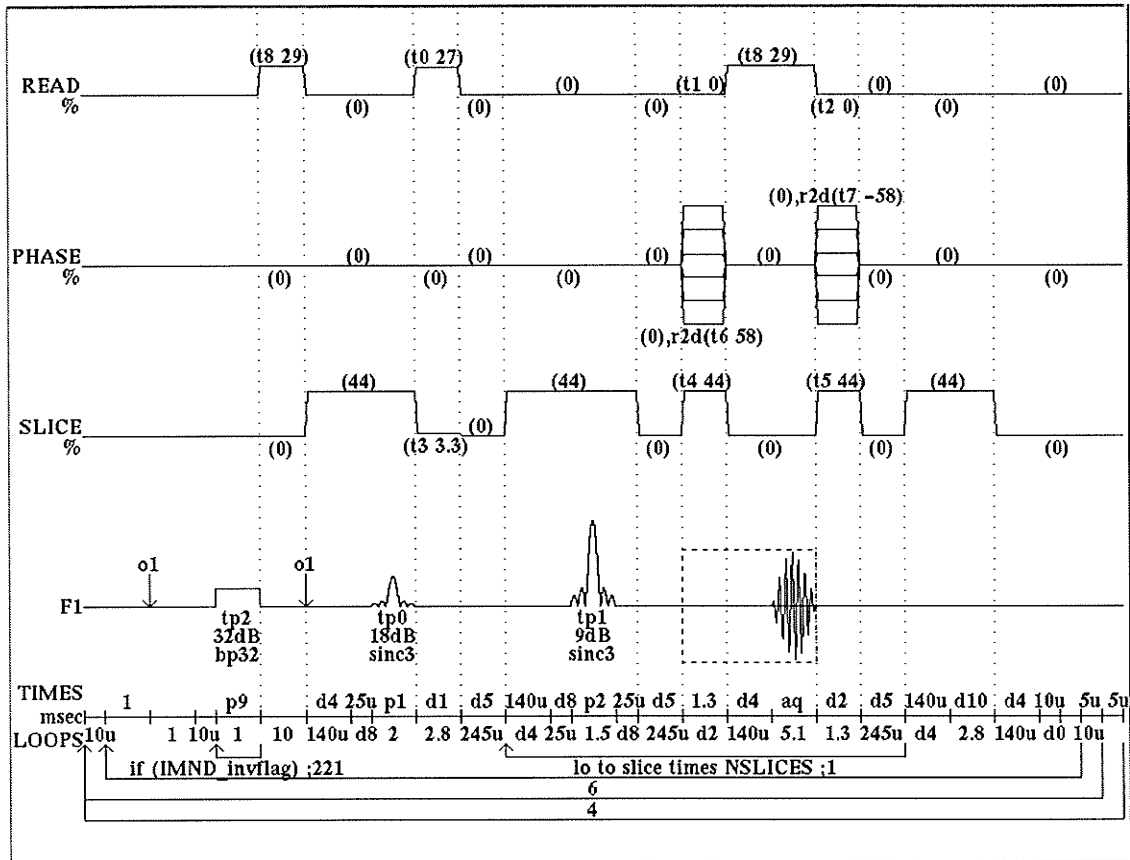
# Pulse sequence for T<sub>2</sub>-weighted imaging



# Pulse sequence for T1-weighted imaging



# Pulse sequence for MT-weighted imaging with saturation pulse





## REFERENCES

1. Steinman L, Zamvil SS. Virtues and pitfalls of EAE for the development of therapies for multiple sclerosis. *Trends Immunol* 2005; 26(11):565-571.
2. Noseworthy JH, Lucchinetti C, Rodriguez M, Weinshenker BG. Multiple sclerosis. *N Engl J Med* 2000; 343(13):938-952.
3. Martin R, McFarland HF. Immunological aspects of experimental allergic encephalomyelitis and multiple sclerosis. *Crit Rev Clin Lab Sci* 1995; 32(2):121-182.
4. Al Omaishi J, Bashir R, Gendelman HE. The cellular immunology of multiple sclerosis. *J Leukoc Biol* 1999; 65(4):444-452.
5. Fox RJ, Ransohoff RM. New directions in MS therapeutics: vehicles of hope. *Trends Immunol* 2004; 25(12):632-636.
6. Compston A, Coles A. Multiple sclerosis. *Lancet* 2002; 359(9313):1221-1231.
7. Martin R, McFarland HF, McFarlin DE. Immunological aspects of demyelinating diseases. *Annu Rev Immunol* 1992; 10:153-187.
8. Waksman BH, Reynolds WE. Multiple sclerosis as a disease of immune regulation. *Proc Soc Exp Biol Med* 1984; 175(3):282-294.
9. McFarlin DE, McFarland HF. Multiple sclerosis (first of two parts). *N Engl J Med* 1982; 307(19):1183-1188.
10. Bowen J. Diagnosing multiple sclerosis and its imitators. *Phys Med Rehabil Clin N Am* 2005; 16(2):359-381.
11. Warren S. *Multiple Sclerosis*. Geneva: 2001.
12. Dyment DA, Ebers GC, Sadovnick AD. Genetics of multiple sclerosis. *Lancet Neurol* 2004; 3(2):104-110.
13. Hartung HP, Bar-Or A, Zoukos Y. What do we know about the mechanism of action of disease-modifying treatments in MS? *J Neurol* 2004; 251 Suppl 5:v12-v29.
14. Neuhaus O, Archelos JJ, Hartung HP. Immunomodulation in multiple sclerosis: from immunosuppression to neuroprotection. *Trends Pharmacol Sci* 2003; 24(3):131-138.

15. Sospedra M, Martin R. Immunology of multiple sclerosis. *Annu Rev Immunol* 2005; 23:683-747.
16. El Behi M, Dubucquoi S, Lefranc D, Zephir H, De Seze J, Vermersch P, Prin L. New insights into cell responses involved in experimental autoimmune encephalomyelitis and multiple sclerosis. *Immunol Lett* 2005; 96(1):11-26.
17. Cui JY. Multiple sclerosis: an immunologic perspective. *Phys Med Rehabil Clin N Am* 2005; 16(2):351-358.
18. Yong VW. Differential mechanisms of action of interferon-beta and glatiramer acetate in MS. *Neurology* 2002; 59(6):802-808.
19. Traugott U, Lebon P. Multiple sclerosis: involvement of interferons in lesion pathogenesis. *Ann Neurol* 1988; 24(2):243-251.
20. Raine CS. Biology of disease. Analysis of autoimmune demyelination: its impact upon multiple sclerosis. *Lab Invest* 1984; 50(6):608-635.
21. Qin Y, Duquette P. B-cell immunity in MS. *Int MS J* 2003; 10(4):110-120.
22. Olsson T. Critical influences of the cytokine orchestration on the outcome of myelin antigen-specific T-cell autoimmunity in experimental autoimmune encephalomyelitis and multiple sclerosis. *Immunol Rev* 1995; 144:245-268.
23. Navikas V, Link H. Review: cytokines and the pathogenesis of multiple sclerosis. *J Neurosci Res* 1996; 45(4):322-333.
24. Ransohoff RM. Mechanisms of inflammation in MS tissue: adhesion molecules and chemokines. *J Neuroimmunol* 1999; 98(1):57-68.
25. Ubogu EE, Cossoy MB, Ransohoff RM. The expression and function of chemokines involved in CNS inflammation. *Trends Pharmacol Sci* 2006; 27(1):48-55.
26. Zlotnik A, Yoshie O. Chemokines: a new classification system and their role in immunity. *Immunity* 2000; 12(2):121-127.
27. Bacon K, Baggiolini M, Broxmeyer H, Horuk R, Lindley I, Mantovani A, Maysushima K, Murphy P, Nomiyama H, Oppenheim J, Rot A, Schall T, Tsang M, Thorpe R, Van Damme J, Wadhwa M, Yoshie O, Zlotnik A, Zoon K. Chemokine/chemokine receptor nomenclature. *J Interferon Cytokine Res* 2002; 22(10):1067-1068.
28. Selmaj K, Raine CS, Cannella B, Brosnan CF. Identification of lymphotoxin and tumor necrosis factor in multiple sclerosis lesions. *J Clin Invest* 1991; 87(3):949-954.

29. Rieckmann P, Albrecht M, Kitze B, Weber T, Tumani H, Broocks A, Luer W, Poser S. Cytokine mRNA levels in mononuclear blood cells from patients with multiple sclerosis. *Neurology* 1994; 44(8):1523-1526.
30. Rieckmann P, Albrecht M, Kitze B, Weber T, Tumani H, Broocks A, Luer W, Helwig A, Poser S. Tumor necrosis factor-alpha messenger RNA expression in patients with relapsing-remitting multiple sclerosis is associated with disease activity. *Ann Neurol* 1995; 37(1):82-88.
31. Cannella B, Raine CS. Cytokines up-regulate Ia expression in organotypic cultures of central nervous system tissue. *J Neuroimmunol* 1989; 24(3):239-248.
32. Gonsette RE. New immunosuppressants with potential implication in multiple sclerosis. *J Neurol Sci* 2004; 223(1):87-93.
33. Miller DH, Khan OA, Sheremata WA, Blumhardt LD, Rice GP, Libonati MA, Willmer-Hulme AJ, Dalton CM, Miszkiel KA, O'Connor PW. A controlled trial of natalizumab for relapsing multiple sclerosis. *N Engl J Med* 2003; 348(1):15-23.
34. Rieckmann P. Neurodegeneration and clinical relevance for early treatment in multiple sclerosis. *Int MS J* 2005; 12(2):42-51.
35. Lutton JD, Winston R, Rodman TC. Multiple sclerosis: etiological mechanisms and future directions. *Exp Biol Med (Maywood)* 2004; 229(1):12-20.
36. Traugott U, McFarlin DE, Raine CS. Immunopathology of the lesion in chronic relapsing experimental autoimmune encephalomyelitis in the mouse. *Cell Immunol* 1986; 99(2):395-410.
37. Tonra JR, Reiseter BS, Kolbeck R, Nagashima K, Robertson R, Keyt B, Lindsay RM. Comparison of the timing of acute blood-brain barrier breakdown to rabbit immunoglobulin G in the cerebellum and spinal cord of mice with experimental autoimmune encephalomyelitis. *J Comp Neurol* 2001; 430(1):131-144.
38. Lossinsky AS, Badmajew V, Robson JA, Moretz RC, Wisniewski HM. Sites of egress of inflammatory cells and horseradish peroxidase transport across the blood-brain barrier in a murine model of chronic relapsing experimental allergic encephalomyelitis. *Acta Neuropathol* 1989; 78(4):359-371.
39. Muller DM, Pender MP, Greer JM. Blood-brain barrier disruption and lesion localisation in experimental autoimmune encephalomyelitis with predominant cerebellar and brainstem involvement. *J Neuroimmunol* 2005; 160(1-2):162-169.

40. Oldstone MB, Dixon FJ. Immunohistochemical study of allergic encephalomyelitis. *Am J Pathol* 1968; 52(2):251-263.
41. Juhler M, Barry DI, Offner H, Konat G, Klinken L, Paulson OB. Blood-brain and blood-spinal cord barrier permeability during the course of experimental allergic encephalomyelitis in the rat. *Brain Res* 1984; 302(2):347-355.
42. Juhler M, Blasberg RG, Fenstermacher JD, Patlak CS, Paulson OB. A spatial analysis of the blood-brain barrier damage in experimental allergic encephalomyelitis. *J Cereb Blood Flow Metab* 1985; 5(4):545-553.
43. Wuerfel J, Tysiak E, Prozorovski T, Smyth M, Mueller S, Schnorr J, Taupitz M, Zipp F. Mouse model mimics multiple sclerosis in the clinico-radiological paradox. *Eur J Neurosci* 2007; 26(1):190-198.
44. Leibowitz S, Kennedy L. Cerebral vascular permeability and cellular infiltration in experimental allergic encephalomyelitis. *Immunology* 1972; 22(5):859-869.
45. Cutler RW, Lorenzo AV, Barlow CF. Brain vascular permeability to I-125 gamma globulin and leukocytes in allergic encephalomyelitis. *J Neuropathol Exp Neurol* 1967; 26(4):558-571.
46. Kristensson K, Wisniewski HM. Chronic relapsing experimental allergic encephalomyelitis. Studies in vascular permeability changes. *Acta Neuropathol* 1977; 39(3):189-194.
47. Kitz K, Lassmann H, Karcher D, Lowenthal A. Blood-brain barrier in chronic relapsing experimental allergic encephalomyelitis: a correlative study between cerebrospinal fluid protein concentrations and tracer leakage in the central nervous system. *Acta Neuropathol* 1984; 63(1):41-50.
48. Barlow CF. A study of abnormal blood-brain permeability in experimental allergic encephalomyelitis. *J Neuropathol Exp Neurol* 1956; 15(2):196-207.
49. Kuharik MA, Edwards MK, Farlow MR, Becker GJ, Azzarelli B, Klatte EC, Augustyn GT, Dreesen RG. Gd-enhanced MR imaging of acute and chronic experimental demyelinating lesions. *AJNR Am J Neuroradiol* 1988; 9(4):643-648.
50. Zamvil SS, Steinman L. The T lymphocyte in experimental allergic encephalomyelitis. *Annu Rev Immunol* 1990; 8:579-621.
51. Seeldrayers PA, Syha J, Morrissey SP, Stodal H, Vass K, Jung S, Gneiting T, Lassmann H, Haase A, Hartung HP, . Magnetic resonance imaging investigation of blood-brain barrier damage in adoptive transfer experimental autoimmune encephalomyelitis. *J Neuroimmunol* 1993; 46(1-2):199-206.

52. Wekerle H, Kojima K, Lannes-Vieira J, Lassmann H, Linington C. Animal models. *Ann Neurol* 1994; 36 Suppl:S47-S53.
53. Petry KG, Boullerne AI, Pousset F, Brochet B, Caille JM, Dousset V. Experimental allergic encephalomyelitis animal models for analyzing features of multiple sclerosis. *Pathol Biol (Paris)* 2000; 48(1):47-53.
54. Morrissey SP, Stodal H, Zettl U, Simonis C, Jung S, Kiefer R, Lassmann H, Hartung HP, Haase A, Toyka KV. In vivo MRI and its histological correlates in acute adoptive transfer experimental allergic encephalomyelitis. Quantification of inflammation and oedema. *Brain* 1996; 119 ( Pt 1):239-248.
55. Traugott U, Raine CS, McFarlin DE. Acute experimental allergic encephalomyelitis in the mouse: immunopathology of the developing lesion. *Cell Immunol* 1985; 91(1):240-254.
56. Rausch M, Hiestand P, Baumann D, Cannet C, Rudin M. MRI-based monitoring of inflammation and tissue damage in acute and chronic relapsing EAE. *Magn Reson Med* 2003; 50(2):309-314.
57. Lampert P, Carpenter S. Electron microscopic studies on the vascular permeability and the mechanism of demyelination in experimental allergic encephalomyelitis. *J Neuropathol Exp Neurol* 1965; 24:11-24.
58. Hohlfeld R, Wekerle H. Autoimmune concepts of multiple sclerosis as a basis for selective immunotherapy: from pipe dreams to (therapeutic) pipelines. *Proc Natl Acad Sci U S A* 2004; 101 Suppl 2:14599-14606.
59. Berger C, Hiestand P, Kindler-Baumann D, Rudin M, Rausch M. Analysis of lesion development during acute inflammation and remission in a rat model of experimental autoimmune encephalomyelitis by visualization of macrophage infiltration, demyelination and blood-brain barrier damage. *NMR Biomed* 2006; 19(1):101-107.
60. Goldstein GW. Endothelial cell-astrocyte interactions. A cellular model of the blood-brain barrier. *Ann N Y Acad Sci* 1988; 529:31-39.
61. Pachter JS, de Vries HE, Fabry Z. The blood-brain barrier and its role in immune privilege in the central nervous system. *J Neuropathol Exp Neurol* 2003; 62(6):593-604.
62. Prat A, Biernacki K, Lavoie JF, Poirier J, Duquette P, Antel JP. Migration of multiple sclerosis lymphocytes through brain endothelium. *Arch Neurol* 2002; 59(3):391-397.
63. Abbott NJ. Dynamics of CNS barriers: evolution, differentiation, and modulation. *Cell Mol Neurobiol* 2005; 25(1):5-23.

64. Greter M, Heppner FL, Lemos MP, Odermatt BM, Goebels N, Laufer T, Noelle RJ, Becher B. Dendritic cells permit immune invasion of the CNS in an animal model of multiple sclerosis. *Nat Med* 2005; 11(3):328-334.
65. Becher B, Bechmann I, Greter M. Antigen presentation in autoimmunity and CNS inflammation: how T lymphocytes recognize the brain. *J Mol Med* 2006; 84(7):532-543.
66. Sixt M, Engelhardt B, Pausch F, Hallmann R, Wendler O, Sorokin LM. Endothelial cell laminin isoforms, laminins 8 and 10, play decisive roles in T cell recruitment across the blood-brain barrier in experimental autoimmune encephalomyelitis. *J Cell Biol* 2001; 153(5):933-946.
67. Ozenci V, Rinaldi L, Teleshova N, Matusevicius D, Kivisakk P, Kouwenhoven M, Link H. Metalloproteinases and their tissue inhibitors in multiple sclerosis. *J Autoimmun* 1999; 12(4):297-303.
68. Bar-Or A, Nuttall RK, Duddy M, Alter A, Kim HJ, Ifergan I, Pennington CJ, Bourgoin P, Edwards DR, Yong VW. Analyses of all matrix metalloproteinase members in leukocytes emphasize monocytes as major inflammatory mediators in multiple sclerosis. *Brain* 2003; 126(Pt 12):2738-2749.
69. Sellebjerg F, Sorensen TL. Chemokines and matrix metalloproteinase-9 in leukocyte recruitment to the central nervous system. *Brain Res Bull* 2003; 61(3):347-355.
70. Kouwenhoven M, Ozenci V, Gomes A, Yarilin D, Giedraitis V, Press R, Link H. Multiple sclerosis: elevated expression of matrix metalloproteinases in blood monocytes. *J Autoimmun* 2001; 16(4):463-470.
71. Cossins JA, Clements JM, Ford J, Miller KM, Pigott R, Vos W, Van d, V, De Groot CJ. Enhanced expression of MMP-7 and MMP-9 in demyelinating multiple sclerosis lesions. *Acta Neuropathol* 1997; 94(6):590-598.
72. Olsson Y, Svensjo E, Arfors KE, Hultstrom D. Fluorescein labelled dextrans as tracers for vascular permeability studies in the nervous system. *Acta Neuropathol* 1975; 33(1):45-50.
73. Hultstrom D, Malmgren L, Gilström D, Olsson Y. FITC-Dextrans as tracers for macromolecular movements in the nervous system. A freeze-drying method for dextrans of various molecular sizes injected into normal animals. *Acta Neuropathol* 1983; 59(1):53-62.
74. Yepes M, Sandkvist M, Moore EG, Bugge TH, Strickland DK, Lawrence DA. Tissue-type plasminogen activator induces opening of the blood-brain barrier via the LDL receptor-related protein. *J Clin Invest* 2003; 112(10):1533-1540.

75. Young PP, Fantz CR, Sands MS. VEGF disrupts the neonatal blood-brain barrier and increases life span after non-ablative BMT in a murine model of congenital neurodegeneration caused by a lysosomal enzyme deficiency. *Exp Neurol* 2004; 188(1):104-114.
76. Ding-Zhou L, Marchand-Verrecchia C, Croci N, Plotkine M, Margail I. L-NAME reduces infarction, neurological deficit and blood-brain barrier disruption following cerebral ischemia in mice. *Eur J Pharmacol* 2002; 457(2-3):137-146.
77. Claudio L, Kress Y, Norton WT, Brosnan CF. Increased vesicular transport and decreased mitochondrial content in blood-brain barrier endothelial cells during experimental autoimmune encephalomyelitis. *Am J Pathol* 1989; 135(6):1157-1168.
78. Hirano A, Dembitzer HM, Becker NH, Levine S, Zimmerman HM. Fine structural alterations of the blood-brain barrier in experimental allergic encephalomyelitis. *J Neuropathol Exp Neurol* 1970; 29(3):432-440.
79. Nakagawa Y, Cervos-Navarro J, Artigas J. Tracer study on a paracellular route in experimental hydrocephalus. *Acta Neuropathol* 1985; 65(3-4):247-254.
80. Kato T, Tsuchida T, Kawamoto K. Blood tumor permeability of experimental brain tumor: an electron microscopic study using lanthanum. *Neuropathology* 2005; 25(1):21-26.
81. Bushong SC. *Magnetic Resonance Imaging: Physical and Biological Processes*. 3 ed. St. Louis: Mosby, 2003.
82. Freeman R. *Magnetic Resonance in Chemistry and Medicine*. 1 ed. New York: Oxford University Press, 2003.
83. Hashemi RH, Bradley WGJr, Lisanti CJ. *MRI: The Basics*. 1 ed. Philadelphia: Lippincott Williams & Wilkins, 2004.
84. Wolff SD, Balaban RS. Magnetization transfer imaging: practical aspects and clinical applications. *Radiology* 1994; 192(3):593-599.
85. Cook LL, Foster PJ, Mitchell JR, Karlik SJ. In vivo 4.0-T magnetic resonance investigation of spinal cord inflammation, demyelination, and axonal damage in chronic-progressive experimental allergic encephalomyelitis. *J Magn Reson Imaging* 2004; 20(4):563-571.
86. Chen JT, Kuhlmann T, Jansen GH, Collins DL, Atkins HL, Freedman MS, O'Connor PW, Arnold DL. Voxel-based analysis of the evolution of magnetization transfer ratio to quantify remyelination and demyelination with histopathological validation in a multiple sclerosis lesion. *Neuroimage* 2007; 36(4):1152-1158.

87. Gonzalez-Scarano F, Grossman RI, Galetta S, Atlas SW, Silberberg DH. Multiple sclerosis disease activity correlates with gadolinium-enhanced magnetic resonance imaging. *Ann Neurol* 1987; 21(3):300-306.
88. McFarland HF, Frank JA, Albert PS, Smith ME, Martin R, Harris JO, Patronas N, Maloni H, McFarlin DE. Using gadolinium-enhanced magnetic resonance imaging lesions to monitor disease activity in multiple sclerosis. *Ann Neurol* 1992; 32(6):758-766.
89. Bruck W, Bitsch A, Kolenda H, Bruck Y, Stiefel M, Lassmann H. Inflammatory central nervous system demyelination: correlation of magnetic resonance imaging findings with lesion pathology. *Ann Neurol* 1997; 42(5):783-793.
90. Bakshi R, Hutton GJ, Miller JR, Radue EW. The use of magnetic resonance imaging in the diagnosis and long-term management of multiple sclerosis. *Neurology* 2004; 63(11 Suppl 5):S3-11.
91. Hawkins CP, Mackenzie F, Tofts P, du Boulay EP, McDonald WI. Patterns of blood-brain barrier breakdown in inflammatory demyelination. *Brain* 1991; 114 ( Pt 2):801-810.
92. Hawkins CP, Munro PM, Mackenzie F, Kesselring J, Tofts PS, du Boulay EP, Landon DN, McDonald WI. Duration and selectivity of blood-brain barrier breakdown in chronic relapsing experimental allergic encephalomyelitis studied by gadolinium-DTPA and protein markers. *Brain* 1990; 113 ( Pt 2):365-378.
93. Cook LL, Foster PJ, Karlik SJ. Pathology-guided MR analysis of acute and chronic experimental allergic encephalomyelitis spinal cord lesions at 1.5T. *J Magn Reson Imaging* 2005; 22(2):180-188.
94. Miller DH, Rudge P, Johnson G, Kendall BE, Macmanus DG, Moseley IF, Barnes D, McDonald WI. Serial gadolinium enhanced magnetic resonance imaging in multiple sclerosis. *Brain* 1988; 111 ( Pt 4):927-939.
95. Kermodé AG, Tofts PS, Thompson AJ, Macmanus DG, Rudge P, Kendall BE, Kingsley DP, Moseley IF, du Boulay EP, McDonald WI. Heterogeneity of blood-brain barrier changes in multiple sclerosis: an MRI study with gadolinium-DTPA enhancement. *Neurology* 1990; 40(2):229-235.
96. Grossman RI, Gonzalez-Scarano F, Atlas SW, Galetta S, Silberberg DH. Multiple sclerosis: gadolinium enhancement in MR imaging. *Radiology* 1986; 161(3):721-725.
97. Kermodé AG, Thompson AJ, Tofts P, Macmanus DG, Kendall BE, Kingsley DP, Moseley IF, Rudge P, McDonald WI. Breakdown of the blood-brain barrier precedes symptoms and other MRI signs of new lesions in multiple sclerosis. Pathogenetic and clinical implications. *Brain* 1990; 113 ( Pt 5):1477-1489.

98. Kappos L, Moeri D, Radue EW, Schoetzau A, Schweikert K, Barkhof F, Miller D, Gutmman CR, Weiner HL, Gasperini C, Filippi M. Predictive value of gadolinium-enhanced magnetic resonance imaging for relapse rate and changes in disability or impairment in multiple sclerosis: a meta-analysis. *Gadolinium MRI Meta-analysis Group. Lancet* 1999; 353(9157):964-969.
99. Smith ME, Stone LA, Albert PS, Frank JA, Martin R, Armstrong M, Maloni H, McFarlin DE, McFarland HF. Clinical worsening in multiple sclerosis is associated with increased frequency and area of gadopentetate dimeglumine-enhancing magnetic resonance imaging lesions. *Ann Neurol* 1993; 33(5):480-489.
100. Khoury SJ, Gutmman CR, Orav EJ, Hohol MJ, Ahn SS, Hsu L, Kikinis R, Mackin GA, Jolesz FA, Weiner HL. Longitudinal MRI in multiple sclerosis: correlation between disability and lesion burden. *Neurology* 1994; 44(11):2120-2124.
101. Trojano M, Avolio C, Liuzzi GM, Ruggieri M, Defazio G, Liguori M, Santacroce MP, Paolicelli D, Giuliani F, Riccio P, Livrea P. Changes of serum sICAM-1 and MMP-9 induced by rIFNbeta-1b treatment in relapsing-remitting MS. *Neurology* 1999; 53(7):1402-1408.
102. Richert ND, Ostuni JL, Bash CN, Duyn JH, McFarland HF, Frank JA. Serial whole-brain magnetization transfer imaging in patients with relapsing-remitting multiple sclerosis at baseline and during treatment with interferon beta-1b. *AJNR Am J Neuroradiol* 1998; 19(9):1705-1713.
103. Rovaris M, Agosta F, Sormani MP, Inglese M, Martinelli V, Comi G, Filippi M. Conventional and magnetization transfer MRI predictors of clinical multiple sclerosis evolution: a medium-term follow-up study. *Brain* 2003; 126(Pt 10):2323-2332.
104. Dousset V, Grossman RI, Ramer KN, Schnall MD, Young LH, Gonzalez-Scarano F, Lavi E, Cohen JA. Experimental allergic encephalomyelitis and multiple sclerosis: lesion characterization with magnetization transfer imaging. *Radiology* 1992; 182(2):483-491.
105. Pike GB, de Stefano N, Narayanan S, Francis GS, Antel JP, Arnold DL. Combined magnetization transfer and proton spectroscopic imaging in the assessment of pathologic brain lesions in multiple sclerosis. *AJNR Am J Neuroradiol* 1999; 20(5):829-837.
106. Gareau PJ, Rutt BK, Karlik SJ, Mitchell JR. Magnetization transfer and multicomponent T2 relaxation measurements with histopathologic correlation in an experimental model of MS. *J Magn Reson Imaging* 2000; 11(6):586-595.

107. Chen JT, Collins DL, Atkins HL, Freedman MS, Arnold DL. Magnetization transfer ratio evolution with demyelination and remyelination in multiple sclerosis lesions. *Ann Neurol* 2008; 63(2):254-262.
108. van Waesberghe JH, van Walderveen MA, Castelijns JA, Scheltens P, Nijeholt GJ, Polman CH, Barkhof F. Patterns of lesion development in multiple sclerosis: longitudinal observations with T1-weighted spin-echo and magnetization transfer MR. *AJNR Am J Neuroradiol* 1998; 19(4):675-683.
109. Blezer EL, Bauer J, Brok HP, Nicolay K, 't Hart BA. Quantitative MRI-pathology correlations of brain white matter lesions developing in a non-human primate model of multiple sclerosis. *NMR Biomed* 2007; 20(2):90-103.
110. Schmierer K, Scaravilli F, Altmann DR, Barker GJ, Miller DH. Magnetization transfer ratio and myelin in postmortem multiple sclerosis brain. *Ann Neurol* 2004; 56(3):407-415.
111. Tsutsui S, Schnermann J, Noorbakhsh F, Henry S, Yong VW, Winston BW, Warren K, Power C. A1 adenosine receptor upregulation and activation attenuates neuroinflammation and demyelination in a model of multiple sclerosis. *J Neurosci* 2004; 24(6):1521-1529.
112. Giuliani F, Fu SA, Metz LM, Yong VW. Effective combination of minocycline and interferon-beta in a model of multiple sclerosis. *J Neuroimmunol* 2005; 165(1-2):83-91.
113. Bergman RK, Munoz JJ, Portis JL. Vascular permeability changes in the central nervous system of rats with hyperacute experimental allergic encephalomyelitis induced with the aid of a substance from *Bordetella pertussis*. *Infect Immun* 1978; 21(2):627-637.
114. Giuliani F, Metz LM, Wilson T, Fan Y, Bar-Or A, Yong VW. Additive effect of the combination of glatiramer acetate and minocycline in a model of MS. *J Neuroimmunol* 2005; 158(1-2):213-221.
115. Meyerand ME, Cremillieux Y, Wadghiri YZ, Azzawi A, Hoopes PJ, Dunn JF. In vivo gradient echo microimaging of rodent spinal cord at 7 T. *Magn Reson Med* 1998; 40(5):789-791.
116. Zhang Z, Davies K, Prostack J, Fenstermacher J, Chopp M. Quantitation of microvascular plasma perfusion and neuronal microtubule-associated protein in ischemic mouse brain by laser-scanning confocal microscopy. *J Cereb Blood Flow Metab* 1999; 19(1):68-78.
117. Hultstrom D, Svensjo E. Intravital and electron microscopic study of bradykinin-induced vascular permeability changes using FITC-dextran as a tracer. *J Pathol* 1979; 129(3):125-133.

118. Thorball N. FITC-dextran tracers in microcirculatory and permeability studies using combined fluorescence stereo microscopy, fluorescence light microscopy and electron microscopy. *Histochemistry* 1981; 71(2):209-233.
119. Hawkins CP, Munro PM, Landon DN, McDonald WI. Metabolically dependent blood-brain barrier breakdown in chronic relapsing experimental allergic encephalomyelitis. *Acta Neuropathol* 1992; 83(6):630-635.
120. Claudio L, Kress Y, Factor J, Brosnan CF. Mechanisms of edema formation in experimental autoimmune encephalomyelitis. The contribution of inflammatory cells. *Am J Pathol* 1990; 137(5):1033-1045.
121. Floris S, Blezer EL, Schreibelt G, Dopp E, van der Pol SM, Schadee-Eestermans IL, Nicolay K, Dijkstra CD, de Vries HE. Blood-brain barrier permeability and monocyte infiltration in experimental allergic encephalomyelitis: a quantitative MRI study. *Brain* 2004; 127(Pt 3):616-627.
122. Wong FS, Dittel BN, Janeway CA, Jr. Transgenes and knockout mutations in animal models of type 1 diabetes and multiple sclerosis. *Immunol Rev* 1999; 169:93-104.
123. Fazekas G, Tabira T. What transgenic and knockout mouse models teach us about experimental autoimmune encephalomyelitis. *Rev Immunogenet* 2000; 2(1):115-132.
124. Dousset V, Ballarino L, Delalande C, Coussemaq M, Canioni P, Petry KG, Caille JM. Comparison of ultrasmall particles of iron oxide (USPIO)-enhanced T2-weighted, conventional T2-weighted, and gadolinium-enhanced T1-weighted MR images in rats with experimental autoimmune encephalomyelitis. *AJNR Am J Neuroradiol* 1999; 20(2):223-227.
125. Wolburg H, Wolburg-Buchholz K, Engelhardt B. Diapedesis of mononuclear cells across cerebral venules during experimental autoimmune encephalomyelitis leaves tight junctions intact. *Acta Neuropathol* 2005; 109(2):181-190.
126. Engelhardt B, Wolburg H. Mini-review: Transendothelial migration of leukocytes: through the front door or around the side of the house? *Eur J Immunol* 2004; 34(11):2955-2963.
127. Gu L, Tseng SC, Rollins BJ. Monocyte chemoattractant protein-1. *Chem Immunol* 1999; 72:7-29.
128. Mahad DJ, Ransohoff RM. The role of MCP-1 (CCL2) and CCR2 in multiple sclerosis and experimental autoimmune encephalomyelitis (EAE). *Semin Immunol* 2003; 15(1):23-32.

129. McManus C, Berman JW, Brett FM, Staunton H, Farrell M, Brosnan CF. MCP-1, MCP-2 and MCP-3 expression in multiple sclerosis lesions: an immunohistochemical and in situ hybridization study. *J Neuroimmunol* 1998; 86(1):20-29.
130. Van d, V, Tekstra J, Beelen RH, Tensen CP, Van d, V, De Groot CJ. Expression of MCP-1 by reactive astrocytes in demyelinating multiple sclerosis lesions. *Am J Pathol* 1999; 154(1):45-51.
131. Simpson JE, Newcombe J, Cuzner ML, Woodroffe MN. Expression of monocyte chemoattractant protein-1 and other beta-chemokines by resident glia and inflammatory cells in multiple sclerosis lesions. *J Neuroimmunol* 1998; 84(2):238-249.
132. Sorensen TL, Ransohoff RM, Strieter RM, Sellebjerg F. Chemokine CCL2 and chemokine receptor CCR2 in early active multiple sclerosis. *Eur J Neurol* 2004; 11(7):445-449.
133. Mahad D, Callahan MK, Williams KA, Ubogu EE, Kivisakk P, Tucky B, Kidd G, Kingsbury GA, Chang A, Fox RJ, Mack M, Sniderman MB, Ravid R, Staugaitis SM, Stins MF, Ransohoff RM. Modulating CCR2 and CCL2 at the blood-brain barrier: relevance for multiple sclerosis pathogenesis. *Brain* 2006; 129(Pt 1):212-223.
134. Izikson L, Klein RS, Charo IF, Weiner HL, Luster AD. Resistance to experimental autoimmune encephalomyelitis in mice lacking the CC chemokine receptor (CCR)2. *J Exp Med* 2000; 192(7):1075-1080.
135. Huang DR, Wang J, Kivisakk P, Rollins BJ, Ransohoff RM. Absence of monocyte chemoattractant protein 1 in mice leads to decreased local macrophage recruitment and antigen-specific T helper cell type 1 immune response in experimental autoimmune encephalomyelitis. *J Exp Med* 2001; 193(6):713-726.
136. Hulkower K, Brosnan CF, Aquino DA, Cammer W, Kulshrestha S, Guida MP, Rapoport DA, Berman JW. Expression of CSF-1, c-fms, and MCP-1 in the central nervous system of rats with experimental allergic encephalomyelitis. *J Immunol* 1993; 150(6):2525-2533.
137. Ransohoff RM, Hamilton TA, Tani M, Stoler MH, Shick HE, Major JA, Estes ML, Thomas DM, Tuohy VK. Astrocyte expression of mRNA encoding cytokines IP-10 and JE/MCP-1 in experimental autoimmune encephalomyelitis. *FASEB J* 1993; 7(6):592-600.
138. Toft-Hansen H, Buist R, Sun XJ, Schellenberg A, Peeling J, Owens T. Metalloproteinases control brain inflammation induced by pertussis toxin in mice overexpressing the chemokine CCL2 in the central nervous system. *J Immunol* 2006; 177(10):7242-7249.

139. Fuentes ME, Durham SK, Swerdel MR, Lewin AC, Barton DS, Megill JR, Bravo R, Lira SA. Controlled recruitment of monocytes and macrophages to specific organs through transgenic expression of monocyte chemoattractant protein-1. *J Immunol* 1995; 155(12):5769-5776.
140. Huang D, Tani M, Wang J, Han Y, He TT, Weaver J, Charo IF, Tuohy VK, Rollins BJ, Ransohoff RM. Pertussis toxin-induced reversible encephalopathy dependent on monocyte chemoattractant protein-1 overexpression in mice. *J Neurosci* 2002; 22(24):10633-10642.
141. Lu C, Pelech S, Zhang H, Bond J, Spach K, Noubade R, Blankenhorn EP, Teuscher C. Pertussis toxin induces angiogenesis in brain microvascular endothelial cells. *J Neurosci Res* 2008; 86(12):2624-2640.
142. Stamatovic SM, Dimitrijevic OB, Keep RF, Andjelkovic AV. Protein kinase Calpha-RhoA cross-talk in CCL2-induced alterations in brain endothelial permeability. *J Biol Chem* 2006; 281(13):8379-8388.
143. Stamatovic SM, Shakui P, Keep RF, Moore BB, Kunkel SL, Van Rooijen N, Andjelkovic AV. Monocyte chemoattractant protein-1 regulation of blood-brain barrier permeability. *J Cereb Blood Flow Metab* 2005; 25(5):593-606.
144. Song L, Pachter JS. Monocyte chemoattractant protein-1 alters expression of tight junction-associated proteins in brain microvascular endothelial cells. *Microvasc Res* 2004; 67(1):78-89.
145. Bruckener KE, el Baya A, Galla HJ, Schmidt MA. Permeabilization in a cerebral endothelial barrier model by pertussis toxin involves the PKC effector pathway and is abolished by elevated levels of cAMP. *J Cell Sci* 2003; 116(Pt 9):1837-1846.
146. Yong T, Meininger GA, Linthicum DS. Enhancement of histamine-induced vascular leakage by pertussis toxin in SJL/J mice but not BALB/c mice. *J Neuroimmunol* 1993; 45(1-2):47-52.
147. Linthicum DS, Munoz JJ, Blaskett A. Acute experimental autoimmune encephalomyelitis in mice. I. Adjuvant action of Bordetella pertussis is due to vasoactive amine sensitization and increased vascular permeability of the central nervous system. *Cell Immunol* 1982; 73(2):299-310.
148. Olah ME, Stiles GL. Adenosine receptor subtypes: characterization and therapeutic regulation. *Annu Rev Pharmacol Toxicol* 1995; 35:581-606.
149. Stehle JH, Rivkees SA, Lee JJ, Weaver DR, Deeds JD, Reppert SM. Molecular cloning and expression of the cDNA for a novel A2-adenosine receptor subtype. *Mol Endocrinol* 1992; 6(3):384-393.

150. Cronstein BN. Adenosine, an endogenous anti-inflammatory agent. *J Appl Physiol* 1994; 76(1):5-13.
151. Johnston JB, Silva C, Gonzalez G, Holden J, Warren KG, Metz LM, Power C. Diminished adenosine A1 receptor expression on macrophages in brain and blood of patients with multiple sclerosis. *Ann Neurol* 2001; 49(5):650-658.
152. Mayne M, Shepel PN, Jiang Y, Geiger JD, Power C. Dysregulation of adenosine A1 receptor-mediated cytokine expression in peripheral blood mononuclear cells from multiple sclerosis patients. *Ann Neurol* 1999; 45(5):633-639.
153. Mayne M, Fotheringham J, Yan HJ, Power C, Del Bigio MR, Peeling J, Geiger JD. Adenosine A2A receptor activation reduces proinflammatory events and decreases cell death following intracerebral hemorrhage. *Ann Neurol* 2001; 49(6):727-735.
154. Hasko G, Szabo C, Nemeth ZH, Kvetan V, Pastores SM, Vizi ES. Adenosine receptor agonists differentially regulate IL-10, TNF-alpha, and nitric oxide production in RAW 264.7 macrophages and in endotoxemic mice. *J Immunol* 1996; 157(10):4634-4640.
155. Parmely MJ, Zhou WW, Edwards CK, III, Borcharding DR, Silverstein R, Morrison DC. Adenosine and a related carbocyclic nucleoside analogue selectively inhibit tumor necrosis factor-alpha production and protect mice against endotoxin challenge. *J Immunol* 1993; 151(1):389-396.
156. Bouma MG, Stad RK, van den Wildenberg FA, Buurman WA. Differential regulatory effects of adenosine on cytokine release by activated human monocytes. *J Immunol* 1994; 153(9):4159-4168.
157. Schwaninger M, Neher M, Viegas E, Schneider A, Spranger M. Stimulation of interleukin-6 secretion and gene transcription in primary astrocytes by adenosine. *J Neurochem* 1997; 69(3):1145-1150.
158. Le Moine O, Stordeur P, Schandene L, Marchant A, de Groote D, Goldman M, Deviere J. Adenosine enhances IL-10 secretion by human monocytes. *J Immunol* 1996; 156(11):4408-4414.
159. Sharief MK, Hentges R. Association between tumor necrosis factor-alpha and disease progression in patients with multiple sclerosis. *N Engl J Med* 1991; 325(7):467-472.
160. Sharief MK, Thompson EJ. In vivo relationship of tumor necrosis factor-alpha to blood-brain barrier damage in patients with active multiple sclerosis. *J Neuroimmunol* 1992; 38(1-2):27-33.

161. Sun D, Samuelson LC, Yang T, Huang Y, Paliege A, Saunders T, Briggs J, Schnermann J. Mediation of tubuloglomerular feedback by adenosine: evidence from mice lacking adenosine 1 receptors. *Proc Natl Acad Sci U S A* 2001; 98(17):9983-9988.
162. Ditamo Y, Degano AL, Maccio DR, Pistoiresi-Palencia MC, Roth GA. Age-related changes in the development of experimental autoimmune encephalomyelitis. *Immunol Cell Biol* 2005; 83(1):75-82.
163. Smith ME, Eller NL, McFarland HF, Racke MK, Raine CS. Age dependence of clinical and pathological manifestations of autoimmune demyelination. Implications for multiple sclerosis. *Am J Pathol* 1999; 155(4):1147-1161.
164. Mandala S, Hajdu R, Bergstrom J, Quackenbush E, Xie J, Milligan J, Thornton R, Shei GJ, Card D, Keohane C, Rosenbach M, Hale J, Lynch CL, Rupprecht K, Parsons W, Rosen H. Alteration of lymphocyte trafficking by sphingosine-1-phosphate receptor agonists. *Science* 2002; 296(5566):346-349.
165. Peng X, Hassoun PM, Sammani S, McVerry BJ, Burne MJ, Rabb H, Pearse D, Tudor RM, Garcia JG. Protective effects of sphingosine 1-phosphate in murine endotoxin-induced inflammatory lung injury. *Am J Respir Crit Care Med* 2004; 169(11):1245-1251.
166. Schaphorst KL, Chiang E, Jacobs KN, Zaiman A, Natarajan V, Wigley F, Garcia JG. Role of sphingosine-1 phosphate in the enhancement of endothelial barrier integrity by platelet-released products. *Am J Physiol Lung Cell Mol Physiol* 2003; 285(1):L258-L267.
167. Garcia JG, Liu F, Verin AD, Birukova A, Dechert MA, Gerthoffer WT, Bamberg JR, English D. Sphingosine 1-phosphate promotes endothelial cell barrier integrity by Edg-dependent cytoskeletal rearrangement. *J Clin Invest* 2001; 108(5):689-701.
168. Schwab SR, Pereira JP, Matloubian M, Xu Y, Huang Y, Cyster JG. Lymphocyte sequestration through S1P lyase inhibition and disruption of S1P gradients. *Science* 2005; 309(5741):1735-1739.
169. Fujita T, Inoue K, Yamamoto S, Ikumoto T, Sasaki S, Toyama R, Chiba K, Hoshino Y, Okumoto T. Fungal metabolites. Part 11. A potent immunosuppressive activity found in *Isaria sinclairii* metabolite. *J Antibiot (Tokyo)* 1994; 47(2):208-215.
170. Brinkmann V, Davis MD, Heise CE, Albert R, Cottens S, Hof R, Bruns C, Prieschl E, Baumruker T, Hiestand P, Foster CA, Zollinger M, Lynch KR. The immune modulator FTY720 targets sphingosine 1-phosphate receptors. *J Biol Chem* 2002; 277(24):21453-21457.

171. Chiba K, Yanagawa Y, Masubuchi Y, Kataoka H, Kawaguchi T, Ohtsuki M, Hoshino Y. FTY720, a novel immunosuppressant, induces sequestration of circulating mature lymphocytes by acceleration of lymphocyte homing in rats. I. FTY720 selectively decreases the number of circulating mature lymphocytes by acceleration of lymphocyte homing. *J Immunol* 1998; 160(10):5037-5044.
172. Pinschewer DD, Ochsenbein AF, Odermatt B, Brinkmann V, Hengartner H, Zinkernagel RM. FTY720 immunosuppression impairs effector T cell peripheral homing without affecting induction, expansion, and memory. *J Immunol* 2000; 164(11):5761-5770.
173. Kappos L, Antel J, Comi G, Montalban X, O'Connor P, Polman CH, Haas T, Korn AA, Karlsson G, Radue EW. Oral fingolimod (FTY720) for relapsing multiple sclerosis. *N Engl J Med* 2006; 355(11):1124-1140.
174. Webb M, Tham CS, Lin FF, Lariosa-Willingham K, Yu N, Hale J, Mandala S, Chun J, Rao TS. Sphingosine 1-phosphate receptor agonists attenuate relapsing-remitting experimental autoimmune encephalitis in SJL mice. *J Neuroimmunol* 2004; 153(1-2):108-121.
175. Kataoka H, Sugahara K, Shimano K, Teshima K, Koyama M, Fukunari A, Chiba K. FTY720, sphingosine 1-phosphate receptor modulator, ameliorates experimental autoimmune encephalomyelitis by inhibition of T cell infiltration. *Cell Mol Immunol* 2005; 2(6):439-448.
176. Rausch M, Hiestand P, Foster CA, Baumann DR, Cannet C, Rudin M. Predictability of FTY720 efficacy in experimental autoimmune encephalomyelitis by in vivo macrophage tracking: clinical implications for ultrasmall superparamagnetic iron oxide-enhanced magnetic resonance imaging. *J Magn Reson Imaging* 2004; 20(1):16-24.
177. Fujino M, Funeshima N, Kitazawa Y, Kimura H, Amemiya H, Suzuki S, Li XK. Amelioration of experimental autoimmune encephalomyelitis in Lewis rats by FTY720 treatment. *J Pharmacol Exp Ther* 2003; 305(1):70-77.
178. Deloire-Grassin MS, Brochet B, Quesson B, Delalande C, Dousset V, Canioni P, Petry KG. In vivo evaluation of remyelination in rat brain by magnetization transfer imaging. *J Neurol Sci* 2000; 178(1):10-16.
179. Zaaaraoui W, Deloire M, Merle M, Girard C, Raffard G, Biran M, Inglese M, Petry KG, Gonen O, Brochet B, Franconi JM, Dousset V. Monitoring demyelination and remyelination by magnetization transfer imaging in the mouse brain at 9.4 T. *MAGMA* 2008; 21(5):357-362.
180. Lichtinghagen R, Seifert T, Kracke A, Marckmann S, Wurster U, Heidenreich F. Expression of matrix metalloproteinase-9 and its inhibitors in mononuclear blood cells of patients with multiple sclerosis. *J Neuroimmunol* 1999; 99(1):19-26.